

Manganese Oxides as Electrocatalysts in Water Oxidation: Synthesis, Characterization and their Activity in the Oxygen Evolution Reaction

DISSERTATION

vorgelegt von

Justus Heese-Gärtlein, M.Sc.

aus Berlin

von der Fakultät für Chemie
der Universität Duisburg-Essen
zur Erlangung des akademischen Grades

Doktor der Naturwissenschaften

- Dr. rer. nat. -

Promotionsausschuss:

Vorsitzender: Prof. Dr. Jochen Gutmann

Gutachter: Prof. Dr. Malte Behrens

Gutachter: Prof. Dr. Philipp Kurz

Tag der wissenschaftlichen Aussprache: 28.09.2018

Essen 2018

Eidesstattliche Erklärung

Hiermit versichere ich, die vorliegende Abschlussarbeit selbstständig und nur unter Verwendung der von mir angegebenen Quellen und Hilfsmittel verfasst zu haben. Sowohl inhaltlich als auch wörtlich entnommene Inhalte wurden als solche kenntlich gemacht. Die Arbeit hat in dieser oder vergleichbarer Form noch keinem anderem Prüfungsgremium vorgelegen.

Datum: _____ Unterschrift: _____

Abstract

The development of an efficient non-precious metal based electrocatalyst for the oxygen evolution reaction (OER) can be seen as a milestone to a sustainable energy scenario. Manganese oxides, which are deemed to be promising OER electrocatalysts, are in the main focus of this thesis with a particular emphasis on material and catalytic properties. Several different manganese oxide compounds were synthesized, characterized and compared regarding their electrocatalytic activity in the OER. For determination of material features, standard characterization methods such as thermogravimetric analysis, X-ray diffraction, N₂ physisorption experiments, scanning electron microscopy and atomic absorption spectroscopy were performed. Furthermore selected samples were investigated by complementary methods like Rietveld refinement of structural data or in situ Raman spectroscopy. By comparison of the electrocatalytic data clear differences in catalytic activity and stability depending on the manganese oxide species can be observed. Thus, the most active catalysts can be found within the hollandite-type oxides, like Cryptomelane which reaches a current density of about 30 mA cm⁻² at a potential of 1.8 V. A more in-depth examination of Cryptomelane was carried out for a determination of influencing factors independent of the structure type. Therefore, Cryptomelane samples were synthesized by varying methods. Based on this approach different material properties could be derived and partly linked with the catalytic activity. Thereby, the sample conductivity and the morphology were identified as important impact factors. However, the influence of other possibly important properties like the BET surface area were found to have only minor effects. Additionally, the electrocatalytic behavior is compared with water oxidation catalysis (WOC) using Ce⁴⁺ as chemical oxidising agent and H₂O₂ decomposition experiments. A detailed study on α -MnO₂ provides deeper knowledge about the influence of the tunnel cation as well as the electrocatalytic performance of a “pure” manganese oxide. Finally, the evaluation of manganese oxides as OER electrocatalysts is complemented by an investigation of the stability and material changes during catalysis.

Zusammenfassung

Die Entwicklung von leistungsfähigen nichtedelmetall-basierten Elektrokatalysatoren für die Sauerstoffentwicklungsreaktion (OER) stellt ein Meilenstein für den Weg zu flächendeckenden nachhaltigen Energiesystemen dar. Als vielversprechende OER Elektrokatalysatoren gelten Manganoxide, mit deren Katalyse- und Materialeigenschaften sich in der vorliegenden Dissertation befasst wird. Verschiedenste Manganoxidphasen wurden synthetisiert, charakterisiert und bezüglich ihrer katalytischen OER Aktivität verglichen. Zur Bestimmung der Materialmerkmale wurden Standardcharakterisierungsmethoden, z.B. Thermogravimetrie, Röntgenbeugung, Stickstoff-Physisorption-Verfahren, Atomabsorptionsspektroskopie und Rasterelektronenmikroskopie, angewandt. Bei ausgewählten Proben kamen zusätzlich ergänzende Methoden, wie die Rietveldverfeinerung der Strukturdaten oder die in situ Raman-Spektroskopie, zum Einsatz. Im Vergleich zeigten die jeweiligen Manganoxide gravierende Unterschiede bezüglich ihrer elektrokatalytischen Aktivität und Stabilität. So konnten die leistungsfähigsten Katalysatoren in der Gruppe der Hollandit-artigen Oxide verortet werden. Herausragend war hierbei Kryptomelan, welches eine Stromdichte von über 30 mA cm^{-2} bei einem Potential von 1.8 V aufweist. Für die Identifizierung von strukturtypunabhängigen Faktoren, die das elektrokatalytische Verhalten beeinflussen, erfolgte eine tiefgehende Untersuchung von Kryptomelan. Dafür wurden Kryptomelanproben über unterschiedliche Routen synthetisiert und somit verschiedene Materialeigenschaften eingestellt. Diese Eigenschaften konnten teilweise mit der katalytischen Aktivität korreliert werden. So konnte unter anderem der elektrischen Leitfähigkeit und der Morphologie entscheidender Einfluss zugeschrieben werden. Im Gegenzug wurden andere Materialeigenschaften, wie zum Beispiel die BET Oberfläche, als nahezu bedeutungslos eingestuft. Zusätzlich werden in der vorliegenden Arbeit auch Experimente zur chemischen Wasserspaltung mit Ce^{4+} als Oxidationsmittel sowie zur Wasserstoffperoxidzersetzung betrachtet und die Resultate einander gegenübergestellt. Eine detaillierte Studie über $\alpha\text{-MnO}_2$ gibt Aufschluss über den Einfluss des Tunnelkations und über die elektrokatalytischen Eigenschaften eines "reinen" Manganoxids. Die Bewertung der Eignung von Manganoxiden als OER Katalysatoren wurde durch Untersuchungen zur Stabilität und zu Materialveränderungen während der Katalyse ergänzt.

Acknowledgement

First, I would like to express my sincere gratitude to my thesis advisor Prof. Dr. Malte Behrens for the continuous support of my work, the motivation and the freedom in executing my research he granted to me.

Special thanks also to Prof. Dr. Philipp Kurz of the University of Freiburg for being the second reviewer of my doctoral work and Prof. Dr. Jochen Gutmann of the University of Duisburg-Essen for acting as chairman of the doctoral committee.

My acknowledgment for the financial support goes to the State of North Rhine-Westphalia through the University of Duisburg-Essen and the BMBF funded project MANGAN (FKZ: 03SF0511B). Many thanks to the working groups within the MANGAN project for the fruitful collaboration.

I sincerely thank all Behrens group members, Alex, Andreas, Anna, Chakrapani, Denise, Dominik, Fatih, Klaus, Maik, Manuel, Sabine and Stefanie for supporting my work and for enriching my time as doctoral student.

Additional special thanks to Klaus Friedel Ortega for all the inspiring discussions and his immense scientific knowledge, Fatih Özcan for providing the presented SEM images and conducting the TG measurements and Manuel Heimann and Stefanie Hoffmann for running the chemical water oxidation, the H_2O_2 decomposition and the N_2 physisorption experiments.

Furthermore thanks to Dulce M. Morales (Ruhr-University Bochum) for carrying out and interpreting the in operando Raman experiments, Laura Kühnel (Institute of Technology for Nanostructures, University Duisburg-Essen) for conducting the resistivity measurements and Niklas Cibura (MPI CEC) for running the TPO experiment of the $\alpha\text{-MnO}_2$ sample.

Moreover, I would like to thank all the other not yet mentioned people who have contributed to the successful realization of my scientific work.

Preface

This thesis contains the main research results from my work as doctoral student, originated in the period from October 2015 to May 2018 under the supervision of Prof. Dr. Malte Behrens at the Faculty of Chemistry, University of Duisburg-Essen. My studies were conducted in the framework of the MANGAN project which pursues the overall question, if and under which conditions manganese oxide based materials are able to replace existing water splitting catalysts. My work was divided in three main parts. First of all, a rough screening of the catalytic OER activity and a characterization of several manganese oxides differing in structure and/or in composition were carried out. Based on the results the respective phase depending suitability as electrocatalyst is evaluated in Chapter 3. The most active catalyst, Cryptomelane, was chosen for further research aiming at finding structure-property relationships as described in Chapter 4. Finally, the thesis discuss an in-depth investigation of the structural related α -MnO₂ in Chapter 5. The three before mentioned chapters were written in the manuscript-style for a scientific publication. Thus, each of these chapters can be seen as independent and consequently some information may be repeated. For the sake of clarity, the entire work was kept in a consistent layout and all references were combined in one list.

Table of Contents

Eidesstattliche Erklärung	I
Abstract	II
Zusammenfassung	III
Acknowledgement	IV
Preface	VI

I – Introduction

1. Motivation	2
2. Theoretical Background on Selected Topics	4
2.1 X-ray Powder Diffraction	4
2.2 Electrocatalytic Water Oxidation	8

II – Results and Discussion

3. Synthesis, Characterization and OER Activity of different Manganese Oxides	13
3.1 Abstract	14
3.2 Introduction.....	14
3.3 Experimental Section	17
3.3.1 Synthesis	17
3.3.2 Characterization.....	18
3.3.3 Electrocatalysis	20
3.4 Results and Discussion.....	21
3.4.1 Characterization.....	21
3.4.2 Electrocatalysis.....	29
3.5 Conclusion.....	31
3.6 Acknowledgement.....	31
3.7 Supporting information	32
4. Cryptomelane as Water Oxidation Catalyst: Factors Influencing the OER Activity	37
4.1 Abstract	38
4.2 Introduction.....	38

4.3 Experimental Section	40
4.3.1 Synthesis and sample labelling	40
4.3.2 Characterization	41
4.3.3 Catalysis	43
4.4 Results and Discussion	44
4.4.1 Characterization	44
4.4.2 Catalysis	51
4.5 Conclusion	60
4.6 Acknowledgement	61
4.7 Supporting information	62
5. Controlling the Crystallinity of α-MnO₂ Synthesized by Acid Digestion of Bixbyite and its Electro-catalytic OER Activity	63
5.1 Abstract	64
5.2 Introduction	64
5.3 Experimental Section	67
5.3.1 Synthesis	67
5.3.2 Characterization	67
5.3.3 Electrocatalysis	69
5.4 Results and Discussion	70
5.4.1 Synthesis and Characterisation	70
5.4.2 Electrocatalysis	75
5.5 Conclusion	80
5.6 Acknowledgement	80
5.7 Supporting information	81
6. Conclusion and Outlook	83
7. References	84
A. Appendix	89
A.1 List of Publications	89
A.2 List of Conference Contributions	92
List of Figures	93
List of Tables	97

I – Introduction

1. Motivation

One of the biggest challenges humankind faces today, is satisfying the constantly increasing energy demands at dwindling resources. Additionally, the conventional energy production has fallen into disrepute over wide parts of the globe. The main reasons can be found in the uncertainty and the consequent risk of the used technology as well as of the increasing global environmental pollution. Especially the huge emission of greenhouse gases which are largely responsible for an accelerated climate warming is seen as highly problematic. Against this backdrop, a comprehensive power supply based on sustainable energy generation is mandatorily required. From the scientific and technological point of view, this goal is currently not hindered by the energy production. The usage of solar energy and wind power is well established. The bottleneck rather lies in suitable systems for the storage of energy which are crucial for supplying devices decoupled from the power grid like automobiles and for compensating shortages in energy production. The most promising approach is based on the chemical energy storage producing fuels from renewable energy. Independent of the specific kind of fuel, the first step of the production chain will likely be the generation of reducing equivalents in form of hydrogen. For this, water can act as practicable almost unlimited source. The electrolysis of water to produce hydrogen can be seen as fundament of the chemical energy storage. Water splitting consists of two half reactions: the hydrogen evolution reaction (HER) and the oxygen evolution reaction (OER). Although the general interest aims at the production of hydrogen, the oxygen evolution reaction is for stoichiometric reasons unavoidable. Moreover, the OER represents the determining step in the overall reaction and thus has shifted into focus of research. The decomposition of water into oxygen and hydrogen has a standard potential of -1.23 V . Induced by unfavorable kinetics, the four-electron oxidation of water to oxygen at the anode needs a higher overvoltage to run. Electrocatalysts are able to lower this overpotential. Developing suitable catalysts and finding material related properties that influence the electrocatalytic performance are goals of the current research. The best known catalysts are based on the precious metals iridium and ruthenium.^{[1][2]} Unfortunately, both metals are expensive, rare and the respective OER catalyst (usually an oxide) degrades during reaction. Thus, they are economically unsuitable for a global application. For a large-scale deployment, the catalyst material should be based on elements which are able to accomplish important properties like inexpensiveness, natural abundance, simple handling and low toxicity. Considering these points, manganese oxides can be seen as promising candidates. Prior to the

development of a usable water electrolysis device equipped with a manganese oxide catalyst, the profound investigation of material related properties is required and the aim of this PhD thesis. Therefor a foundation of broad knowledge was built by the synthesis, characterization and OER activity screening of several MnO_x phases. Based on this, hollandite-type manganese oxides, as most promising catalysts, were selected for a more detailed study on electrocatalytic behavior and structure-property relations.

2. Theoretical Background on Selected Topics

In the scope of this thesis, several analytic and synthetic methods were applied. Relevant background information are given in the respective chapters. The analyses and interpretation of structural features by using X-ray Powder Diffraction (PXRD) and the electrocatalytic measurements are two key elements in all three manuscripts and are thus more in-depth discussed in the following.

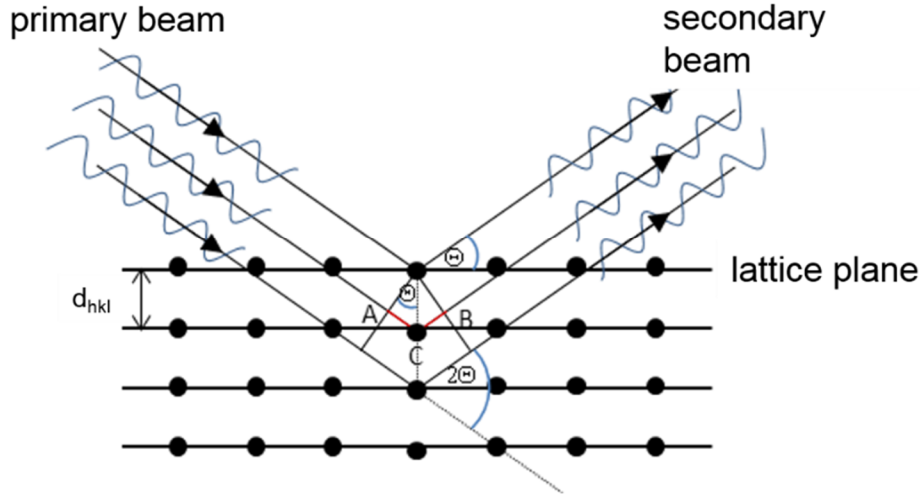
2.1 X-ray Powder Diffraction

In 1992, the International Union of Crystallography defined a crystal as “any solid having an essentially discrete diffraction diagram”.^[3] X-ray diffractometry is an often-used method to study the structure and composition of crystalline materials. The atomic distances in a crystalline solid are of a similar order of magnitude as the wavelengths of X-rays ($\lambda \approx 10 \text{ nm-1 pm}$), so a crystal can be seen as a three-dimensional diffraction grating. X-ray waves are elastically scattered by the electrons of an atom. The scattered waves interfere with each other depending on the arrangement and distance of the atoms. If the waves, scattered from parallel lattice planes, interfere constructively, they remain in phase resulting in a secondary beam which is macroscopically perceived as the diffracted X-ray. According to the Bragg condition, a constructive interference occurs if the path difference ($2d_{hkl}\sin\theta$) of the scattered waves is equal to an integer multiple of the wavelength. This condition is described by Bragg's law (equation (2.1)).

$$n\lambda = 2d_{hkl}\sin\theta \quad (2.1)$$

d_{hkl}	interplanar distance	θ	scattering angle
n	positive integer, diffraction order	λ	wavelength of the incident wave

By assuming the before mentioned requirement ($\Delta S(\text{path difference}) = n\lambda$) Bragg's law can be derived by a simple geometric consideration (Figure 2.1).



Derivation of Bragg's law:

$$\Delta S(\text{path difference}) = n\lambda \quad (2.2)$$

$$\overline{AC} = \overline{CB} = d_{hkl}\sin\theta \quad (2.3)$$

$$\Delta S = \overline{AC} + \overline{CB} = 2d_{hkl}\sin\theta \quad (2.4)$$

$$2d_{hkl}\sin\theta = n\lambda \quad (2.5)$$

Figure 2.1. Scheme of the diffraction geometry of the Bragg condition.

With a suitable apparatus, the intensity of the diffracted X-rays can be measured as a function of the diffraction angle. From the data of such a diffraction diagram, properties of the spatial structure of a crystalline sample can be derived. Characteristic in a powder diffraction diagram are the reflection position, the reflection intensity and the reflection shape. While the position reveals information about the lattice metric, the peak width mainly depends on crystal defects. The observed scattering intensity provides indications about the position and arrangement of the atoms in the unit cell. One common method to characterize crystalline materials is the Rietveld refinement of such X-ray powder data.^[4] The technique uses a least squares approach to refine various metric and instrumental parameters of a theoretical diffraction pattern to approximate it to the measured one. Based on this technique important structural information can be obtained, for example about the lattice parameters, domain size, texture properties or atomic positions. Further insight can be found in regarding the phase purity or the phase ratio of multi-phase samples. From the mathematical point of view, the Rietveld refinement aims to minimize a function S_y which describes the difference between a calculated profile y_{ci} and the observed data y_i .^{[5][6]}

$$S_y = \sum_i \frac{1}{y_i} (y_i - y_{ci})^2 \quad (2.6)$$

During the refinement the intensity at each point in the diffraction pattern is calculated.

$$y_{ci} = s \sum_{hkl} L_{hkl} |F_{hkl}|^2 \Phi(2\theta_i - 2\theta_{hkl}) P_{hkl} A + y_{bi} \quad (2.7)$$

s	scale factor	hkl	Miller indices
Φ	reflection profile function	A	absorption factor
F_{hkl}	structure factor	y_{bi}	background intensity
P_{hkl}	preferred orientation function	L_{hkl}	contains Lorentz, polarization and multiplicity factors

Like obvious in equation (2.7) the intensity correlates with the squared modulus of the structure factor F_{hkl} :

$$y_{ci} \propto |F_{hkl}|^2 \quad (2.8)$$

The structure factor can be determined by the following expression:

$$F_{hkl} = \sum_{j=1}^n f_j \exp[2\pi i(hx_j + ky_j + lz_j)] \exp[-M_j] \quad (2.9)$$

$$M_j = 8\pi^2 \overline{u_s^2} \sin^2 \frac{\theta}{\lambda^2} = B_j \sin^2 \frac{\theta}{\lambda^2} \quad (2.10)$$

h, k, l	Miller indices	n	number of atoms in the unit cell
x_j, y_j, z_j	coordinates of the jth atom	f_j	atomic form factor of the jth atom
$\overline{u_s^2}$	mean squared displacement	B	B-factor

The atomic form factor f_j depends on the number of electrons of an atom and expresses its scattering ability. Due to negative interference within the electron shell, the atomic form factor (and thus the intensity) decreases with increasing diffraction angle. The B-factor (see also Debye–Waller factor) describes the thermal and random static displacement of the jth atom.^[5] The quality of the structure refinement can be evaluated by judging the graphical result and by using numerical criteria of fit. Nowadays, well-established criteria are the R-values (residual).

Several different R 's were developed in the last decades. Often considered are the R-structure factor R_F and the R-Bragg factor R_B which are based on the integrated intensities.^[7]

$$R_F = \frac{\sum |I_{hkl/o}^{0.5} - I_{hkl/c}^{0.5}|}{\sum I_{hkl/o}^{0.5}} \quad (2.11)$$

$$R_B = \frac{\sum |I_{hkl/o} - I_{hkl/c}|}{\sum I_{hkl/o}} \quad (2.12)$$

$I_{hkl/o}$ observed integrated intensity $I_{hkl/c}$ calculated integrated intensity

In contrast to the R-pattern R_p and R-weighted pattern R_{wp} values which use the observed and calculated intensities at the i th step. The weighting factor w_i is often defined as $\frac{1}{y_i}$ but other values are possible.^[7]

$$R_p = \frac{\sum |y_i - y_{ci}|}{\sum y_i} \quad (2.13)$$

$$R_{wp} = \left[\frac{\sum w_i (y_i - y_{ci})^2}{\sum w_i (y_i)^2} \right]^{0.5} \quad (2.14)$$

Young emphasizes the R-weighted pattern R_{wp} as mathematically most meaningful R value because the before mentioned value S_y which has to be minimized is considered in the numerator. R_{wp} is linked to the “goodness of fit” S via R_{exp} which is defined as follows:

$$R_{exp} = \left[\frac{N - P}{\sum w_i (y_i)^2} \right]^{0.5} \quad (2.15)$$

N number of measuring points P number of refined parameters

$$S = \frac{R_{wp}}{R_{exp}} \quad (2.16)$$

How low the “goodness of fit” should be for a successful refinement, is still discussed in literature and depends on the author. D. A. Weber recommends a value smaller than 2 as goal of the refinement whereas R. A. Young judges stricter and advises to aim at $S < 1.3$.^{[8][5]}

2.2 Electrocatalytic Water Oxidation

Several approaches to split water in hydrogen and oxygen are already known and partly well investigated.^{[9][10][11][12][13]} The manifold techniques are based on different physical effects. Noteworthy are the photocatalytic, chemical and thermal water splitting as well as the electrolysis of water which will be described more detailed in the following.

Electrolysis is a process to force a chemical reaction by using a direct electric current. Between a pair of electrodes, dipped in an electrolyte, an electric potential is applied. Ions which are part of the electrolyte are attracted by the respective opposing charged electrode. Neutral atoms move through diffusion. By applying a sufficient potential the chemical transformation of the educts occurs by the removal (anode) and the addition (cathode) of electrons at the electrolyte/electrode interface. The ob-

tained products often differ in the state of aggregation from the electrolyte and can be separated easily. During the electrolysis of water, two gaseous phases evolve which bubble from the electrolyte. The oxygen evolution reaction (OER) take place at the anode and the hydrogen evolution reaction (HER) at the cathode. The overall reaction of the water splitting is as follows:



The reaction consists of two half-cell reactions which depend on the pH value of the electrolyte.

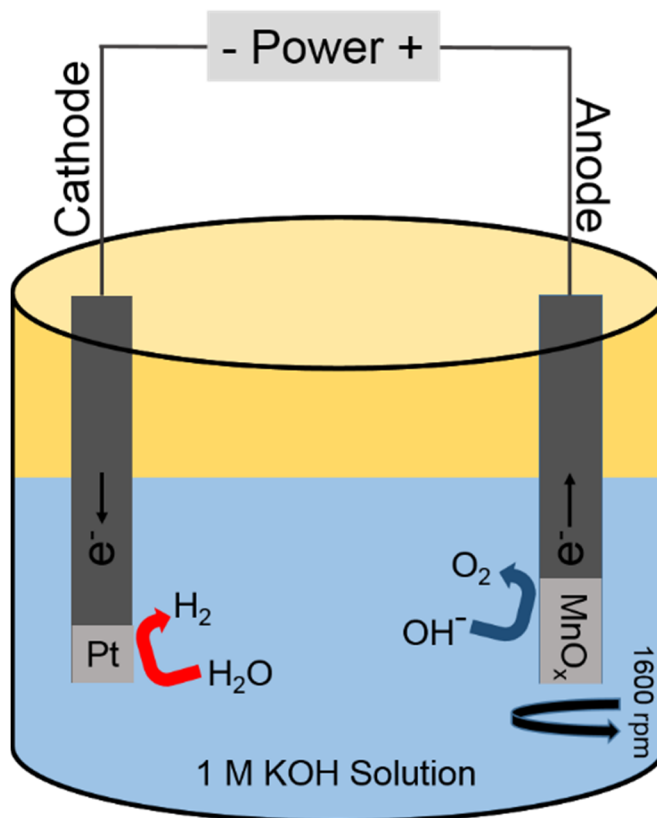
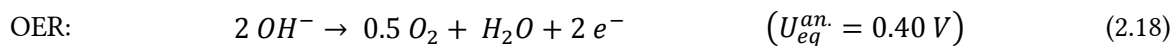
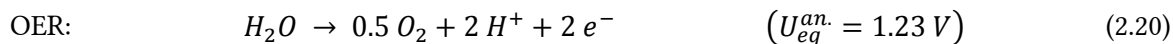


Figure 2.2. Abstract schema of water electrolysis and electrolyzer cell.

Alkaline solution:



Acidic solution:



To electrolyze water, a total energy of at least $237.1 \text{ kJ}\cdot\text{mol}^{-1}$ ($-\Delta G_{\text{H}_2\text{O}}^\circ$) has to be provided. Considering that the reaction involves two electrons ($z=2$), the water splitting equilibrium potential can be calculated at a value of about 1.23 V.

$$U_{eq} = \frac{-\Delta G_{\text{H}_2\text{O}}^\circ}{z \cdot F} = \frac{237.1 \frac{\text{kJ}}{\text{mol}}}{2 \cdot 96.485 \frac{\text{kJ}}{\text{V}\cdot\text{mol}}} = 1.229 \text{ V} \quad (2.22)$$

Although the standard potentials ($U_{eq}^{an.}$, $U_{eq}^{cat.}$) of the respective oxidation and reduction steps are pH dependent according to the Nernst equation, the potential difference which has to be applied between the electrodes keeps always 1.23 V (Figure 2.3). However in reality a substantial amount of potential has to be added to generate hydrogen and oxygen. This is caused by cell resistance and overpotential phenomena.^{[14][15]} The cell resistance is mainly affected by the design of the electrolyzer unit (e.g. electrode distance and size, conductivity of electrolyte, temperature, stirring speed) and can be optimized by a favorable setup. The electrode related overpotential comes due to kinetic limitations which depend on many different factors like the electrode material, the kind of evolving gas, the current density, the pH value or educt/product concentrations. Although these kinetic phenomena occur at both electrodes, the overpotential at the cathode can be nearly complete prevented by using an appropriate material like platinum. The major part of the overpotential comes from the anodic OER which consequently represents the bottleneck of the complete water splitting reaction.

$$U = U_{eq} + \eta_{cathode} + \eta_{anode} + \eta_r \quad (2.23)$$

U	Potential which has to be provided
U_{eq}	Standard electrode potential (1.23 V for H ₂ O)
$\eta_{cathode/anode}$	Overpotential to overcome the kinetic barriers at cathode/anode
η_r	Potential to compensate resistance losses

The required overpotential can be lowered by using suitable catalysts whose development is subject of current scientific research. A non-experimental approach is the identification of the mechanistic process of the OER. Knowledge about the determining step could help to optimize the catalytic material as well as the applied conditions. Several possible mechanistic pathways

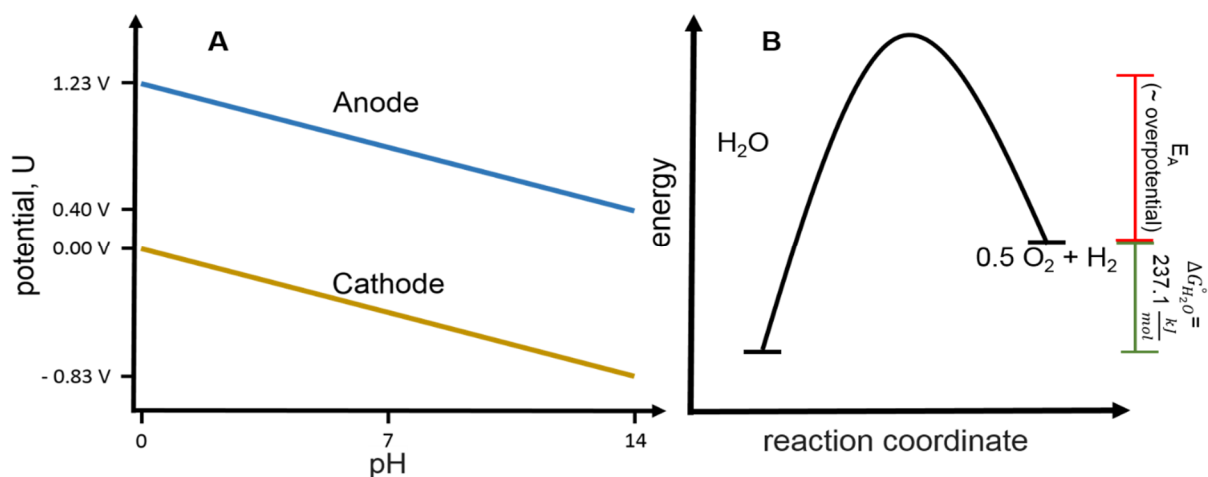
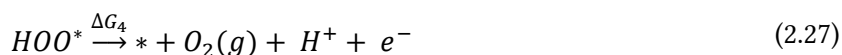
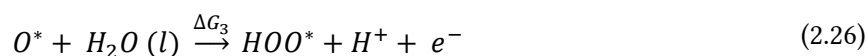
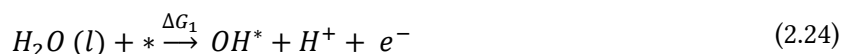


Figure 2.3. A: pH dependency of the half-cell reaction standard potentials. B: Relation between activation energy (E_a) and Gibbs energy in terms of electrocatalytic water splitting.

were proposed within the last decades.^[15] The working groups of Jan Rossmeisl and Jens K. Nørskov investigated the thermodynamic of the following four electron reaction paths by the usage of DFT (Density Functional Theory) based calculations.^[16]



They identified step 2 or 3 as rate determining independent from the oxide and reasoned it by a suboptimal O^* binding energy. By introducing a descriptor ($\Delta G_2 = \Delta G_{O^*} - \Delta G_{HO^*}$) and correlating it with the negative values of the theoretical overpotential (η_{OER}) of various materials a volcano plot was obtained (Figure 2.4). The plot clearly displays the most promising catalysts and confirms experimental results like the well-known superiority of ruthenium based materials. However, the results also reveal the theoretical suitability of manganese oxides as OER electrocatalysts.

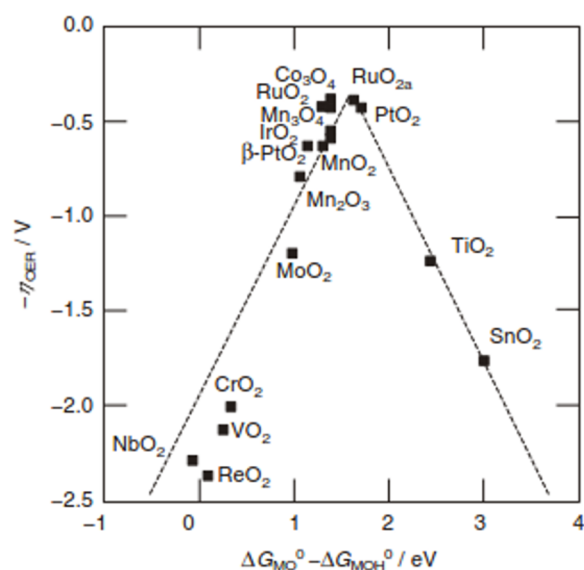


Figure 2.4. Theoretical overpotential of several oxides plotted against the standard free energy difference ΔG_2 .^{[15][16]}

II – Results and Discussion

3. Synthesis, Characterization and OER Activity of different Manganese Oxides

Justus Heese-Gärtlein^[a], Malte Behrens^{*[a]}

^[a] Faculty of Chemistry, Inorganic Chemistry
University of Duisburg-Essen and Center for Nanointegration Duisburg-Essen
Universitätsstr. 7, 45141 Essen, Germany

* Corresponding author (malte.behrens@uni-due.de)

Contributions of co-author:

M. Behrens: Advising, support and proofreading.

3.1 Abstract

Manganese oxides are seen as potential electrocatalysts for the oxygen evolution reaction (OER). At present a large number of manganese oxide compounds are known. To find the most suitable OER catalyst, some comparative studies of selected MnO_x materials were reported in recent years. However, caused by varying measuring parameters and conditions, the comparability of studies made by different working groups is often limited. For this study, a relatively large quantity of ten different manganese oxides differing in structure and/or composition were synthesized, characterized and compared regarding their OER activity and stability using a consistent set of experimental parameters. In general, manganese oxides of the hollandite-type with a formal oxidation state of +4 were more active than those with a lower oxidation state. It turned out that the activity strongly depends on the manganese oxide compound. As most active catalyst Cryptomelane reached a current density of about 15 mA cm^{-2} at a potential of 1.8 V. In contrast, the samples with the lowest activity exhibited values less than 1 mA cm^{-2} . The stability experiments revealed a fast decrease in activity of all samples within the first minutes of measurement and an activity loss of nearly 100 % after 60 min.

3.2 Introduction

A key technology to produce hydrogen in a clean way might be based on water electrolysis. To run the oxygen evolution reaction a potential difference of at least 1.23 V must be applied. The value of 1.23 V is in practice not realizable because different phenomena force a higher voltage. The critical step is the anodic oxygen evolution reaction (OER). The challenge of the catalytic research is to lower this overpotential by developing suitable electrocatalysts. These materials should be based on elements which are able to accomplish important properties like inexpensiveness, natural abundance, simple handling and low toxicity. Considering these points, manganese oxides can be seen as promising candidates.

Several manganese oxides with various properties are already known. [17][18][19][20][21][22][23][24][25][26][27][28] In the following the materials which are investigated in this work will be introduced shortly. Unit cells of the considered phases are depicted in Figure 3.1. Manganese(IV) oxides exist in various polymorphs which are all based on MnO_6 octahedra which differ in their linkage. MnO_2 is just the idealized composition since the average

oxidation state of manganese is commonly slightly below +4 caused by a mixed valence.^[10] ^{[17][29][30]} and many phases accommodate certain amounts of water and additional cations. The tetragonal Hollandite structure (α - MnO_2) consists of edge-sharing MnO_6 octahedra which form 2x2 tunnels with a spacing of the wall atoms of 4.8 Å.^[31] The tunnels commonly incorporate cations with an effective ionic radius of about 1.4 Å, like K^+ , NH_4^+ or Ba^{2+} .^[32] The most preferred one is potassium. The resulting K-Hollandite is called Cryptomelane. As one

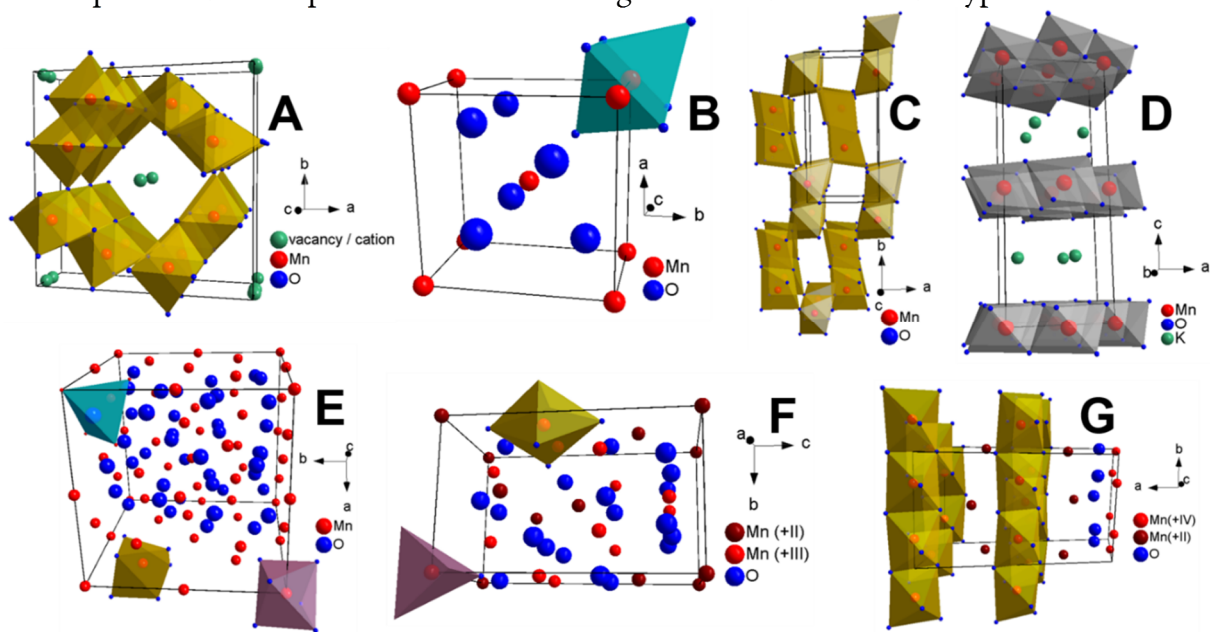


Figure 3.1. Idealized unit cells of hollandite-group (A), Pyrolusite (B), Ramsdellite (C), K-Birnessite (D), Bixbyite (E), Hausmannite (F) and Mn_5O_8 (G) with selected MnO_x polyhedra.

of the first J. W. Gruner described in 1943 the chemical composition, structural features and a synthetic route for Cryptomelane.^[33] In contrast to Cryptomelane, ammonium containing Hollandite (NH_4^+ -Hollandite) attracts less attention in research. In addition to the flexible type of the tunnel cations, also their amount in hollandite-type materials can strongly vary and decrease even to zero. The resulting pure phase is further called α - MnO_2 .^[34] At present, α - MnO_2 is the only known tunnelled manganese oxide which exhibits a stable structure even in the absence of a large stabilizing foreign cation in its tunnels. Hollandite-type manganese oxides are seen as attractive materials for several applications, like electrode component for rechargeable lithium batteries^[34], as catalyst for the degradation of chemicals^{[24][35][36][37][38][39][40][41]} and also as electrocatalyst for the alkaline oxygen evolution reaction (OER).^[42] In contrast to α - MnO_2 , the orthorhombic Ramsdellite (R- MnO_2) consists of 2x1 channels which are formed by double chains of edge-sharing MnO_6 octahedra connected by corners. Just like in α - MnO_2 the channels are orientated along the $\langle 001 \rangle$ direction.^{[26][43]} Ramsdellite was first fully described by Fleischer and Richmond in 1943 and named after the

mineralogist Lewis Steven Ramsdell, who identified Ramsdellite as mineral.^[44] A further tunnelled MnO_2 phase is Pyrolusite ($\beta\text{-MnO}_2$), an isotype to tetragonal rutile-type TiO_2 . The MnO_2 octahedra are edge-sharing along the $\langle 001 \rangle$ direction and crosslinked by corners building 1×1 channels.^{[45][46]} Reasoned by the ability to incorporate Li^+ into the channels Ramsdellite and Pyrolusite were studied as electrode material for lithium batteries.^{[47][48]} Beside the tunnelled phases, manganese oxides are also able to crystallize in a layer structure, for example Birnessite. Although it was already synthesized in previous years, Birnessite ($\delta\text{-MnO}_2$) obtained its name first in 1956 from Jones et al..^{[49][50][51]} Edge-sharing MnO_6 octahedra build layers with a interlayer distance of about 7 Å which are able to accommodate a wide variety and a large amount of ions and water molecules.^{[52][27]} Similar to the before mentioned tunnelled manganese oxides Birnessite shows potential as battery material^{[53][54]}, cation adsorbent^[55] or as catalyst in chemical and electrochemical water oxidation.^{[56][57][58]} Additional to the MnO_2 phases, oxides with a lower average oxidation state of manganese were investigated in this study. One representative of the manganese(III) oxides is $\alpha\text{-Mn}_2\text{O}_3$. The related mineral is called Bixbyite. The mineral $(\text{Fe},\text{Mn})_2\text{O}_3$ was first described by Penfield and Foote in 1897 and named after its discoverer Maynard Bixby.^[59] The structure of Bixbyite can be described as superstructure of the fluorite-type with ordered anionic vacancies and distorted MnO_6 octahedra.^{[60][61]} Among others, Bixbyite is known to be an active catalyst in CO oxidation and N_2O decomposition and can also be used as an adsorbent in waste water treatment.^{[62][63][64]} One of the oldest known manganese oxides is the mineral Hausmannite (Mn_3O_4) which was first described by Friedrich Hausmann in 1813.^[65] This manganese(II,III) oxide crystallizes in a tetragonal deformed spinel-type structure. The deformation comes from the Jahn-Teller distortion of the $\text{Mn}^{\text{III}}\text{O}_6$ octahedra.^{[66][67]} Hausmannite can act as oxidation catalyst and as sensing material.^{[68][69]} A synthetic manganese oxide without a known related naturally occurring mineral is Mn_5O_8 . This manganese(II,IV) oxide was first identified by W. Feitknecht in 1964 and structurally described by H. R. Oswald and M. J. Wampetich some years later.^{[28][70]} The monoclinic Mn_5O_8 consists of layered edge-linked distorted $\text{Mn}^{\text{IV}}\text{O}_6$ octahedra interrupted by Mn^{IV} vacancies. Between the octahedra, a Mn^{2+} cationic layer was proposed. The manganese(II) atoms are coordinated by oxygen atoms and build distorted $\text{Mn}^{\text{II}}\text{O}_6$ trigonal prisms.^[70] Mn_5O_8 is rarely noticed in literature but found attention as electrocatalyst for the OER at neutral pH.^[71]

In this study, the before mentioned MnO_x compounds were synthesized and characterized. Aiming at a high comparability, the catalytic performances were measured by using the same experimental set up and conditions.

3.3 Experimental Section

3.3.1 Synthesis

α -MnO₂

Adapted from Ohzuku et al.^[72] α -MnO₂ was synthesized by thermal treatment of Bixbyite (α -Mn₂O₃) powder with a sulfuric acid solution in a reflux apparatus. Therefore, 0.3 g α -Mn₂O₃ and 113 ml 4 molar H₂SO₄ solution (H₂SO₄: >95 %, Thermo Fisher Scientific GmbH, demineralized water: conductivity < 5 μ S) were stirred (500 rpm) in a 250 ml round-bottom flask for 24 h at a temperature of 80 °C (yield = 85 - 91 %). The Bixbyite powder was synthesized by calcination of Manganese(III) acetate (97 % p.a., Sigma-Aldrich) in a muffle furnace for 24 h at 800 °C (β = 32 K min⁻¹).

Calc.- α -MnO₂

Calc.- α -MnO₂ was obtained by the calcination of α -MnO₂ for 6 h at 475 °C (β = 19 K min⁻¹) in a muffle furnace. The used α -MnO₂ was obtained by the before described route.

Cryptomelane

To synthesize Cryptomelane analogous to the literature procedure^[73], 2 ml HCl (37 %, VWR Chemicals) was added to 160 ml of a 0.1 molar KMnO₄ (>99 % p.a., Carl Roth GmbH) solution. After stirring (500 rpm) for 30 min at room temperature the solution was hydrothermally treated for 8 h at 150 °C in a Teflon-lined autoclave (250 ml).

NH₄-Hollandite

Based on the same route like pure α -MnO₂, NH₄-Hollandite was synthesized via the procedure of Ohzuku et al.^[72] Therefore, Bixbyite (made by calcination of Mn(CH₃COO)₃) and (NH₄)₂SO₄ (>99 % p.a., Sigma-Aldrich Chemie GmbH) were added in the molar ratio 1:1 to the 4 molar sulfuric acid solution and treated for 24 h at 80 °C.

Pyrolusite

For the synthesis of Pyrolusite a method reported by Gao et al. was used.^[74] 7.5 mmol (NH₄)₂S₂O₈ (>98 % p.a., Alfa Aesar/Thermo Fisher Scientific GmbH) and 7.5 mmol MnSO₄•4H₂O (>98 % p.a., Sigma-Aldrich Chemie GmbH) were dissolved in 160 ml H₂O. The solution was hydrothermal treated for 12 h at 140 °C in a Teflon-lined autoclave (250 ml).

Ramsdellite

Ramsdellite was synthesized by the same route like Pyrolusite however a lower temperature of 85 °C was applied.^{[25][74]}

K-Birnessite

Based on the published route from Ching et al.^[75], 50 ml of a 0.38 molar KMnO₄ solution was mixed with 20 ml of a 1.4 molar Glucose (99 % p.a., Alfa Aesar/Thermo Fisher Scientific GmbH) solution. The precipitate was kept in solution for 4 h and afterwards isolated, washed and dried in air at 80 °C for 12 h. The obtained precursor was calcined at 425 °C for 2 h ($\beta = 17 \text{ K min}^{-1}$) in a muffle furnace.

Bixbyite

Bixbyite was synthesized by solvothermal treatment of 2 g Pyrolusite in a Teflon-lined autoclave (250 ml) in 160 ml Ethanol for 24 h at 130 °C.^[76]

Hausmannite

The calcination of Pyrolusite in a muffle furnace for 4 h at 1000 °C ($\beta = 32 \text{ K min}^{-1}$) led to Hausmannite.

Mn₅O₈

A brown precursor was obtained by mixing 100 ml of a 0.4 molar Mn(NO₃)₂ (>98 % p.a., Carl Roth GmbH) solution with 100 ml of a 1 molar NaOH (>98.5 % p.a., VWR Chemicals) solution. The precipitate was washed, dried in air at 80 °C for 24 h and finally calcined at 400 °C for 3 h ($\beta = 16 \text{ K min}^{-1}$) in a muffle furnace.^[77]

All obtained powders were isolated and washed with demineralized water until the conductivity of the filtrates fell below 20 $\mu\text{S cm}^{-1}$. Finally, the samples were dried in static air at 80 °C for 24 h.

3.3.2 Characterization

Structural characterization

Powder XRD patterns in the 2θ range from 5 to 90° were recorded with a Bruker D8 Advance diffractometer in Bragg–Brentano geometry by using a position sensitive LYNXEYE detector

(Ni-filtered Cu-K α radiation). A step size of 0.01° and a counting time of 0.3 s were applied. Samples were finally dispersed with ethanol on a glass disk inserted in a round PMMA holder. The latter was subjected to gentle rotation during scanning. To verify the structure and calculate the lattice parameters a Rietveld refinement was performed using the TOPAS software (Bruker Corporation).^[4]

To examine the catalysts after the electrochemical measurement, the samples were recovered from the glassy carbon electrode with a commercial adhesive tape (Scotch Magic™ Tape, Minnesota Mining and Manufacturing Company). After applying the catalyst on the adhesive site the prepared tape was fixed on a glass disk in a round PMMA holder and measured by using the above mentioned setup with a step size of 0.01° and a counting time of 2.96 s.

Morphological characterization and BET surface determination

High-resolution SEM images were taken with a JEOL JSM7500F equipped with a cold-field emission gun. An acceleration voltage of 5.0 kV and an emission current of 10 μ A were applied. All experiments were performed under high vacuum. Samples were fixed on the metallic holder by using a conductive carbon paste. For determining the BET surface N₂ physisorption experiments were performed at -196 °C with a NOVA 3200e (Quantachrome GmbH & Co. KG) after degassing the samples at 80 °C for 2 h in vacuum. BET surface areas were calculated from p/p₀ data between 0.05 and 0.3.

Thermogravimetric analysis and temperature programmed oxidation (TPO)

Thermogravimetric analysis (TG) was carried out with a Netzsch STA 449 F3 Jupiter analyzer. Powdered sample (~ 50 mg) was placed in a corundum crucible and heated from room temperature to 1000 °C. A heating rate of 5 °C min⁻¹ and a mixture of 21 % O₂ in Argon at a flowrate of 100 mL min⁻¹ were applied.

The temperature programmed oxidation was conducted in a fully automated fixed bed flow set-up equipped with a GAM400 quadrupole mass spectrometer from InProcess. The experiment was performed in a quartz reactor which was heated by a ceramic oven from HTM Reetz GmbH. 100 mg sample was fixed between quartz wool and diluted with 400 mg inert SiC (particle size: 300 μ m). The gas purity was 4.5 O₂ in 4.7 He for the oxygen supply and 5.0 for the He supply.

Atomic absorption spectroscopy (AAS)

The metal content of the as-prepared samples was determined by atomic absorption spectroscopy (Thermo Electron Corporation, M-Series) after dissolving the powders in hydrochloric acid.

3.3.3 Electrocatalysis

The electrochemical measurements were carried out in a cell with three-electrode setup and a 1 M KOH solution as the electrolyte. An Autolab potentiostat/galvanostat (PGSTAT12, Eco Chemie, Utrecht, The Netherlands) coupled to a Metrohm RDE rotator (1600 rpm) was used. The glassy carbon tip of the working electrode had a geometric area of 0.126 cm². As reference electrode and counter electrode acted Ag/AgCl/3 M KCl and platinum foil. The catalyst ink was prepared by dispersing 2.5 mg of the catalyst in 2 μ l nafion, 249 μ l ethanol and 249 μ l water followed by 15 min ultrasonication. 5.0 μ l of the ink was drop coated onto the polished glassy carbon electrode and dried in air at room temperature for about 2 h. The modified electrodes were subjected to continuous potential cycling until reproducible voltammograms were obtained before catalytic measurements. Electrochemical impedance spectroscopy was then recorded in the frequency range from 50 kHz to 1 Hz at the corresponding open circuit potential of the electrode, using an AC perturbation of 10 mV. The resistance of the solution was determined from the resulting Nyquist plot and used for iR drop correction. All reported current densities were calculated using the geometric surface area of the electrode. The measured potentials were converted to the reversible hydrogen electrode (RHE) scale.^{[78][79]}

3.4 Results and Discussion

3.4.1 Characterization

Structural analysis

The success of synthesis was verified by PXRD measurements. The XRD patterns (Figure 3.2) indicate phase pure highly crystalline samples. The structural data were refined by the Rietveld method.^[4] The graphical results are depicted in Figure S3.3. The obtained lattice parameters, the integral breadth based volume-weighted column heights (LVol-IB) and selected structural information are shown in Table 3.1. The sample Calc.- α - MnO_2 wasn't refined satisfactorily and is not listed in the table. A more detailed description of the Calc.- α - MnO_2 sample can be found in the next chapter "Synthesis of Calc.- α - MnO_2 by thermal treatment of α - MnO_2 ". The refined lattice parameters of the different manganese oxide samples are similar to values described in literature and confirm the targeted lattice identity of the synthesized phases.^{[26][34][67][72][73][77][80][81][82]} Noteworthy is the varying parameter a within the hollandite-group in dependence of the incorporated tunnel cation. Surprisingly, the α - MnO_2 which is free of any foreign cation reveals the largest parameter and thus the largest unit cell whereas the Cryptomelane containing potassium shows the smallest unit cell.

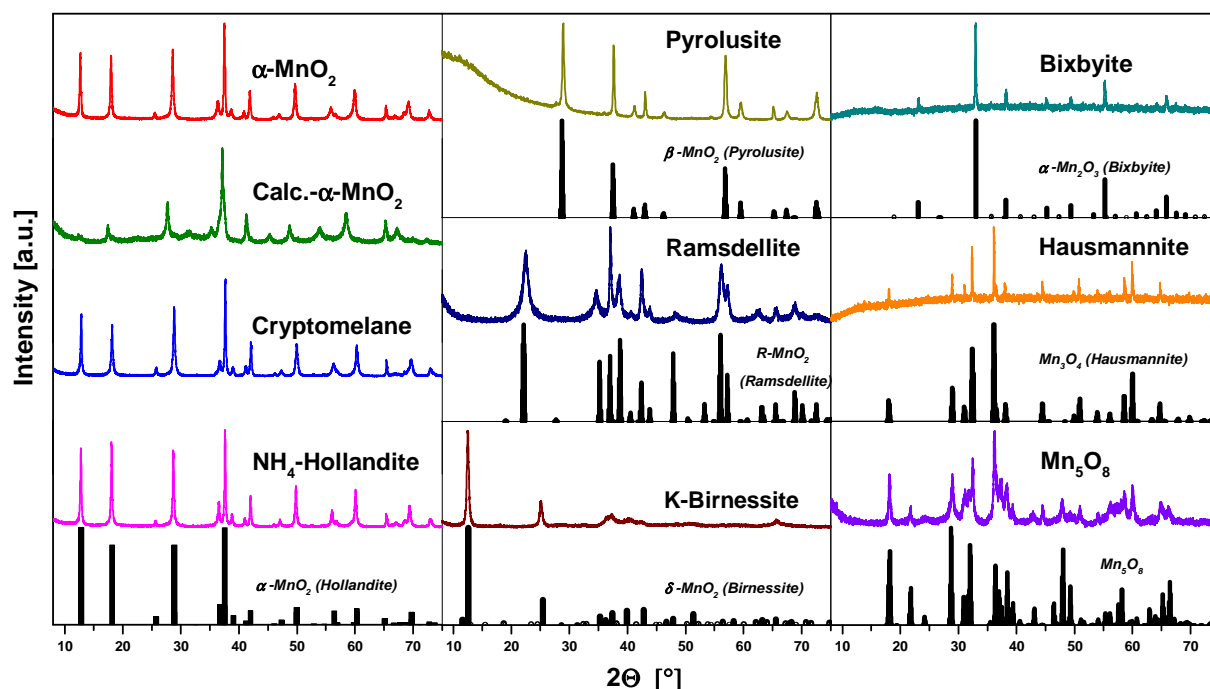


Figure 3.2. XRD pattern of different manganese oxides and the corresponding reference pattern (black): α - MnO_2 ^[34], β - MnO_2 ^[80], R- MnO_2 ^[26], δ - MnO_2 ^[111], α - Mn_2O_3 ^[112], Mn_3O_4 ^[67], Mn_5O_8 ^[70].

Table 3.1. Structural data, lattice parameter and volume-weighted mean column height ($LVol-IB$) of different manganese oxide samples obtained by Rietveld refinement.

<i>Sample</i>	α - MnO_2	<i>Cryptomelane</i>	<i>Bixbyite</i>
<i>Structure type</i>	Hollandite	α - MnO_2	Bixbyite- Mn_2O_3
<i>Crystal system</i>	tetragonal	tetragonal	cubic
<i>Space Group</i>	I 4/m (87)	I 4/m (87)	I a -3 (206)
<i>Formula Units/Cell</i>	8	8	16
<i>Lattice parameter</i> & <i>LVol-IB</i>	a = b = 9.8715(4) Å c = 2.8541(2) Å $\alpha = \beta = \gamma = 90^\circ$ LVol-IB = 20.49(19) nm	a = b = 9.8062(19) Å c = 2.8526(5) Å $\alpha = \beta = \gamma = 90^\circ$ LVol-IB = 48(9) nm	a = b = c = 9.407(3) Å $\alpha = \beta = \gamma = 90^\circ$ LVol-IB = 49.2(9) nm
<i>Sample</i>	<i>NH₄-Hollandite</i>	<i>Pyrolusite</i>	<i>Hausmannite</i>
<i>Structure type</i>	Hollandite	Rutile	$CdMn_2O_4$
<i>Crystal system</i>	tetragonal	tetragonal	tetragonal
<i>Space Group</i>	I 4/m (87)	P 4 ₂ /m n m (136)	I 4 ₁ /a m d (141)
<i>Formula Units/Cell</i>	8	2	4
<i>Lattice parameter</i> & <i>LVol-IB</i>	a = b = 9.8498(14) Å c = 2.8524(4) Å $\alpha = \beta = \gamma = 90^\circ$ LVol-IB = 23.4(3) nm	a = b = 4.404(4) Å c = 2.872(2) Å $\alpha = \beta = \gamma = 90^\circ$ LVol-IB = 25(2) nm	a = b = 5.7628(11) Å c = 9.4728(18) Å $\alpha = \beta = \gamma = 90^\circ$ LVol-IB = 23.4(3) nm
<i>Sample</i>	<i>Ramsdellite</i>	<i>K-Birnessite</i>	<i>Mn₅O₈</i>
<i>Structure type</i>	VO_2	-	$Cd_2Mn_3O_8$
<i>Crystal system</i>	orthorhombic	orthorhombic	monoclinic
<i>Space Group</i>	P b n m (62)	C m c m (63)	C 1 2/m 1 (12)
<i>Formula Units/Cell</i>	4	4	2
<i>Lattice parameter</i> & <i>LVol-IB</i>	a = 4.462(9) Å b = 9.480(18) Å c = 2.861(5) Å $\alpha = \beta = \gamma = 90^\circ$ LVol-IB = 7.25(8) nm	a = 4.685(4) Å b = 2.839(2) Å c = 14.247(11) Å $\alpha = \beta = \gamma = 90^\circ$ LVol-IB = 14.5(2) nm	a = 10.156(17) Å b = 5.780(10) Å c = 4.875(8) Å $\alpha = \gamma = 90^\circ$ $\beta = 109.609 (15)^\circ$ LVol-IB = 7.25(8) nm

Synthesis of Calc.- α -MnO₂ by thermal treatment of α -MnO₂

The α -MnO₂ sample which was synthesized by acid digestion of Bixbyite was characterized by thermogravimetric analysis (TGA) and temperature programmed oxidation (TPO) analysis (Figure 3.3). The structure at different temperatures was determined by a subsequently external XRD analyses. As depicted in the TG Graph, three different mass loss steps occur up to a temperature of 600 °C. The first mass loss at about 100 °C can be attributed to the loss of re-adsorbed surface water. The third mass loss at about 550 °C indicates the expected oxygen

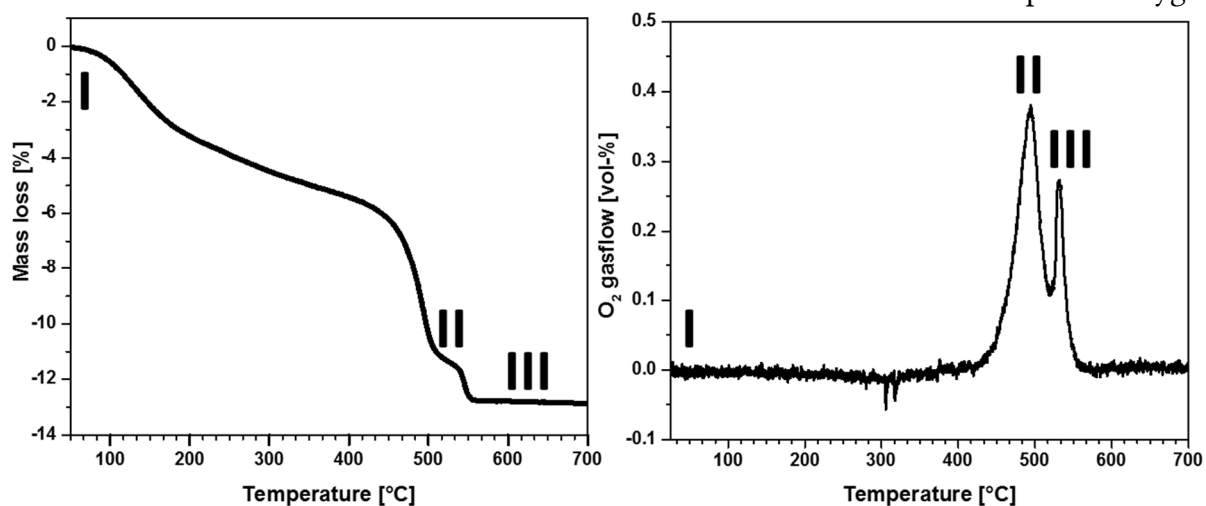


Figure 3.3. Graphs of thermogravimetric (left) and temperature programmed oxidation analysis (right) of α -MnO₂.

loss due to the phase change to Mn₂O₃ (Bixbyite). Surprisingly, the thermal reduction and phase change of α -MnO₂ to Bixbyite does apparently proceed via an intermediate phase, which was also verified by the TPO experiment. This intermediate is labelled Calc.- α -MnO₂ in the following. The narrow plateau after the second feature suggests that Calc.- α -MnO₂ is stable up to 550 °C. A sample for further investigations was obtained by the calcination of α -MnO₂ at 475 °C in a muffle furnace. The oxygen contents of the as prepared α -MnO₂, the Bixbyite (gained from the treatment at 550 °C) and the Calc.- α -MnO₂ were determined by AAS and additionally by TPO. Both methods led to similar results (Figure 3.4). The amount of oxygen in Calc.- α -MnO₂ ranges between those of α -MnO₂ and Bixbyite. The XRD analysis of Calc.- α -MnO₂ reveals a crystalline phase which can't be clearly assigned to α -MnO₂, Bixbyite or another known phase. SEM revealed that the morphology of the Bixbyite phase is surprisingly similar to the one of Calc.- α -MnO₂ (Figure 3.4) showing a rod-cluster, while the α -MnO₂ starting phase consisted mostly of needles. The Bixbyite precursor which was synthesized by calcination of Mn(III) acetate and used for the acid digestion route to α -MnO₂ shows a completely different morphology (Figure S3.2), suggesting that the shaping of Bixbyite is strongly related to its precursor. As seen in the XRD pattern in Figure 3.4, the Calc.- α -MnO₂ reflections

start to appear at 455 °C beside the main phase reflections of α -MnO₂. The phase fraction of Calc.- α -MnO₂ increases up to phase pureness at 475 °C. The temperature range for a pure Calc.- α -MnO₂ is small and ends at around 495 °C with the evolving of Bixbyite. To gain a

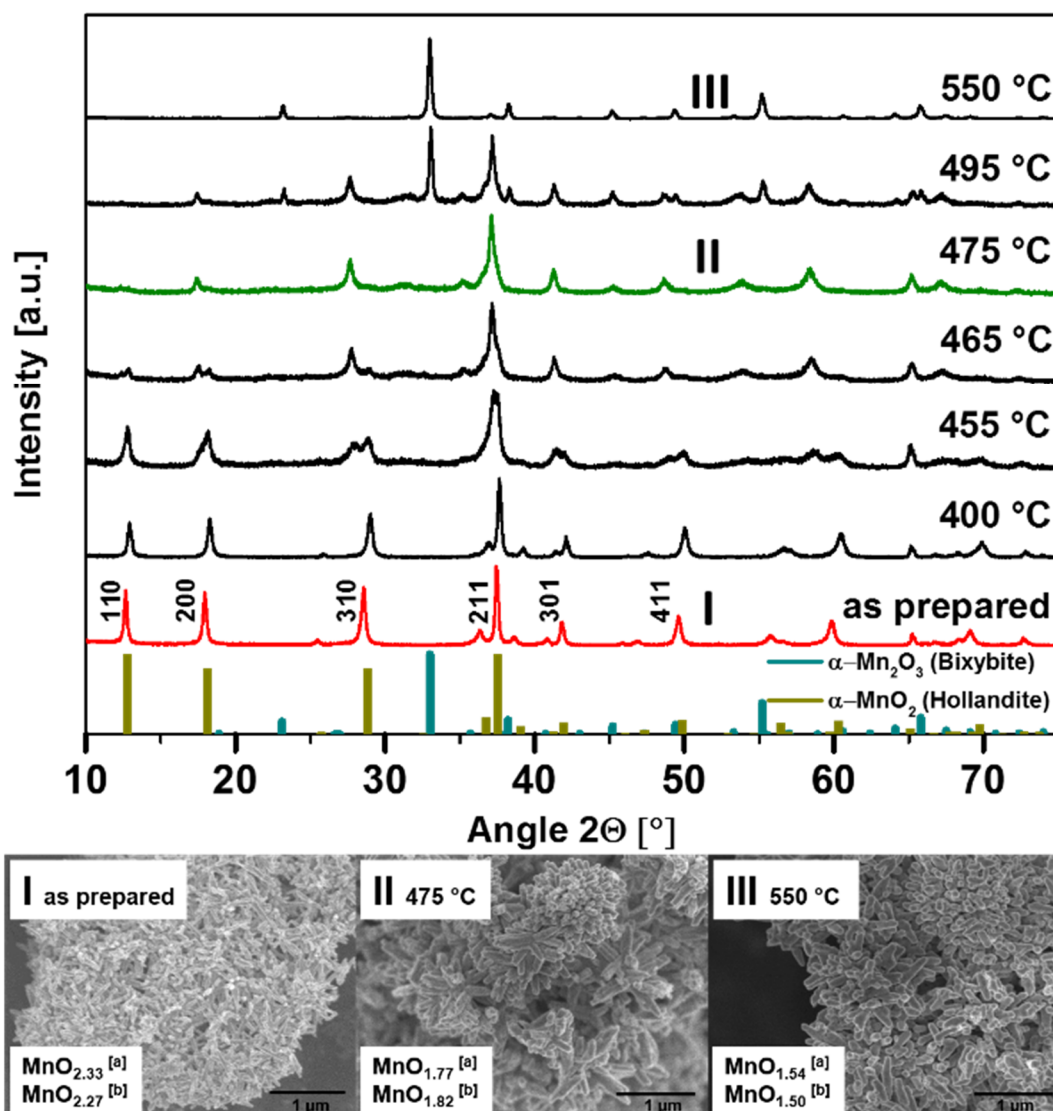


Figure 3.4. XRD pattern (above) of α -MnO₂ calcined at selected temperatures and related Scanning electron micrographs (below). The oxygen content was [a] calculated from the difference to 100 % of the total elemental composition detected by atomic absorption spectroscopy, [b] determined by temperature programmed oxidation assuming a phase-pure Mn₃O₄ sample at 1000 °C.

deeper understanding of the structural changes in α -MnO₂ due to the applied temperature a Rietveld refinement of the powder data was performed. The lattice parameters are shown in Table S3.2 and depicted in Figure 3.5. The unit cell distorts during calcination. Until a temperature of 400 °C a gradual decrease in the a/b parameter and an increase in the c parameter were observed. Starting at 455 °C a two phase system forms in which the α -MnO₂ phase still exhibits an increasing c parameter. However, the a/b parameter just shows small changes.

Like mentioned before, the reflections and the structure of Calc.- α - MnO_2 can't be interpreted properly and further structural investigations are required.

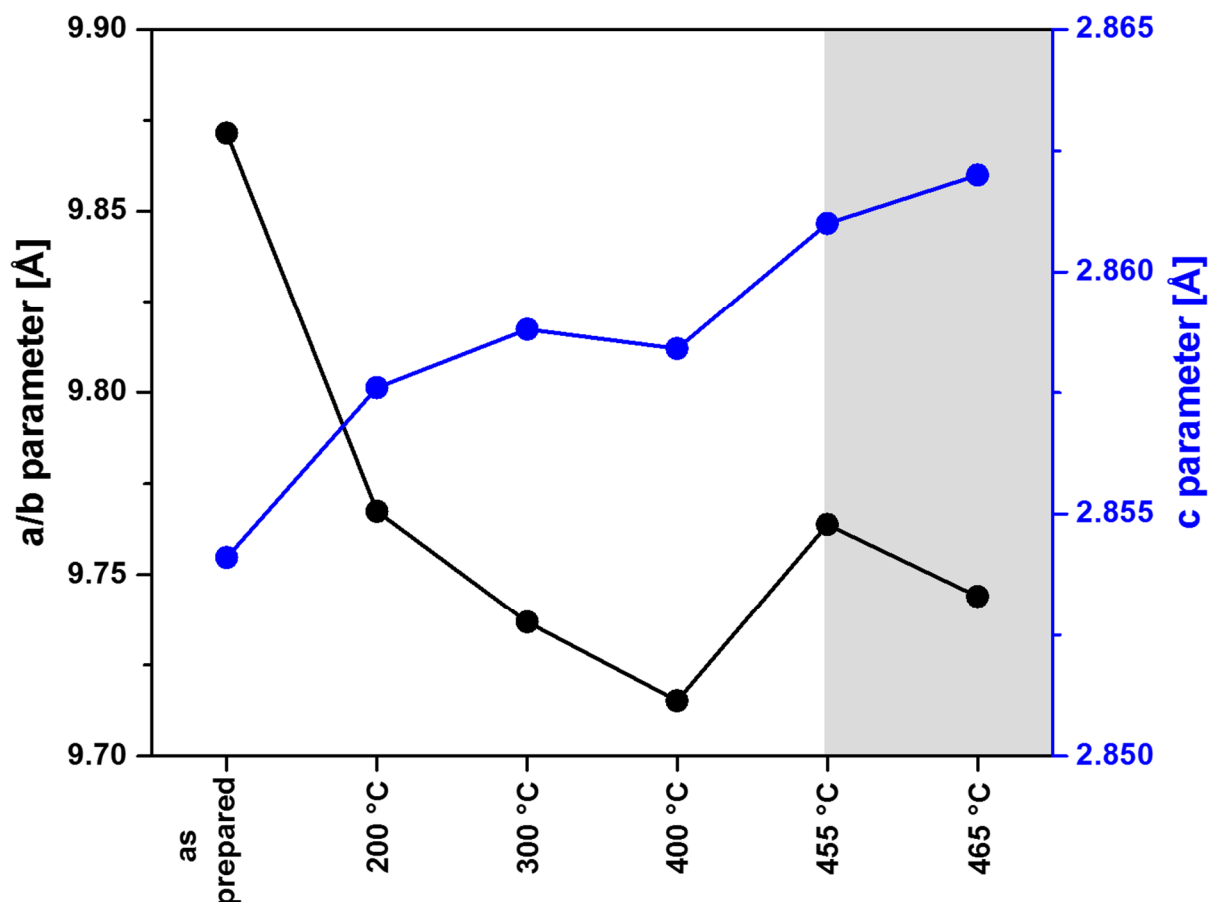


Figure 3.5. Calculated lattice parameters of α - MnO_2 samples calcined at different temperatures. Grey area: presence of two phases.

Morphological, textural and elemental analysis

Scanning Electron Microscopy Images (Figure 3.6) were recorded from all samples. Except the K-Birnessite all MnO_2 -polymorphs show a rod-shape morphology. K-Birnessite, Bixbyite and Mn_5O_8 develop sponge-like aggregates whereas Hausmannite crystallizes in an isotropic, faceted shape. All samples exhibit a low to moderate BET surface area between 1 and $42 \text{ m}^2\text{g}^{-1}$. The calculated elemental composition is in most cases located closely to the ideal one. Deviating compositions can be caused by varying water content and flexible oxidation states of manganese. Especially the tunneled (hollandite-group) and layered (Birnessite) manganese oxides show this variability. Interestingly the same amount (related to manganese) NH_4^+ was incorporated in the NH_4 -Hollandite like K^+ in the Cryptomelane (K-Hollandite).

Probably a foreign cation/manganese atomic ratio of 10 % is the preferred one in the tunnel structure of the hollandite-type in contrast to K-Birnessite, which is obviously able to insert higher amounts of potassium between its layers.

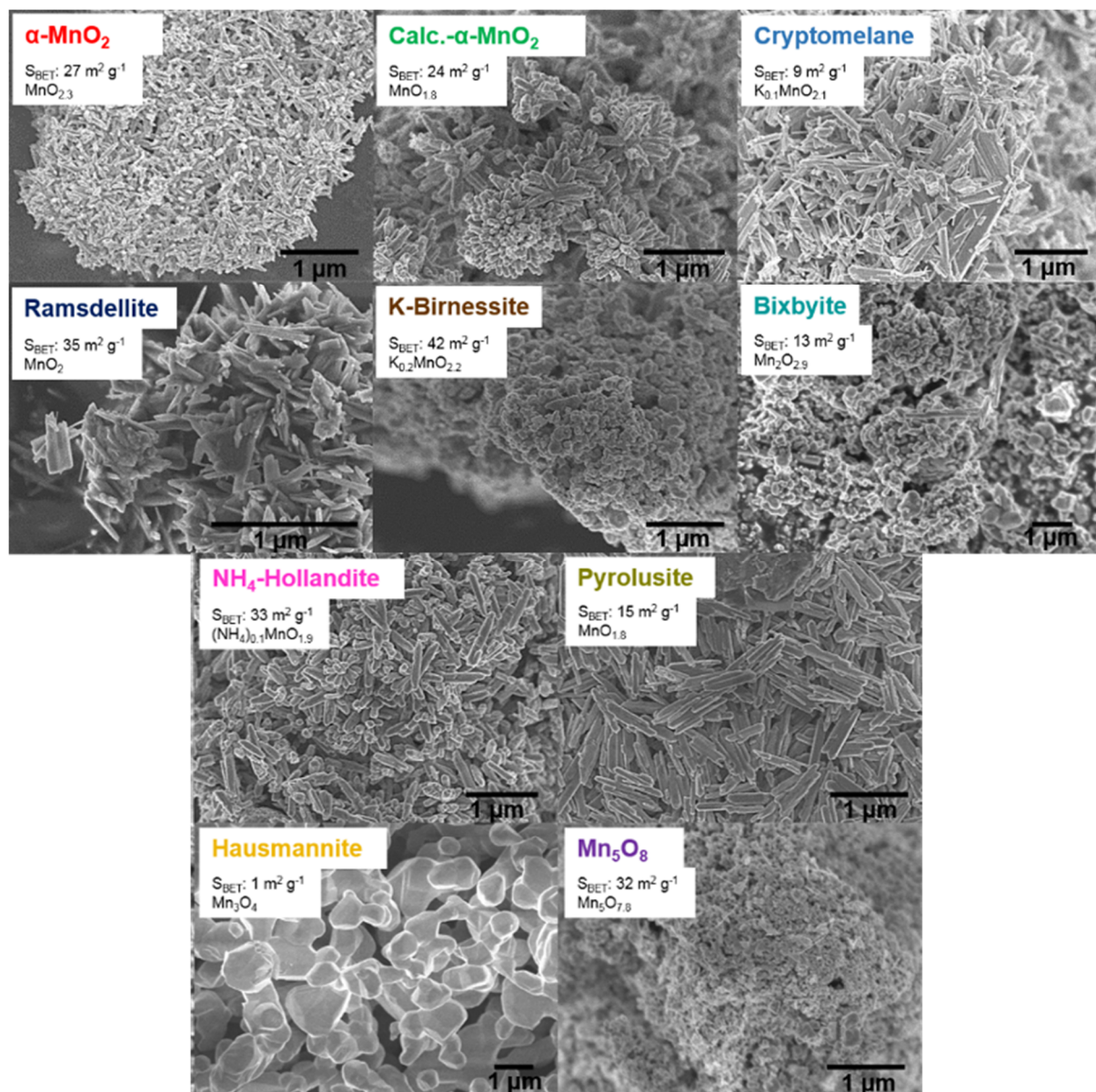


Figure 3.6. Scanning electron micrographs, BET surface areas and chemical formulas of different manganese oxide samples. The oxygen content was calculated from the difference to 100 % of the total elemental composition detected by atomic absorption spectroscopy.

Thermogravimetric analysis

All synthesized samples were characterized by thermogravimetric analysis (Figure 3.7). For a deeper understanding and to identify the phases at selected temperatures, an external XRD analysis was performed after calcination of the samples at characteristic temperatures. The resulting XRD patterns are depicted in Figure S3.4. Foreign metal cation free manganese oxides exhibit two prominent phase transitions while thermal treatment in air: The transformation to Bixbyite at 500-600 °C (except Bixbyite itself) and the transformation to Hausmannite at 900-1000 °C. The transition of α - MnO_2 and Mn_5O_8 to Bixbyite exhibit a shoulder in the TGA profile suggesting formation of an intermediate. The case of α - MnO_2 was explained in detail in the chapter “Synthesis of Calc.- α - MnO_2 by thermal treatment of α - MnO_2 ”.

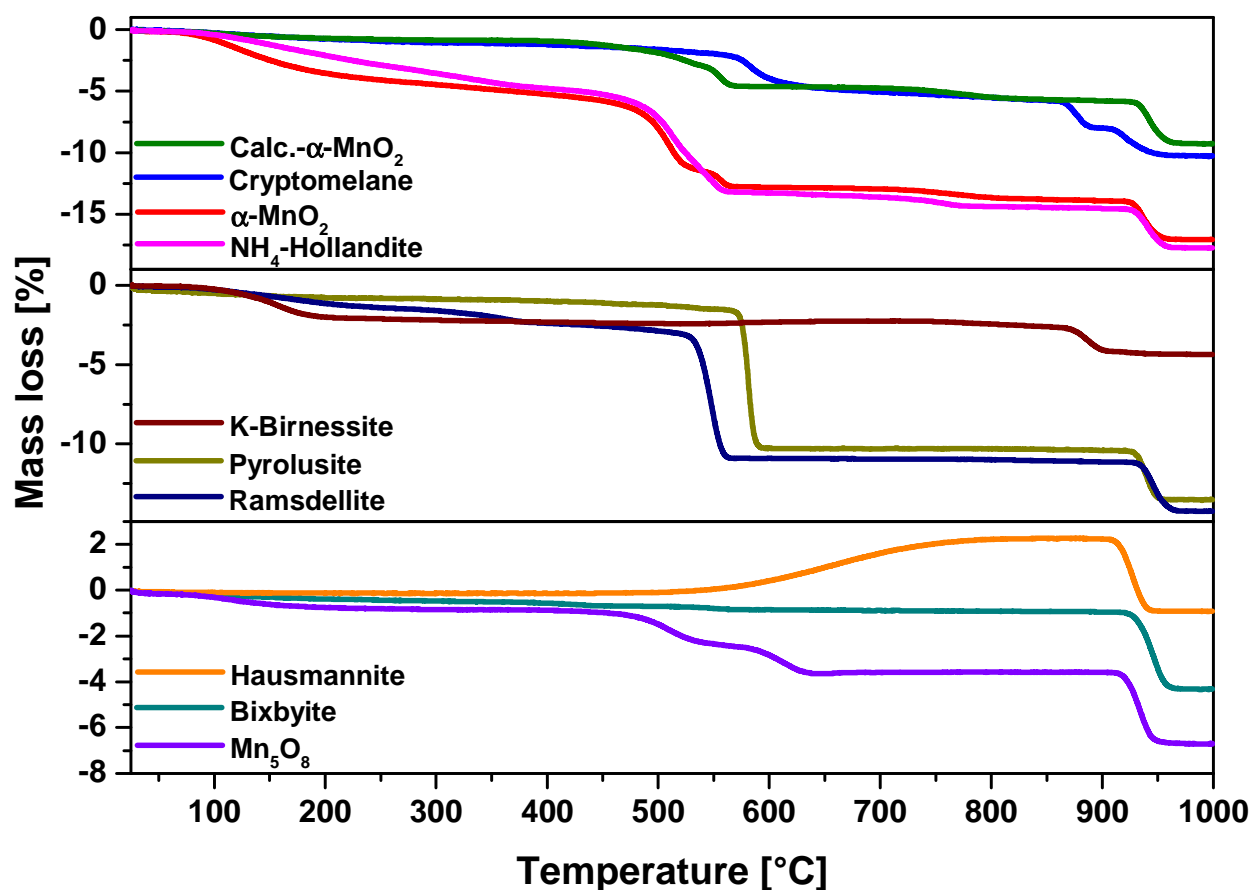


Figure 3.7. Thermogravimetric analysis of different manganese oxides.

The XRD pattern of Mn_5O_8 calcined at 500 °C still indicates a pure Mn_5O_8 phase. However slight changes in the intensity of some reflections leads to an even better resemblance to the literature pattern. Noteworthy, the thermal behavior of NH_4 -Hollandite differs to the one of α - MnO_2 . The main features occur at the same temperature however the NH_4 -Hollandite do not transform to Bixbyite via an intermediate phase although the only structural difference lies in the presence of NH_4^+ ions. It may be hypothesized that the NH_4^+ ions stabilize the

tunneled structure up to the first feature and allow a direct transition to Bixbyite likely under emission of NH_3 . The potential stabilizing effect of the foreign cations can also be seen in the thermal decomposition of Cryptomelane, which is stable up to a higher temperature of approximately 600 °C. In general, Cryptomelane and K-Birnessite show a different thermal behavior than the “pure” manganese oxides. This is caused by the potassium which cannot be incorporated into the dense structures of Bixbyite and Hausmannite. Thus, the presence of a potassium rich phase is unavoidable. The TG graph of Cryptomelane exhibits three features. The first one at about 600 °C is caused by the development of a Bixbyite phase in addition to Cryptomelane. The second one at 850 °C by the formation of a two phase system consisting of K-Birnessite and Bixbyite and the third one at 950 °C by the transformation to a mixture of K-Birnessite and Hausmannite. The TG graph of K-Birnessite reveals a dissimilar course. The first feature at a very low temperature at 100-200 °C could be reasoned with the loss of water, likely from the interlayers, however the K-Birnessite structure remains stable. Although no larger change in mass occurs a two phase system develops due to calcination. The XRD pattern recorded of a sample obtained at 700 °C shows the existence of a hollandite-type phase (probably Cryptomelane) next to a birnessite-like phase. This phase reveals a strong shift of the major Birnessite reflection from $12.6 \ 2\theta$ to $7.1 \ 2\theta$ indicating an increase in the interlayer distance. That could be reasoned by a slight atomic reordering to a structural related phase like Buserite but also just by an enlargement of the K-Birnessite unit cell.^{[25][83][84][85]} Surprisingly the last mass loss at about 850 °C resulted in a Birnessite phase with unchanged interlayer distance regarding the as prepared sample. Additionally to the Birnessite, a Hausmannite phase was detected.

3.4.2 Electrocatalysis

OER activity

An OER activity screening of the synthesized samples was performed. As seen in the rotating disk electrode voltammograms (Figure 3.8 A and B) the ability of the manganese oxide samples to catalyze the oxygen evolution reaction differs substantially. Measurements of a mixed nickel cobalt oxide benchmark (99 % p.a., Sigma-Aldrich Chemie GmbH) show that the electrocatalytic activities of manganese oxides are rather low, compared to other transition metal oxides. The highest activity can be attributed to Cryptomelane followed by the other members of the hollandite-group. However a big variation in activity can be observed within this group.

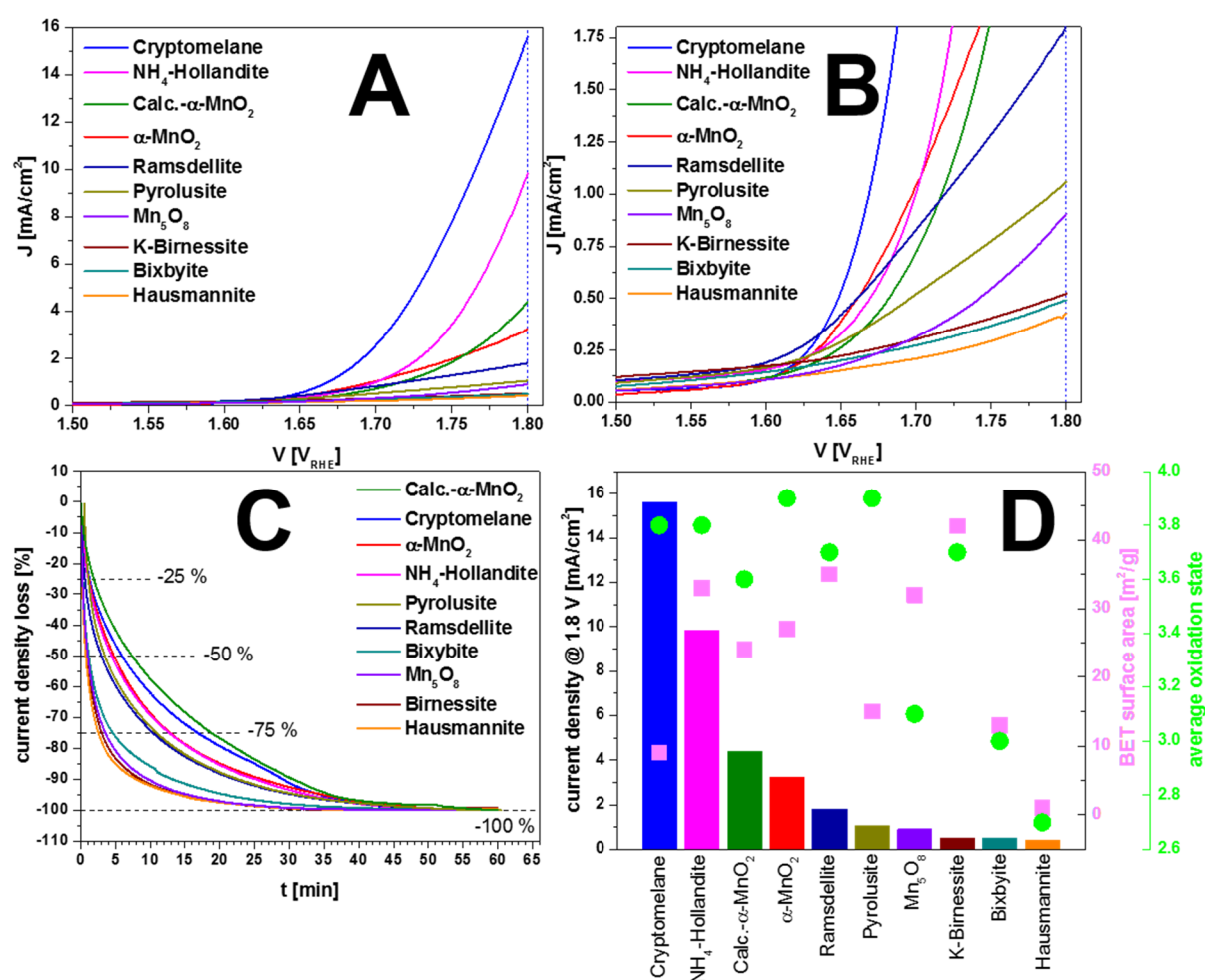


Figure 3.8. OER activities of manganese oxides, A and B: rotating disk electrode voltammograms, C: loss of current density during long-time measurement at 1.8 V, D: Current density at 1.8 V and the manganese oxide related BET surface area and average oxidation state. The oxidation states of Cryptomelane, α -MnO₂, R-MnO₂, Pyrolusite, K-Birnessite, Bixbyite and Hausmannite are based on literature data.^[10] The oxidation state of NH₄-Hollandite is orientated on Cryptomelane, the one of Calc.-Hollandite and Mn₅O₈ was calculated from AAS measurements.

α -MnO₂ reaches a current density of about 3 mA cm⁻² at a potential of 1.8 V what is approximately just 20 % of the value achieved by Cryptomelane (> 15 mA cm⁻²). The Calc.- α -MnO₂ obtained by the thermal treatment of α -MnO₂ exhibits a slightly higher activity than the α -MnO₂ itself. Surprisingly the insertion of NH₄⁺ ions into the α -MnO₂ tunnels enhanced the activity to 10 mA cm⁻² at a potential of 1.8 V representing the second highest value of this screening. If the higher activity of Cryptomelane and NH₄⁺-Hollandite in comparison to the pure α -MnO₂ is caused by the tunnel-ions, the synthesis method or an unknown parameter remains unclear and further investigations are needed. It is noted that the electrolyte contained a high concentration of potassium enabling an incorporation of K⁺ in the tunnels during operation. For a better distinction of the low active manganese oxides a zoom-in is depicted in Figure 3.8 B. Mn₅O₈, K-Birnessite, Bixbyite and Hausmannite exhibit a current density of less than 1 mA cm⁻² at a potential of 1.8 V and may be described as nearly inactive.

The onset potential of the active manganese oxides is seen to be rather similar. The major difference lies in the slope of the curves after the onset. This observation suggests that the variations may not be caused by the chemical species alone, but to some extent also by differences in conductivity. Comparison of the activities with the oxidation states of manganese in the as-prepared samples (Figure 3.8 D) shows that all highly active samples contain Mn in a high oxidation state. At the same time, a high oxidation state alone is not enough to obtain high activity as seen e.g. for Birnessite. Likely, conductivity problems hinder the electrocatalytic performance despite a favorable oxidation state in this case. A significant correlation of the BET surface area with the activity is not observable (Figure 3.8 D). Frey et al. investigated the catalytic activity of various manganese oxides in the water oxidation catalysis (WOC) using Ce⁴⁺ as chemical oxidising agent.^[10] The group reported a higher activity of oxides with tunnel structure like Cryptomelane compared to oxides with dense structure like Hausmannite which was also observed in this study. Noteworthy differences between the results of the WOC and the OER experiments can be found in the activity of K-Birnessite representing an oxide with layer structure. Frey et al. showed that the WOC activity of K-Birnessite is similar to the one of Cryptomelane while the K-Birnessite exhibited a much lower activity in the OER experiments conducted in this study. This may be caused by the different measurement methods and conditions, which possibly change the influence of different material properties on the catalytic performance. The activity trend within the group of samples containing manganese with an oxidation state near +4 was also reported by Meng et al. who compared the OER performance in 0.1 molar KOH of Cryptomelane, Pyrolusite and Birnessite.^[86] The group identified Cryptomelane as most active catalyst followed by Pyrolusite and Birnessite.

Stability

To judge the stability during reaction the potential was held at 1.8 V for a duration of about 1 hour. To compare the results, the current density was normalized and is expressed as relative loss of current density in percent (Figure 3.8 C). All manganese oxide samples exhibit a fast decrease in activity from the beginning. After 10 min the activity loss amounts to at least 50 % and after 60 min to 100 % of the respective starting value. Interestingly the stability trend is similar to the one of the activity. Thus, the current density loss within the hollandite-group is slower than for the low active catalysts like Bixbyite, Mn_5O_8 , K-Birnessite or Hausmannite. In summary, however, it must be stated that the manganese oxides are unstable under the conditions applied here.

3.5 Conclusion

Ten manganese oxide phases differing in structure and/or composition were synthesized and characterized by Rietveld refinement of X-ray diffraction data, N_2 physisorption experiments, scanning electron microscopy, thermogravimetric analysis and atomic absorption spectroscopy. Additional to nine common manganese oxides, which were clearly identified, the tenth phase was obtained by thermal treatment of α - MnO_2 . A screening of all MnO_x samples regarding their electrocatalytic OER performance was conducted. The OER measurements indicate strong differences in activity. The most active catalysts can be found within the hollandite-type oxides containing Mn in an oxidation state near +4. Cryptomelane reaches a current density of over 15 mA cm^{-2} at a potential of 1.8 V. In contrast to Hausmannite, Bixbyite and K-Birnessite which were not even able to surpass a value of 1 mA cm^{-2} . No linear dependence of the average manganese oxidation states or the BET surface area on the OER activity was observed. All manganese oxides were unstable and completely lost their performance within 1 hour.

3.6 Acknowledgement

The authors acknowledge the Financial support of the BMBF funded project MANGAN (FKZ: 03SF0511B) and the collaboration with the related working groups. The authors also sincerely

thank Fatih Özcan for providing the presented SEM images and Niklas Cibura (MPI CEC) for carrying out the TPO experiment of the α - MnO_2 sample.

3.7 Supporting information

Table S3.1. Quality factors of Rietveld refinement of different samples.

Sample	R_{exp}	R_{wp}	R_p	R_{exp}'	R_{wp}'	R_p'	GOF	R_{Bragg}
α - MnO_2 as prepared	9.03	19.20	14.79	7.45	15.85	12.70	2.13	10.312
α - MnO_2 calcined at 200 °C	8.91	19.02	14.79	7.03	14.99	12.14	2.13	7.227
α - MnO_2 calcined at 300 °C	9.96	21.14	16.41	7.59	16.09	13.28	2.12	10.164
α - MnO_2 calcined at 400 °C	11.90	29.04	22.95	8.84	21.58	18.48	2.44	14.525
α - MnO_2 calcined at 455 °C	9.72	18.69	14.62	2.56	4.92	4.46	1.92	10.386
α - MnO_2 calcined at 465 °C	9.69	15.50	11.89	3.29	5.26	4.57	1.60	3.835
α - MnO_2 calcined at 475 °C	0.85	1.11	0.85	3.04	3.98	5.62	1.31	9.651

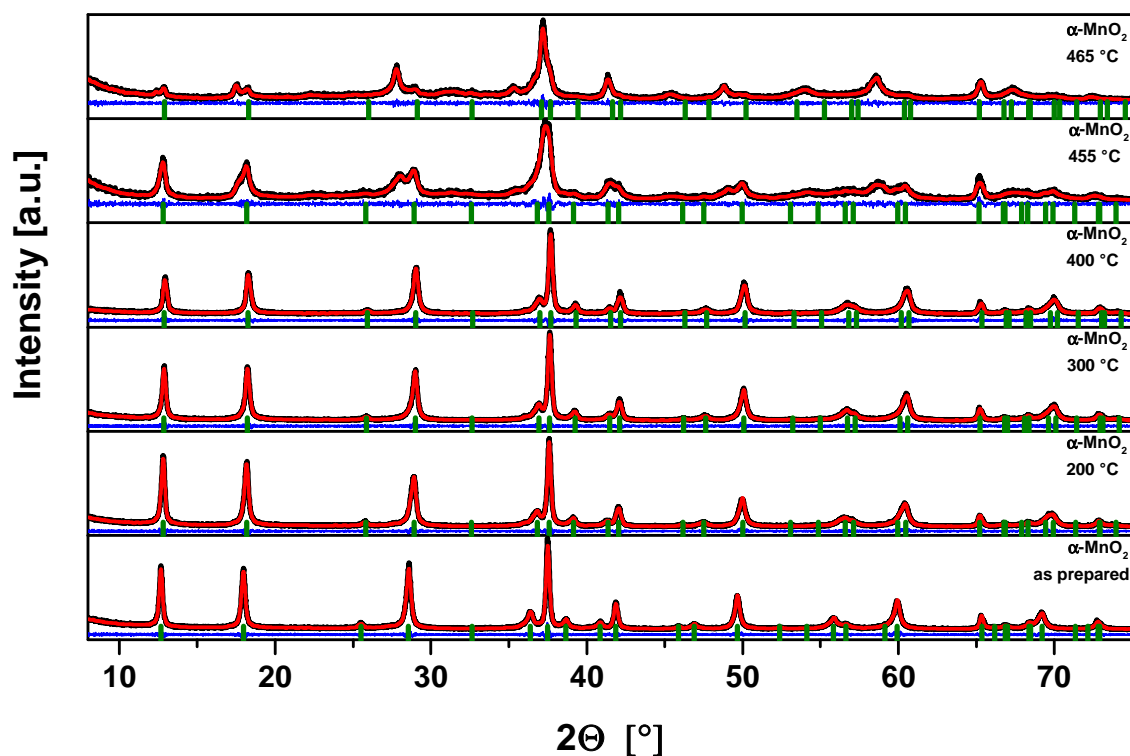


Figure S3.1. Graphical results of the Rietveld refinement of the powder diffraction data of α - MnO_2 samples calcined at different temperatures. Experimental data (black), calculated curve (red), and difference curve (blue). Position of Bragg reflections are indicated by green.

Table S3.2. Lattice parameters of α -MnO₂ samples calcined at different temperatures obtained by Rietveld refinement.

<i>Sample</i>	<i>α-MnO₂ as prepared</i>	<i>α-MnO₂ calcined at 200 °C</i>
<i>Lattice parameter</i>	a = b = 9.8715(4) Å c = 2.8541(2) Å $\alpha = \beta = \gamma = 90^\circ$	a = b = 9.7674(4) Å c = 2.8576(2) Å $\alpha = \beta = \gamma = 90^\circ$
<i>Sample</i>	<i>α-MnO₂ calcined at 300 °C</i>	<i>α-MnO₂ calcined at 400 °C</i>
<i>Lattice parameter</i>	a = b = 9.7369(5) Å c = 2.8588(3) Å $\alpha = \beta = \gamma = 90^\circ$	a = b = 9.7152(8) Å c = 2.8584(4) Å $\alpha = \beta = \gamma = 90^\circ$
<i>Sample</i>	<i>α-MnO₂ calcined at 455 °C</i>	<i>α-MnO₂ calcined at 465 °C</i>
<i>Lattice parameter</i>	<i>α-MnO₂ (Phase 1)</i>	<i>α-MnO₂ (Phase 1)</i>
	a = b = 9.7638(12) Å c = 2.8610(8) Å $\alpha = \beta = \gamma = 90^\circ$	a = b = 9.744(3) Å c = 2.862(2) Å $\alpha = \beta = \gamma = 90^\circ$

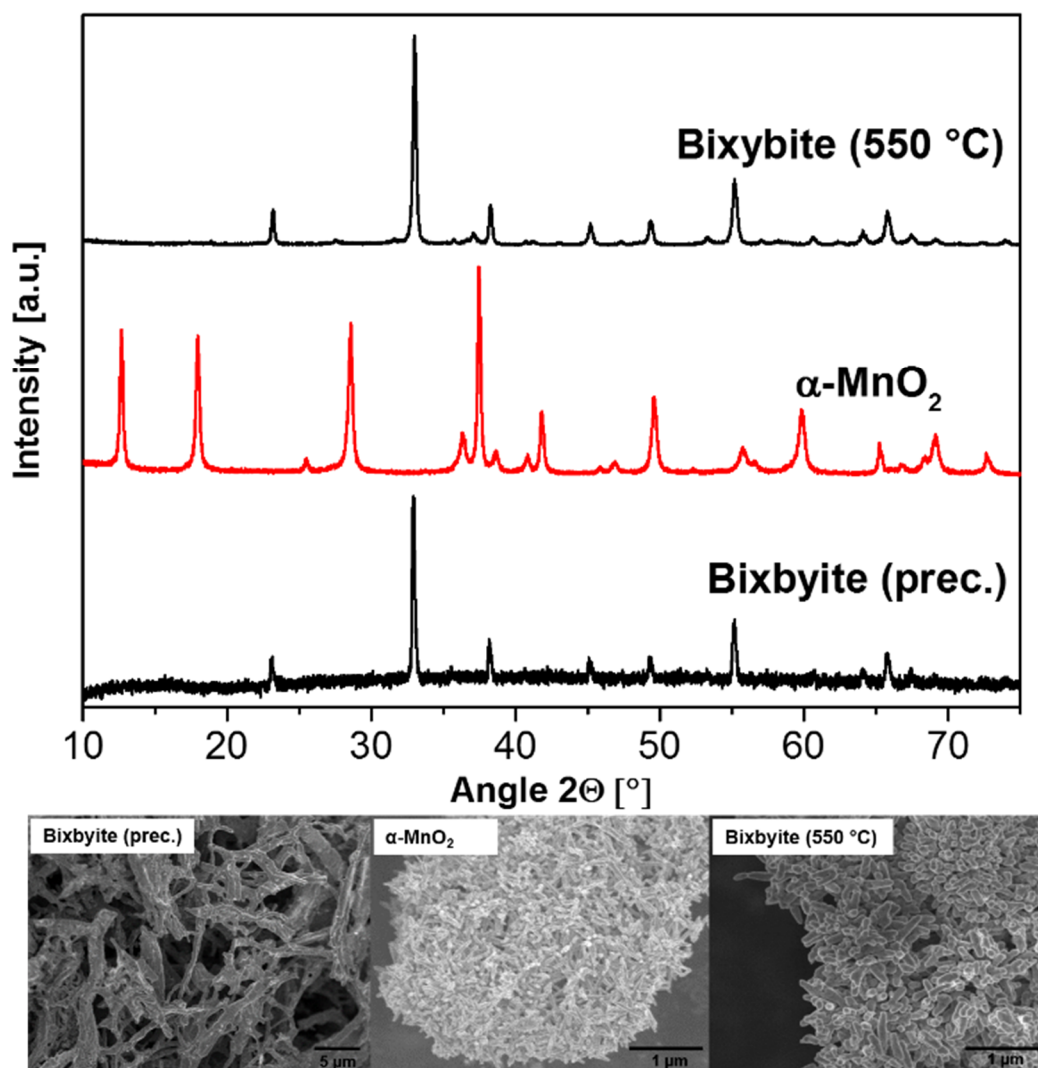


Figure S3.2. XRD pattern and related Scanning electron micrographs of Bixbyite prepared by calcination of Mn(III) acetate (Bixbyite (prec.)), α -MnO₂ synthesized by acid digestion of Bixbyite (prec.) and Bixbyite obtained by calcination of α -MnO₂ (Bixbyite (550 °C)).

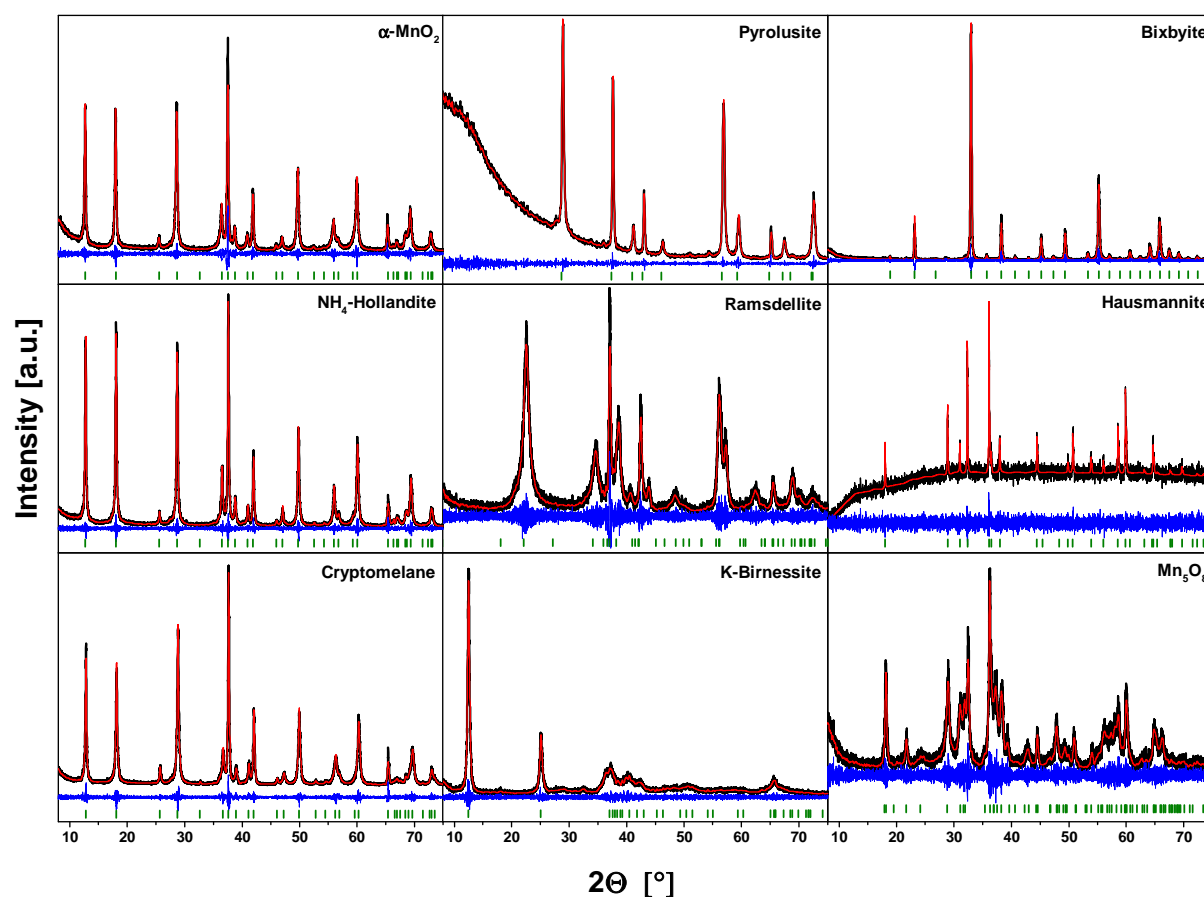


Figure S3.3. Graphical results of the Rietveld refinement of the powder diffraction data of different manganese oxide samples. Experimental data (black), calculated curve (red), difference curve (blue) and position of Bragg reflections (green).

Table S3.3. Quality factors of Rietveld refinement of different manganese oxide samples.

Sample	R_{exp}	R_{wp}	R_p	R_{exp}'	R_{wp}'	R_p'	GOF	R_{Bragg}
α -MnO ₂	9.03	19.20	14.79	7.45	15.85	12.70	2.13	10.312
Cryptomelane	10.43	11.78	8.41	8.12	9.17	7.08	1.13	1.557
NH ₄ -Hollandite	9.06	16.67	13.00	7.39	13.60	11.01	1.84	4.836
Pyrolusite	4.07	4.55	2.91	5.49	6.12	4.52	1.12	0.382
Ramsdellite	15.05	18.16	13.48	15.57	18.79	19.97	1.21	7.145
K-Birnessite	12.83	27.67	21.35	12.10	26.10	22.34	2.16	14.760
Bixbyite	14.77	18.83	13.42	5.91	7.53	6.62	1.27	6.604
Hausmannite	2.71	3.18	2.44	8.46	9.93	11.45	1.17	0.800
Mn ₅ O ₈	16.04	22.14	16.79	13.29	18.33	16.43	1.38	4.685

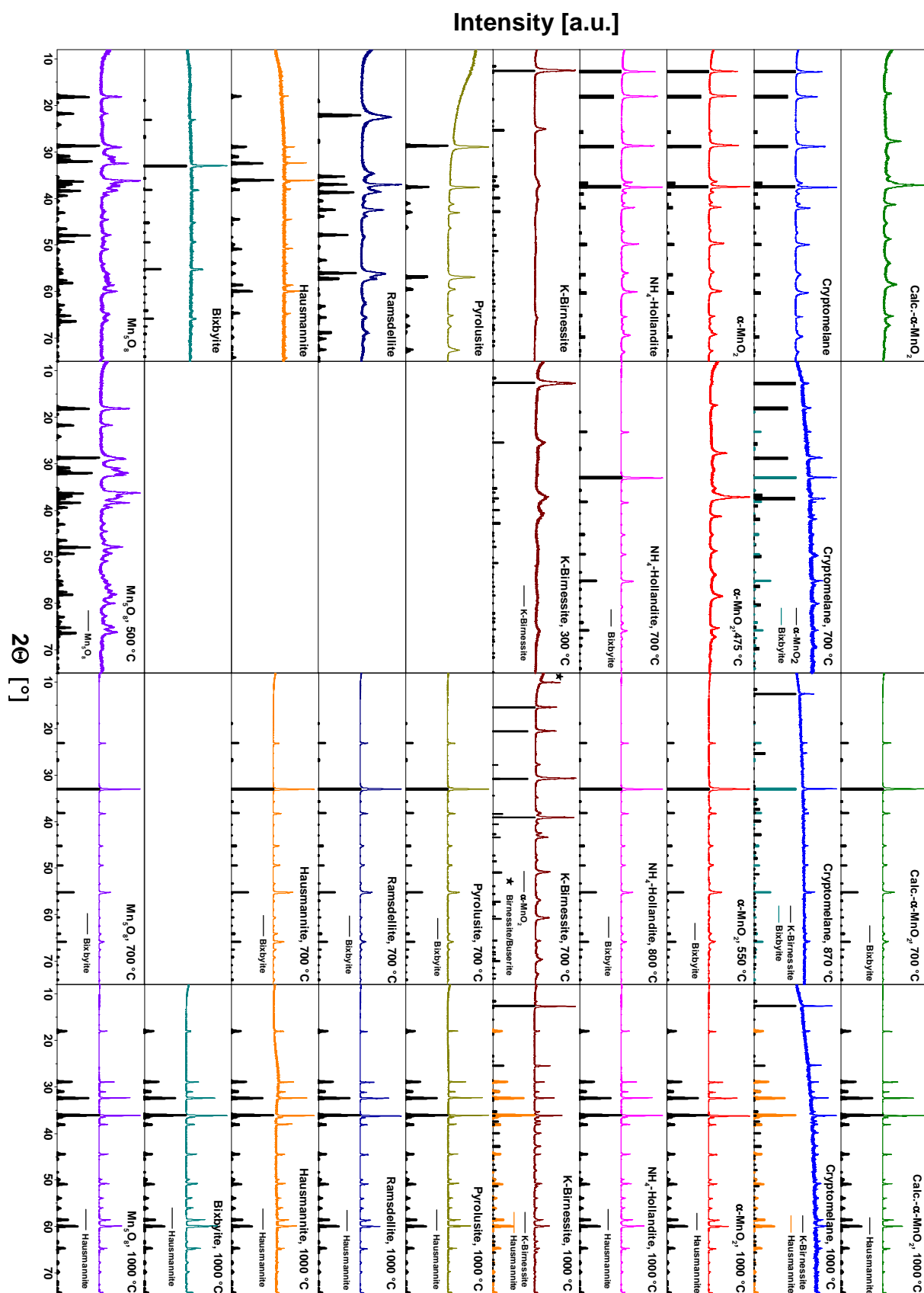


Figure S3.4. XRD patterns of different manganese oxides calcined at selected temperatures. Corresponding TG measurements are shown in Figure 3.7.

4. Cryptomelane as Water Oxidation Catalyst: Factors Influencing the OER Activity

Justus Heese-Gärtlein^[a], D. M. Morales^[b], W. Schuhmann^[b], Malte Behrens^{*[a]}

^[a] Faculty of Chemistry, Inorganic Chemistry
University of Duisburg - Essen and Center for Nanointegration Duisburg-Essen
Universitätsstr. 7, 45141 Essen, Germany

^[b] Analytical Chemistry - Center for Electrochemical Sciences Ruhr University Bochum
Universitätsstr. 150, 44780 Bochum, Germany

* Corresponding author (malte.behrens@uni-due.de)

Contributions of co-authors:

D. M. Morales: Measurement and Interpretation of the Raman Spectroscopy experiments.

W. Schuhmann: Advising support concerning the Raman Spectroscopy experiments.

M. Behrens: Advising, support and proofreading.

4.1 Abstract

Potassium containing α - MnO_2 (Cryptomelane) samples were synthesized by different routes and characterized in detail. XRD patterns indicate pure phases crystallizing in hollandite-type structure, which was confirmed by Raman spectroscopy. In dependence of the synthesis route textural, compositional and morphological properties vary in a large range. The particle shapes can be described as needle-like with varying mean aspect ratios. Electrocatalytic oxygen evolution reaction (OER), water oxidation catalysis (WOC) with Ce^{4+} as chemical oxidising agent and H_2O_2 decomposition experiments were carried out. Comparative measurements reveal a substantial influence of the synthesis method on the catalytic performance. The H_2O_2 decomposition and the WOC scale mainly with the BET surface area. In terms of OER, the impact factors aspect ratio and conductivity are much more important. Electrocatalytic stability measurements exhibit a strongly decreasing activity. However, the structural stability under the applied conditions is verified by operando Raman spectroscopy and subsequently performed XRD analysis.

4.2 Introduction

Various manganese oxides consisting of linked MnO_6 octahedra forming tunnels are known and well investigated such as Romanechite with 2x3 tunnels, Todorokite with 3x3 tunnels or Hollandite with 2x2 tunnels.^{[17][18][19][20][21][22][23][24]} Usually foreign cations are located in the tunnels.^[32] The preferred tunnel cation of Hollandite is potassium. The related mineral of the resulting K-Hollandite is called Cryptomelane. Already many years ago, Cryptomelane aroused interest among scientist.^[33] Several methods to synthesize Cryptomelane were developed by researchers around the world. In the following, only a few are named. The treatment of Mn_2O_3 (Bixbyite) with an acidic potassium ions containing solution leads to a precipitation of Cryptomelane.^{[72][87]} Golden et al. transformed δ - MnO_2 (Birnessite) to Cryptomelane by thermal treatment.^[88] Other well established routes are based on potassium permanganate, like refluxing^[17], hydrothermal treatment^[89] or a solvent-free calcination of a $\text{KMnO}_4/\text{Mn}^{2+}$ -salt mixture.^[90] The Hollandite structure (Figure 4.1) consists of edge-sharing MnO_6 octahedra, which form 2x2 tunnels with a spacing of the wall atoms of 4.8 Å.^[31] The average oxidation state of the manganese is slightly below +4, caused by a mixed valence.^{[10][17][29][30]}

Considering their inexpensiveness, natural abundance, simple handling and low toxicity, manganese oxides can be seen as candidates with high application potential. Features like stability, the open tunnel structure, the mixed valence of manganese and various ways to synthesize and consequently to adjust material properties make especially Cryptomelane attractive for several applications. Hollandite found attention as electrode material for rechargeable lithium batteries.^[34] Another application of hollandite-type materials is the purification of polluted liquids and gases. On the one hand, it is employed as adsorbent for the selective removal of cations (e.g. K^+).^[32] On the other hand as catalyst for the oxidative degradation of organic chemicals e.g. emitted by manufacturing plants or vehicles.^{[24][35][36][37][38][39][40][41]} A further relevant field in which Cryptomelane might play an important role in future is the electrocatalytic water oxidation, which concerns the issue of chemical energy storage. In this comparative study, the electrocatalytic activity of Cryptomelane was investigated. Therefore, samples with different properties were synthesized by different routes, characterized and compared regarding their performance. Additionally, water oxidation catalysis with Ce^{4+} as chemical oxidizing agent and H_2O_2 decomposition experiments were carried out to evaluate the suitability of Cryptomelane as water oxidation catalyst.

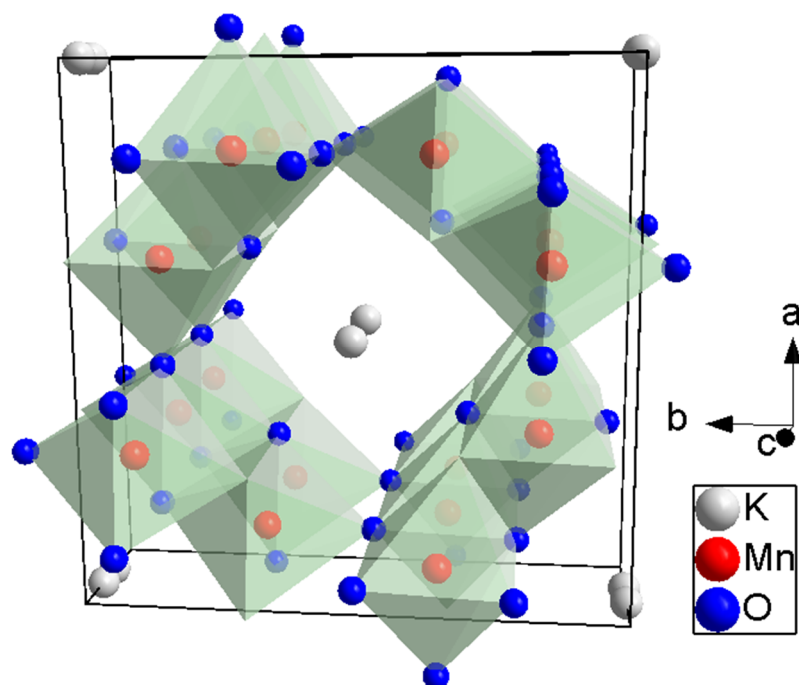


Figure 4.1. Unit cell of Cryptomelane showing the edge-sharing MnO_6 polyhedra that form the tunnels running along the viewing direction (c-axis).

4.3 Experimental Section

4.3.1 Synthesis and sample labelling

R-Cryptomelane

The R-Cryptomelane (R for reflux) synthesis was adapted from DeGuzman et al.^[17] 2.76 g $\text{Mn}(\text{Ac})_2 \cdot 4\text{H}_2\text{O}$ (>99 % p.a., Fluka Chemie AG), 200 ml KMnO_4 (>99 % p.a., Carl Roth GmbH) solution (0.037 mol/l) and 3 ml HNO_3 (65 %, Fisher Chemicals) were stirred (500 rpm) in a 250 ml round-bottom flask connected to a water-cooled condenser opened to the atmosphere at the top. The solution was heated to 100 °C (reflux) for 24 h.

PHT-Cryptomelane

The PHT-Cryptomelane (PHT for precursor hydrothermal) sample was obtained by a two-step synthesis. First, an amorphous precursor was precipitated by combining 300 ml of a 0.15 molar $\text{Mn}(\text{Ac})_2 \cdot 4\text{H}_2\text{O}$ solution and 300 ml of a KMnO_4 solution (0.1 mol/l) in a beaker while stirring (500 rpm) at room temperature for 15 hours. The precipitate was washed with demineralized water until the conductivity of the filtrates fell below $20 \mu\text{S cm}^{-1}$ and dried in static air at 80 °C for 24 h. In a second step the amorphous precursor was suspended in 160 ml H_2O and hydrothermal treated for 48 h at 150 °C in a Teflon-lined autoclave (250 ml).

HT-Cryptomelane

To synthesize HT-Cryptomelane (HT for hydrothermal) analogous to the literature procedure^[73], 2 ml HCl (37 %, VWR Chemicals) was added to 160 ml of a 0.1 molar KMnO_4 solution. After stirring (500 rpm) for 30 min at room temperature the solution was hydrothermal treated for 8 h at 150 °C in a Teflon-lined autoclave (250 ml).

PC-Cryptomelane

For the synthesis of PC-Cryptomelane (PC for precursor calcination) the same amorphous precursor like for PHT-Cryptomelane was used. So, the first step of the route was equal to the one of PHT-Cryptomelane. However, the second step differed. After precipitating, washing and drying, the amorphous precursor was calcined in a muffle furnace for 24 h at 400 °C ($\beta = 20 \text{ K min}^{-1}$) in air.

SS-Cryptomelane

For the synthesis of SS-Cryptomelane (SS for solid state) a solvent-free solid state method developed by Ding et al. was used.^[90] Therefor KMnO_4 and $\text{Mn}(\text{Ac})_2 \cdot 4\text{H}_2\text{O}$ powders were mixed in a stoichiometric ratio of 2:3, ground in a mortar and calcined in a muffle furnace for 4 h at 80 °C ($\beta = 8 \text{ K min}^{-1}$) in air.

All obtained powders were isolated and washed with demineralized water until the conductivity of the filtrates fell below $20 \mu\text{S cm}^{-1}$. Finally, the samples were dried in static air at 80 °C for 24 h.

4.3.2 Characterization

Structural characterization

Powder XRD patterns in the 2θ range from 5 to 90° were recorded with a Bruker D8 Advance diffractometer in Bragg–Brentano geometry by using a position sensitive LYNXEYE detector (Ni-filtered $\text{Cu-K}\alpha$ radiation). A step size of 0.01° and a counting time of 0.3 s were applied. Samples were dispersed with ethanol on a glass disk inserted in a round PMMA holder. The latter was subjected to gentle rotation during scanning. To verify the structure and calculate the lattice parameters a Rietveld refinement was performed using the TOPAS software (Bruker Corporation).^[4]

To examine the catalysts after the electrochemical measurement by XRD the samples were recovered from the glassy carbon electrode with a commercial adhesive tape (Scotch Magic™ Tape, 3M). After applying the catalyst on the adhesive site the prepared tape was fixed on a glass disk in a round PMMA holder and measured by using the above mentioned setup with a step size of 0.01° and a counting time of 2.96 s.

Morphological characterization and BET surface determination

High-resolution SEM images were taken with a JEOL JSM7500F equipped with a cold-field emission gun. An acceleration voltage of 5.0 kV and an emission current of 10 μA were applied. All experiments were performed under high vacuum. Samples were fixed on the metallic holder by using a conductive carbon paste. For determining the BET surface N_2 physisorption experiments were performed at -196 °C with a NOVA 3200e (Quantachrome GmbH & Co. KG) after degassing the samples at 80 °C for 2 h in vacuum. BET surface areas were calculated from p/p_0 data between 0.05 and 0.3.

Thermogravimetric analysis and differential thermal analysis

Thermogravimetric analysis (TG) and differential thermal analysis (DTA) were carried out with a Netzsch STA 449 F3 Jupiter thermoanalyzer. Powdered sample (~ 50 mg) was placed in a corundum crucible and heated from room temperature to 1000 °C. A heating rate of 5 °C min⁻¹ and a mixture of 21 % O₂ in Argon at a flowrate of 100 mL min⁻¹ were applied.

Raman spectroscopy

Raman spectra were recorded with a Jubin–Yvon iHR550 (HORIBA) spectrometer equipped with a 532 nm laser source (Ventus 532, Laser Quantum), using a laser power of 1 mW and a 60x objective.

Operando Raman spectroscopy experiments were conducted in a three electrode cell configuration using a 0.01 M KOH solution as supporting electrolyte. 5 µL of catalyst powder dispersed in a mixture of water and ethanol (1:1) at a concentration of 20 mg mL⁻¹ were drop-cast onto a gold wafer and used as the working electrode. A platinum mesh and an Ag/AgCl (3 M KCl) were used as the counter and the reference electrode, respectively. Cyclic voltammograms were recorded until obtaining a constant response in the range from 0.1 to 0.5 V vs. Ag/AgCl (1.02 to 1.42 V vs. RHE) at a scan rate of 0.1 V s⁻¹. Subsequently, Raman spectra were collected while simultaneously applying potentials in the range from 0.1 to 1.0 V vs. Ag/AgCl (1.02 to 1.92 V vs. RHE).

Atomic absorption spectroscopy (AAS)

The metal content of the as-prepared samples was determined by atomic absorption spectroscopy (Thermo Electron Corporation, M-Series) after dissolving the powders in hydrochloric acid.

Resistance measurement

The resistance was measured by a four-terminal sensing using a Keithley 4200 SCS parameter analyzer combined with a point probe station. The powdered sample were pressed to solid pills with a hydraulic press (Perkin-Elmer, Waltham) by applying a pressure of 5 bar for 2 min. The prepared sample were contacted with four probes arranged in a line. Current was supplied by the outer probes while a voltage in the inner voltage probes were recorded.

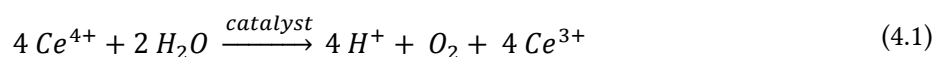
4.3.3 Catalysis

Electrocatalysis

The electrochemical measurements were carried out in a cell with three-electrode setup and a 1 M KOH solution as the electrolyte. An Autolab potentiostat/galvanostat (PGSTAT12, Eco Chemie, Utrecht, The Netherlands) coupled to a Metrohm RDE rotator (1600 rpm) was used. The glassy carbon tip of the working electrode had a geometric area of 0.126 cm². Ag/AgCl/3 M KCl and platinum foil acted as reference electrode and counter electrode. The catalyst ink was prepared by dispersing 2.5 mg of the catalyst in 2 µl nafion, 249 µl ethanol and 249 µl water followed by 15 min ultrasonication. 5.0 µl of the ink was drop coated onto the polished glassy carbon electrode and dried in air at room temperature for about 2 h. The loaded electrodes were subjected to continuous potential cycling until reproducible voltammograms were obtained before catalytic measurements. Electrochemical impedance spectroscopy was then recorded in the frequency range from 50 kHz to 1 Hz at the corresponding open circuit potential of the electrode, using an AC perturbation of 10 mV. The resistance of the solution was determined from the resulting Nyquist plot and used for iR drop correction. All reported current densities were calculated using the geometric surface area of the electrode. The measured potentials were converted to the reversible hydrogen electrode (RHE) scale.^{[78][79]}

Water oxidation catalysis and catalytic H₂O₂ decomposition

Water oxidation catalysis (WOC) was executed with Ce⁴⁺ as chemical oxidizing agent. This well-established method ^{[56][91][92][93]} was recently summarized by Frey et al..^[10] The single-electron oxidant Ce⁴⁺ ($E^0(\text{Ce}^{3+}/\text{Ce}^{4+}) = +1.72 \text{ V vs. NHE at pH}=0$ ^[94]) is reduced to Ce³⁺ during the reaction while water is oxidized to oxygen.



In a typical experiment 100 mg catalyst was dispersed in 45 ml H₂O. The reaction was conducted at pH≈2. While bubbling Argon (50 ml/min) through the dispersion 5 ml of a (NH₄)₂Ce(NO₃)₆ solution (2.5 mol/l) was added. The evolving oxygen was detected by the electrochemical oxygen analyzer EC900 (Systech Illinois).

Catalytic H₂O₂ decomposition experiments were carried out using the same set up by dispersing 200 mg catalyst in 45 ml 4 molar H₂O₂ solution.

4.4 Results and Discussion

4.4.1 Characterization

Structural analysis

Various complementary methods were carried out to characterize and analyse the obtained Cryptomelane samples and to study the effect of the applied synthesis route.

To first verify the success of synthesis, XRD patterns of each sample were recorded. The XRD patterns (Figure 4.2) indicate no other crystalline phases than the hollandite-type structure of Cryptomelane (α -(K)MnO₂). However, slight differences are observable. The patterns of PHT-, HT and PC-Cryptomelane show very discrete and sharp reflections and also the peaks with relatively low intensity are clearly detected. In contrast, the patterns of the R- and SS-Cryptomelane exhibit broad peaks with lower intensity, but still assignable to Cryptomelane. The dissimilar peak widths can be interpreted as varying defect density in the crystal structures

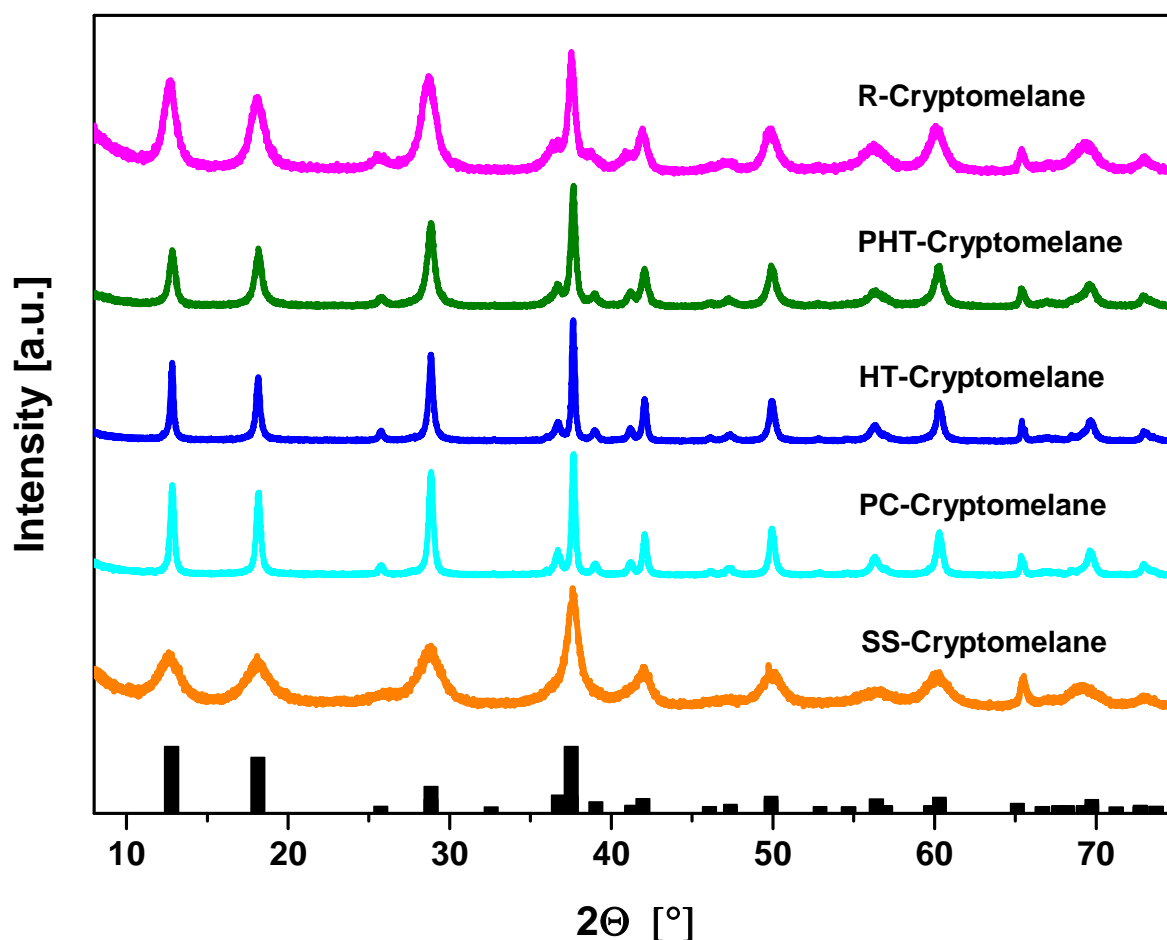


Figure 4.2. XRD patterns of different Cryptomelane samples. Reference pattern: Cryptomelane ^[34].

and are especially influenced by crystallite size and grain boundaries. To verify this assumption and determine further structural properties, a Rietveld refinement of the powder diffraction data of Cryptomelane was performed. All refinements show satisfactorily goodness factors (Table S4.1) and graphical results (Figure 4.3). In Table 4.1, selected structural data and results of the refinements are summarized. To quantify the before-mentioned density of grain boundaries or size effects, the volume-weighted mean column height (LVol-IB) was calculated. This value correlates with the grain size (but not necessarily with the particle size) and thus inversely with the number of grain boundaries and the peak width. In Table 4.1, it is clearly observable that the synthesis method strongly effects the grain size of the product. The LVol-IB value varies almost by an order of magnitude and ranges between 6 and 58 nm. The refinements also reveal slight differences in the lattice parameters of the Cryptomelane samples. The value of the c parameter was calculated to be at approximately 2.85 Å for all samples, whereas the a/b parameter ranges between 9.80 and 9.83 Å, which may indicate a varying widening of the 2x2 tunnels. However, the patterns with broad reflections (R-, and SS-Cryptomelane) exhibit a higher uncertainty of the lattice parameters apparent from the estimated standard deviations (round brackets, Table 4.1) and are thus difficult to interpret properly. The XRD patterns show differences in the relative intensities of some reflections which may be reasoned with a preferably orientation of anisotropic crystallites. Actually the goodness-of-fit of the Rietveld refinement can be further optimized by taking a preferred

Table 4.1. Structural data, lattice parameter and [a] volume-weighted mean column height of different Cryptomelane samples obtained by Rietveld refinement

<i>Phase:</i>	<i>Structure type:</i>	<i>Crystal system:</i>	<i>Space Group:</i>	<i>F. Units/Cell:</i>
Cryptomelane	α -MnO ₂	tetragonal	I 4/m (87)	8
<i>Sample</i>	<i>R-Cryptomelane</i>	<i>PHT-Cryptomelane</i>	<i>HT-Cryptomelane</i>	
<i>Lattice parameter</i> & <i>LVol-IB</i> [a]	a = b = 9.83(8) Å c = 2.85(2) Å $\alpha = \beta = \gamma = 90^\circ$ LVol-IB = 9(6) nm	a = b = 9.819(6) Å c = 2.8554(17) Å $\alpha = \beta = \gamma = 90^\circ$ LVol-IB = 19(5) nm	a = b = 9.8062(19) Å c = 2.8526(5) Å $\alpha = \beta = \gamma = 90^\circ$ LVol-IB = 48(9) nm	
<i>Sample</i>	PC-Cryptomelane		SS-Cryptomelane	
<i>Lattice parameter</i> & <i>LVol-IB</i> [a]	a = b = 9.810(2) Å c = 2.8536(6) Å $\alpha = \beta = \gamma = 90^\circ$ LVol-IB = 58(15) nm		a = b = 9.8(2) Å c = 2.85(6) Å $\alpha = \beta = \gamma = 90^\circ$ LVol-IB = 6(19) nm	

growth along $\langle 001 \rangle$ direction and a consequently preferred orientation of the crystallites with a strong needle-like character (R-, PHT, HT-Cryptomelane) into account. This anisotropy is observed in the SEM images in Figure 4.5.

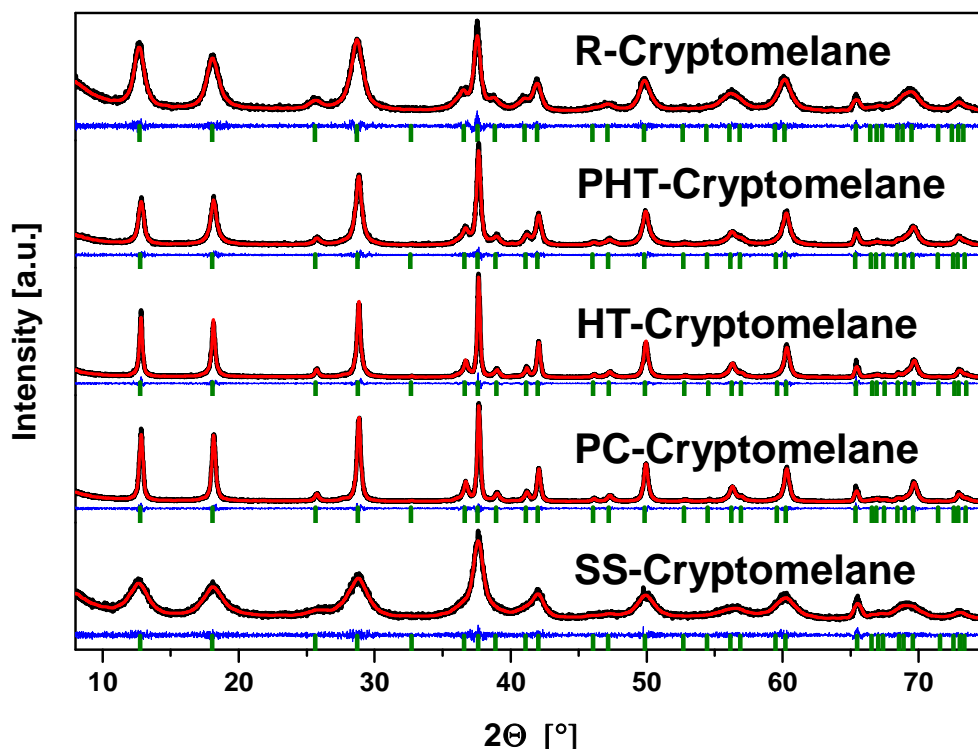


Figure 4.3. Graphical results of the Rietveld refinement of the powder diffraction data of different Cryptomelane samples.

For further structural characterization Raman spectra of R- and HT-Cryptomelane were recorded. The results are shown in Figure 4.4 and Table 4.2. Both samples exhibit Raman peaks previously reported for α -(K)MnO₂.^{[95][96][97]}

The presence of the peaks at ~ 580 and ~ 640 cm⁻¹ indicates a well-defined hollandite-type tetragonal structure, and are caused by symmetric vibrations of the manganese-oxygen bonds^{[95][97]}, while the low intensity bands found between 280 and 520 cm⁻¹ originate from deformation modes.^[96] The intense peak centered at ~ 185 cm⁻¹ differentiates α -MnO₂ from other MnO₂ structures and is due to translational motion of the MnO₆ octahedra.^[96]

The weak peak at 759 cm⁻¹ was found in the case of R-Cryptomelane at very low intensity, but it was not possible to distinguish it in the HT-Cryptomelane sample. It is related to the antisymmetric Mn-O stretching vibrations.^{[95][97]}

Table 4.2. Peaks observed in the Raman spectra.

<i>Cryptomelane sample</i>	<i>Raman wavenumber [cm⁻¹]</i>						
<i>R</i>	182	296	385	511	580	640	759
<i>HT</i>	189	280	385	514	578	639	-
<i>Reference</i> ^[97]	183	330	386	512	574	634	753

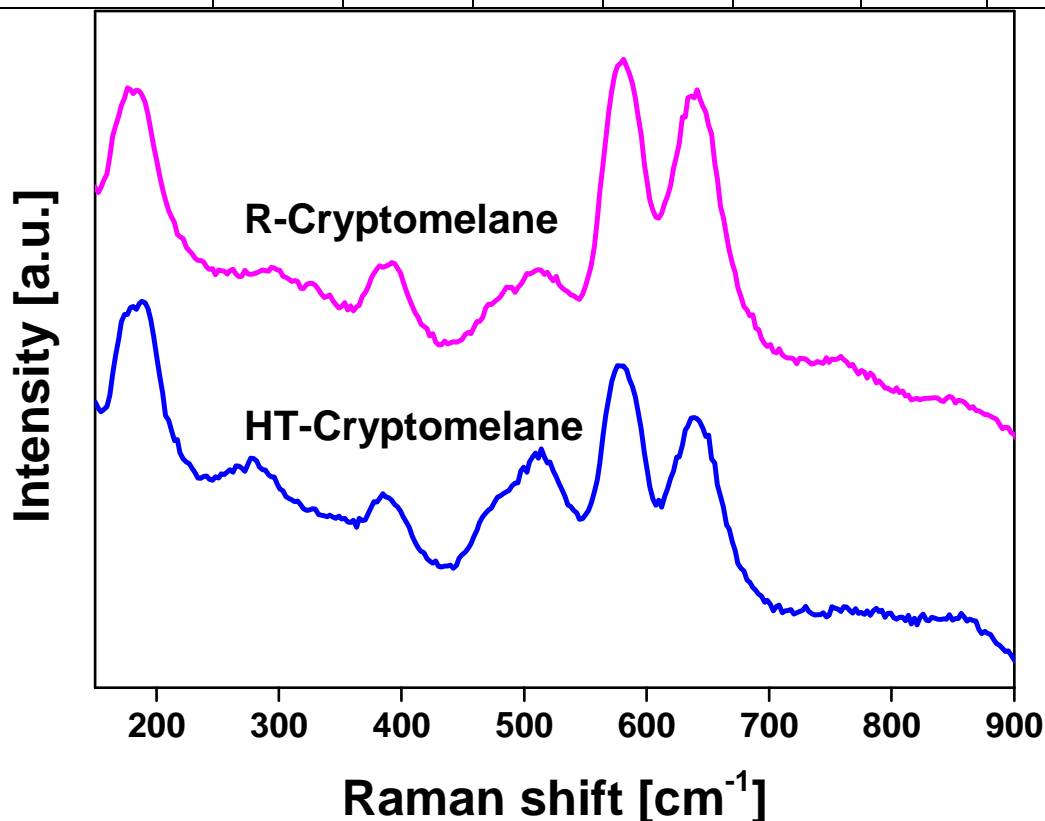


Figure 4.4. Raman spectra of R- and HT-Cryptomelane.

Morphological analysis

The morphology of the R-, PHT- and HT-Cryptomelane can be clearly described as needle-like. The PC- and SS-Cryptomelane give the impression of a sponge-like morphology however in a higher resolution also short intertwined needles can be recognized thus all samples crystallized in form of needles. The preference for this shape is often observed and the needles are reported to be orientated along the 2x2 tunnels ($\langle 001 \rangle$ direction).^[98] To quantify the needle-like character, the average length and width of the particles in the SEM images was measured to gain the average aspect ratio (Table 4.3). In dependence of the chosen synthesis route the particle size varies in a large range. The mean needle lengths range between 40 and 580 nm

and the mean needle widths between 60 and 20 nm leading to a variation of the aspect ratio between 2 and 15. Clearly indicated by the images and verified by high aspect ratios, the needle growth benefits from wet synthesis conditions during the Cryptomelane crystallization step and the lowest values are found for the dry synthesis of PC- and SS-Cryptomelane. The variation of the aspect ratio is mainly impacted by the needle length rather than the width.

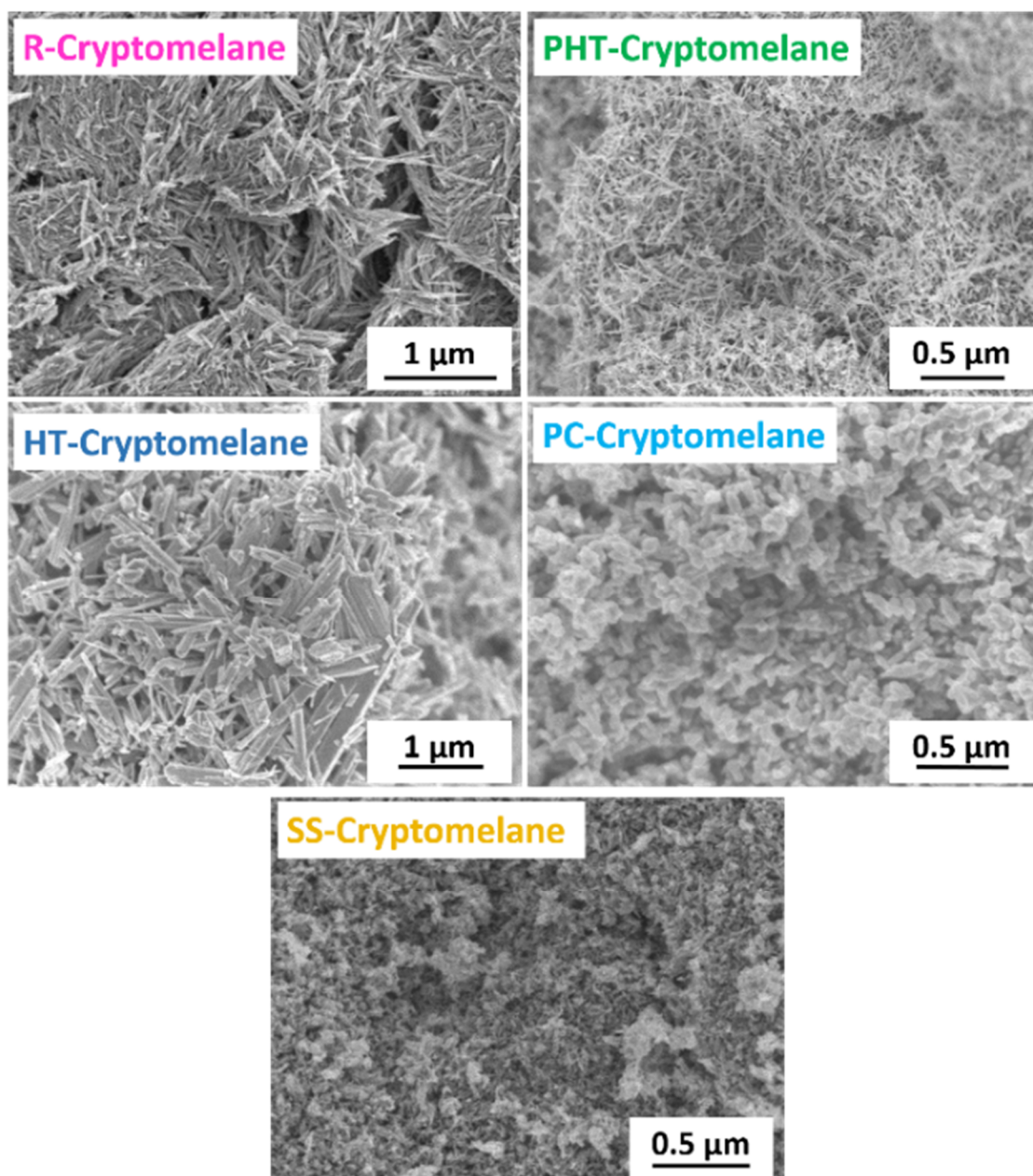


Figure 4.5. Scanning electron micrographs of different Cryptomelane samples.

Table 4.3. Textural and elemental properties of Cryptomelane. [a] BET surface area, [b] average needle length, [c] average needle width, [d] average aspect ratio of needles (length/width), [e] The oxygen content was estimated from the difference to 100 % of the total elemental composition. An average manganese oxidation state of +3.8 was assumed orientated on literature data.^[10]

<i>Cryptomelane sample</i>	S_{BET} [m ² /g] ^[a]	$l_{\emptyset/needle}$ [nm] ^[b]	$W_{\emptyset/needle}$ [nm] ^[c]	\emptyset aspect ratio ^[d]	<i>Chemical formula</i> ^[e]
<i>R</i>	94	580	40	15	K _{0.10} MnO _{1.95} x 0.30 H ₂ O
<i>PHT</i>	45	570	50	11	K _{0.12} MnO _{1.96} x 0.22 H ₂ O
<i>HT</i>	9	420	60	7	K _{0.13} MnO _{1.97} x 0.01 H ₂ O
<i>PC</i>	39	110	40	3	K _{0.13} MnO _{1.97} x 0.14 H ₂ O
<i>SS</i>	166	40	20	2	K _{0.10} MnO _{1.95} x 0.57 H ₂ O

Textural properties and chemical composition

The BET surface areas as well as the chemical compositions of the examined Cryptomelane phases strongly depend on the synthesis route. The respective values are listed in Table 4.3. The surface area, obtained by nitrogen adsorption data and evaluated by the BET method, range between 9 and 170 m²/g. The manganese and potassium content was measured by atomic absorption spectroscopy. The oxygen quantity is estimated from the difference to 100 % of the total elemental composition. The inorganic bound oxygen amount is calculated by assuming an average manganese oxidation state of +3.8^[10] and a potassium oxidation state of +1. The remaining oxygen is attributed to H₂O. The so determined water content correlates with the BET surface area of the samples indicating a high amount of surface bound water. This is backed by a thermogravimetric analysis (Figure 4.7). The surface water related mass loss between 50 and 300 °C follows the same trend like the BET surface area and the calculated water content. Thus, a high surface area leads to a high amount of (re-adsorbed) surface water and consequently to a high mass loss between 50 and 300 °C while heating the sample in air. This correlation is shown graphically in Figure 4.6. The potassium to manganese ratio is only slightly influenced by the synthetic method and similar to previously reported data.^[99]

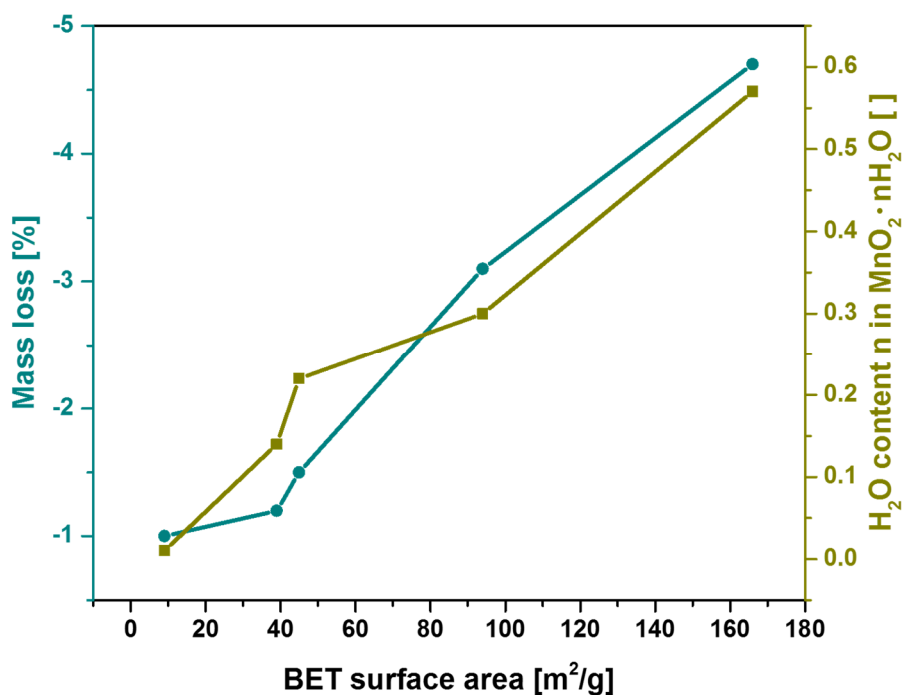


Figure 4.6. Correlation between BET surface area, water content (dark yellow) and water related mass loss while thermal treatment in air between 50 and 300 °C (dark cyan) of Cryptomelane.

Thermogravimetric analysis

The different Cryptomelane samples were characterized by thermogravimetric analysis (TG) followed by subsequent XRD analysis at representative temperatures to identify the obtained phases beyond the initial loss of surface water. As depicted in the TG Graph (Figure 4.7) four major steps occur up to a temperature of 1000 °C. The first mass loss between 50 and 300 °C

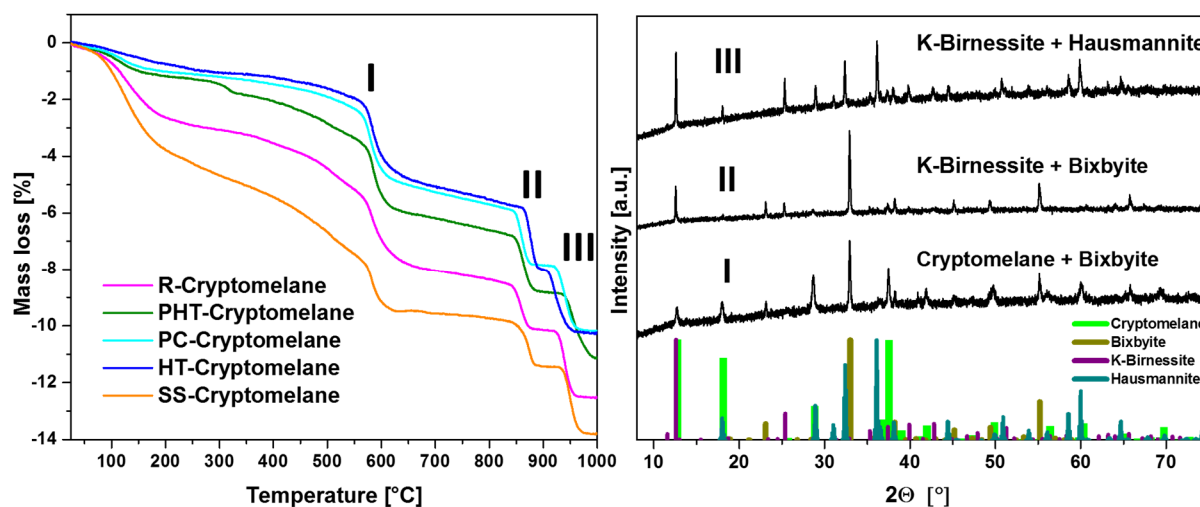


Figure 4.7. Left: thermogravimetric analysis of different Cryptomelane samples. Right: subsequently external XRD analysis of PC-Cryptomelane sample. Reference pattern: green: Cryptomelane^[34], dark yellow: Bixbyite^[113], purple: K-Birnessite^[83], dark cyan: Hausmannite^[67].

can be attributed to the loss of re-adsorbed surface water. The second event at about 550 °C indicates the loss of oxygen and a phase transition from pure Cryptomelane to a mixture of Cryptomelane and Bixbyite ($\alpha\text{-Mn}_2\text{O}_3$). Note that potassium-free Cryptomelane ($\alpha\text{-MnO}_2$) shows at a lower temperature a phase change to pure Bixbyite (Figure S3.4). The persistence of Cryptomelane might thus be explained with the presence of potassium. Dense Bixbyite is unable to incorporate K^+ , thus another potassium rich phase must be present. At about 850 °C a change to K-Birnessite ($\delta\text{-(K)MnO}_2$) and Bixbyite was detected. K-Birnessite exhibits a layered structure and can incorporate a relatively large amount of potassium. It remains stable up to 1000 °C in contrast to the Bixbyite phase which disappears at around 950 °C while a Hausmannite phase evolves. Hausmannite (Mn_3O_4) shows likely the same inability to incorporate potassium like Bixbyite. The observed features are similar to previously reported thermogravimetric analysis.^[99]

4.4.2 Catalysis

Water oxidation catalysis and catalytic H_2O_2 decomposition

In this study, water oxidation catalysis (WOC) was performed with Ce^{4+} as chemical oxidizing agent. WOC was carried out at $\text{pH}\approx 2$ whereas the H_2O_2 decomposition experiments were run at neutral pH. The results of the WOC experiments are graphically presented in Figure 4.8 a. The catalytic activities of the Cryptomelane phases strongly differ. The sample with the lowest value only exhibits an initial O_2 evolution rate of around $1 \mu\text{mol} \cdot \text{min}^{-1}$ whereas the highest rate can be found at about $10 \mu\text{mol} \cdot \text{min}^{-1}$ reached by SS-Cryptomelane. The activities in H_2O_2 decomposition show the same trend, although the differences were smaller (Figure 4.8 b) and the highest rate is just about three times the value of the lowest rate instead of ten times like in water oxidation catalysis with Ce^{4+} . As expected the absolute O_2 evolution rates are clearly higher in the H_2O_2 decomposition reaction compared to the water oxidation. The decomposition of H_2O_2 by homolytic dissociation of the peroxide bond is a relatively simple and fast reaction that can be assumed to be not very demanding with regard to the requirements of the transition metal oxide surface. Thus, a low degree of structure sensitivity can be expected. As seen in Figure 4.9, the activity trend indeed correlates well with the BET surface area. Consequently, it can be assumed that a major part of the differences in oxygen evolution arises from the different surface areas of the samples as expected for a structure insensitive reaction. Interestingly, also the more demanding WOC reaction shows an activity trend that scales with the BET surface area and is indicative of a structure insensitive reaction as shown

in Figure 4.9a. Accordingly, an influence of the average aspect ratio of the needles or the needle length was not observed (Figure 4.9c, d). Based on these observations, we can assume that the WOC reaction over Cryptomelane is intrinsically slower, but similarly independent

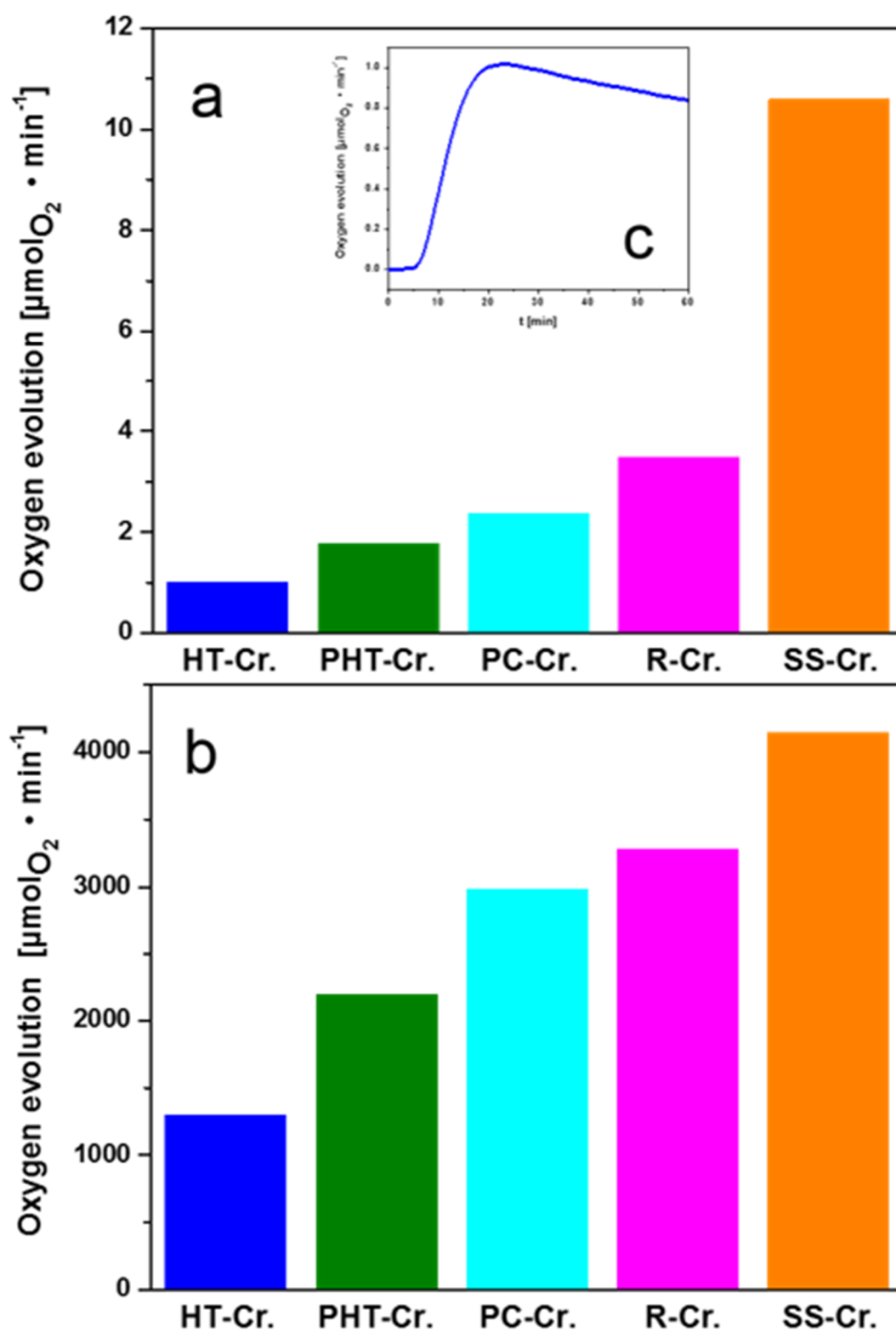


Figure 4.8. Initial rate of oxygen evolution during chemical water oxidation using Ce^{4+} as chemical oxidizing agent (a) and decomposition of hydrogen peroxide (b) catalyzed by different Cryptomelane phases and oxygen evolution rate during chemical water oxidation using Ce^{4+} over a duration of 60 min of HT-Cryptomelane (c).

of the particle morphology as the structure-insensitive H_2O_2 decomposition reaction. All differences in activities are best explained by a higher surface area indicating that sites on different surface facets contribute equally to the WOC. XRD pattern of the HT-Cryptomelane sample were recorded after catalysis. This subsequently measurements followed by Rietveld refinements of the powder data (Figure 4.16, Table 4.4) manifest the structural stability of Cryptomelane at various conditions.

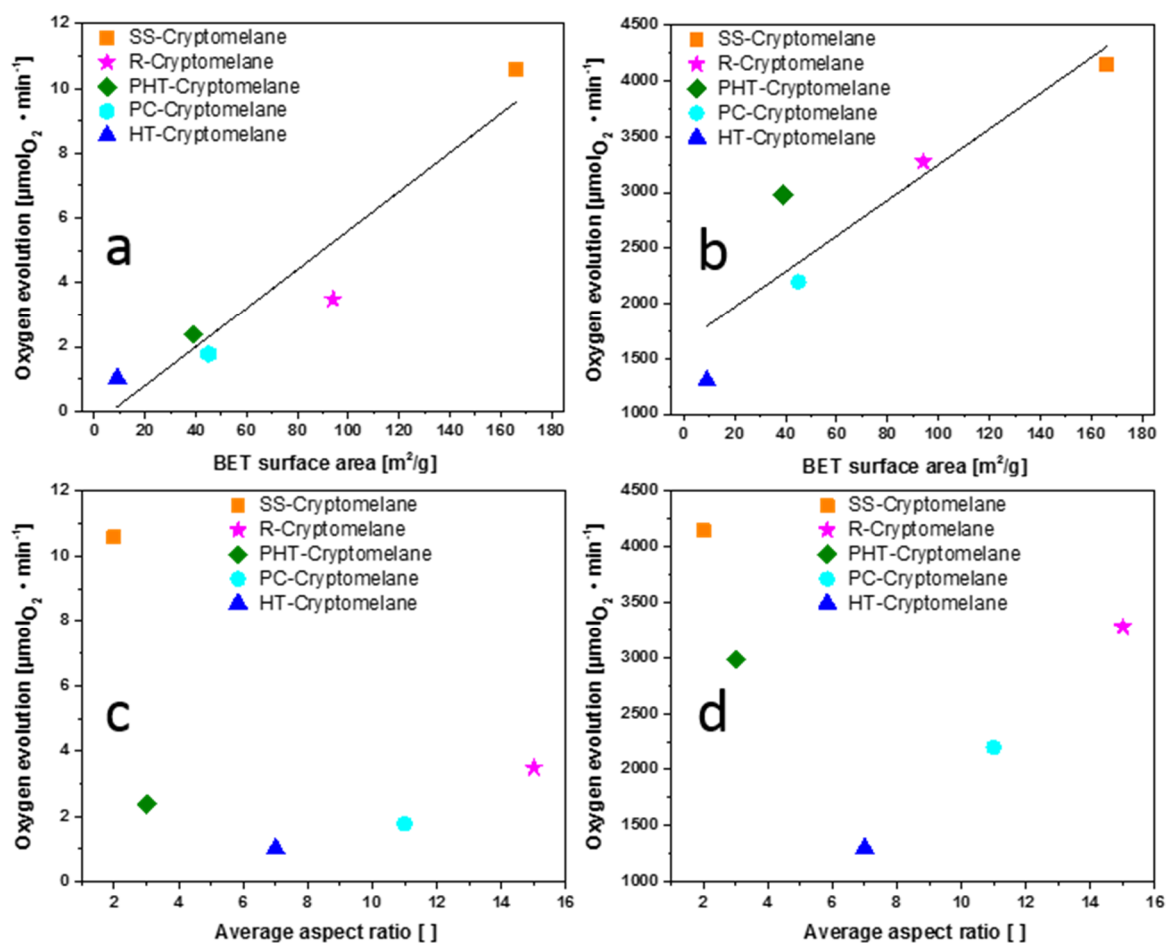


Figure 4.9. Correlation of initial oxygen evolution during chemical water oxidation using Ce^{4+} (a) and during decomposition of hydrogen peroxide (b) with the BET surface area and plot of the initial oxygen evolution during chemical water oxidation using Ce^{4+} (c) and during decomposition of hydrogen peroxide (d) against the average aspect ratio.

Electrocatalysis

The results of the electrocatalytic measurements plotted in Figure 4.10 clearly show strong differences in OER activity of the considered samples. The trend is different from the WOC and the H_2O_2 decomposition experiments and is not correlated with the BET surface area. Thus, the BET surface area is not an important factor for electrocatalytic OER. The most active catalyst (R-Cryptomelane) reaches a current density of about 30 mA/cm^2 at 1.8 V . In contrast to SS-Cryptomelane which just exhibits a value lower than 5 mA/cm^2 . These large differences at 1.8 V can be attributed rather to the slope of the curves and less to the onset, which is around 1.65 V for all samples. R-Cryptomelane is an exception, which starts to catalyze the reaction at about 1.6 V . The varying slopes might be caused by different conductivities of the samples. This is also a likely explanation for the different activity trend if OER is compared to the water oxidation catalysis and the decomposition of hydrogen peroxide. The latter two

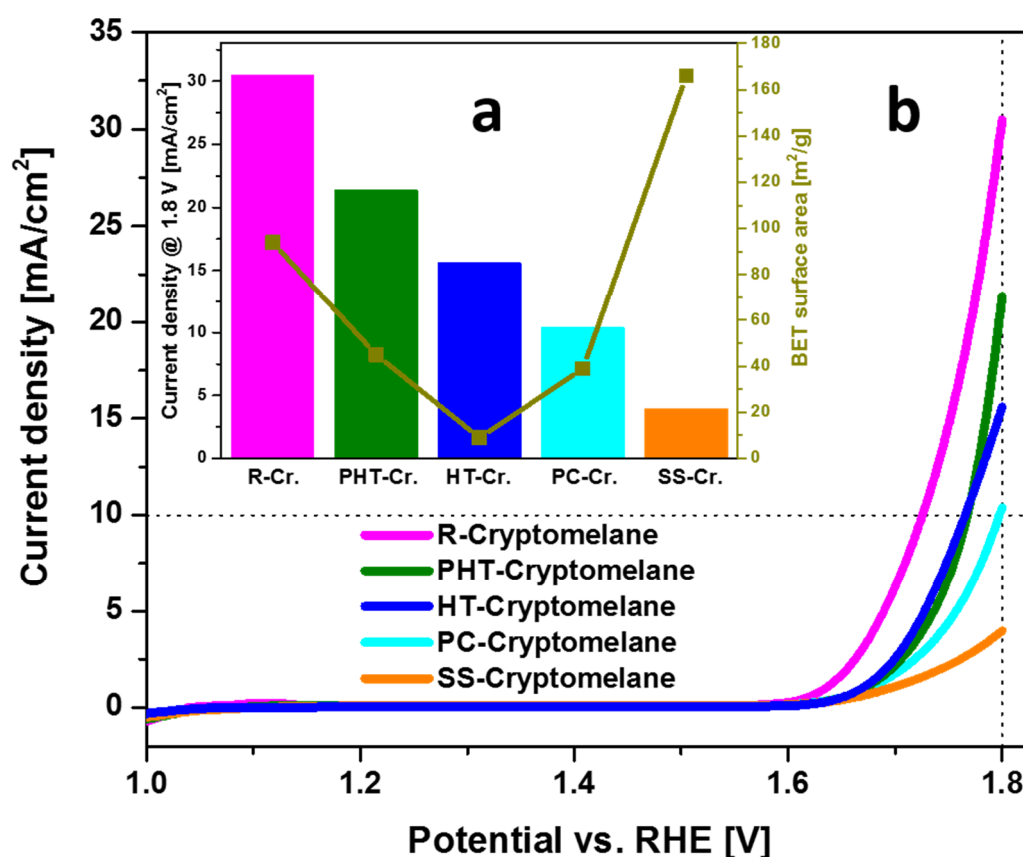


Figure 4.10. OER activities of Cryptomelane phases, a) current density at a voltage of 1.8 V and respective BET surface areas, b) rotating disk electrode voltammograms

reactions are independent of conductivity phenomena unlike the electrocatalytic OER. This assumption was verified by resistance measurements of three samples: R-Cryptomelane as highly active catalyst, HT-Cryptomelane as medium active sample and SS-Cryptomelane as catalyst with the worst performance. The curves in Figure 4.11 a show the voltage difference

at the respective applied current. The slope is according to the ohmic law proportional to the resistance and thus the lower the slope the higher the conductivity. The determined conductivities exhibit the same trend like the OER activities and thus support their impact on the electrocatalytic performance.

An additional influencing factor was found in the morphology of the samples, in particular in the aspect ratio of the needles. The correlation depicted in Figure 4.11 b clearly shows the advantageousness of a high aspect ratio regarding the OER activity suggesting structure sensitivity of the OER at a first sight. Selvakumar et al. investigated the morphological influence

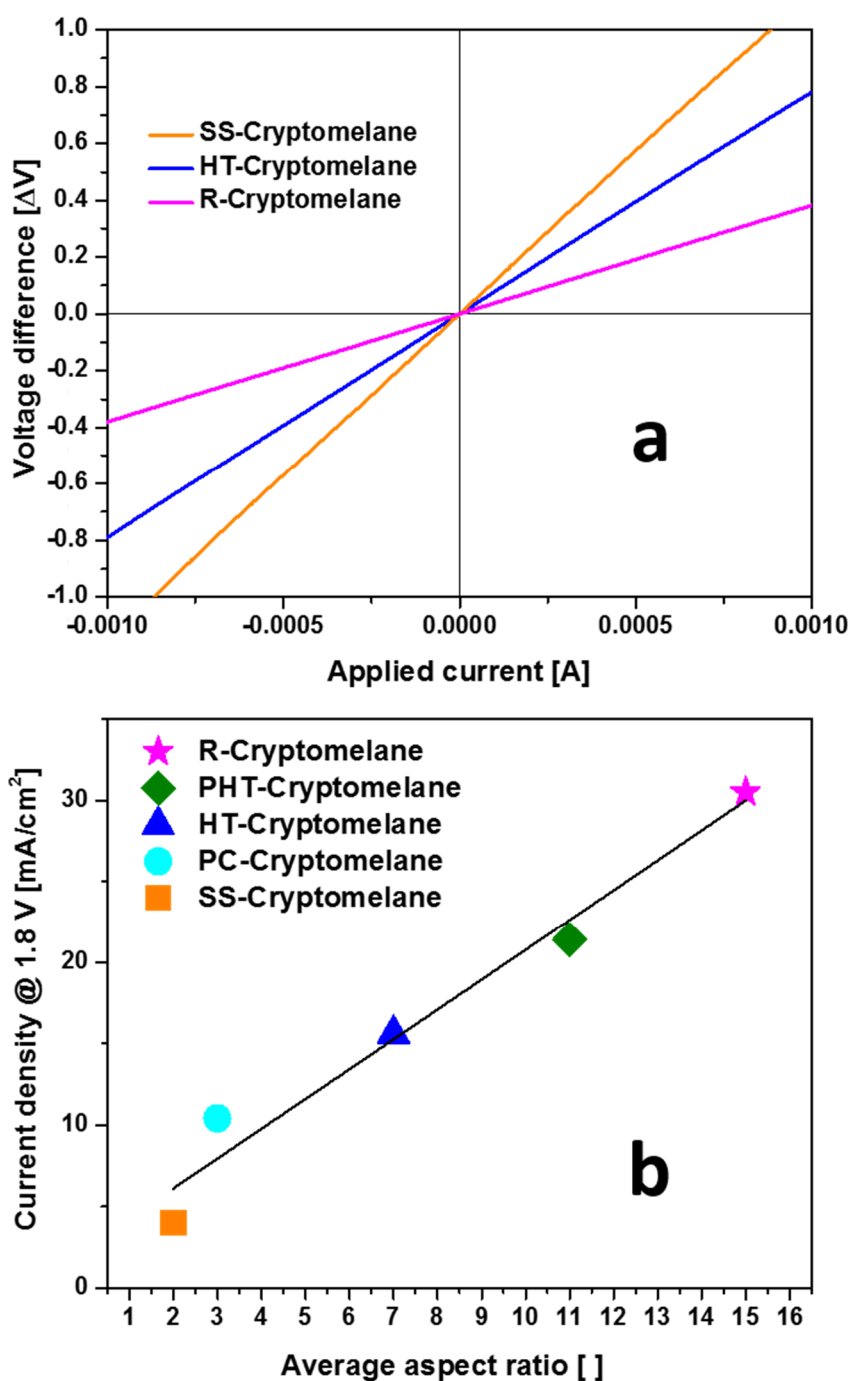


Figure 4.11. a: Resistivity measurement of selected Cryptomelane samples, b: Correlation of activity and mean aspect ratio of different Cryptomelane phases.

of α - MnO_2 samples on the catalytic OER performance with the help of first principles density functional theory.^[100] The group calculated the affinity of (310) crystallographic planes toward water molecules and related it to an enhanced catalytic OER activity. It was assumed that a nano-wire or needle morphology exhibits a higher exposure of these planes to the reaction interface. This result seems to explain our observation, that the OER activity increases parallel to the aspect ratio by means of a structure-sensitive reaction. However, keeping in mind that our WOC data supports the idea that water oxidation proceeds rather in a structure-insensitive manner, though under different pH and with a chemical driving force, an alternative scenario is also possible. In this scenario, the surface sites are present and equally active, but not properly connected to the electrode and a correlation exists between conductivity on the particle level and particle morphology. A possible reason for this correlation may be a facilitated charge-carrier transport through the Cryptomelane needles in the direction of the tunnels than perpendicular to the tunnels. As a consequence, a higher aspect ratio leads to better conductivity and thus better connection of the surface active sites to the electrode

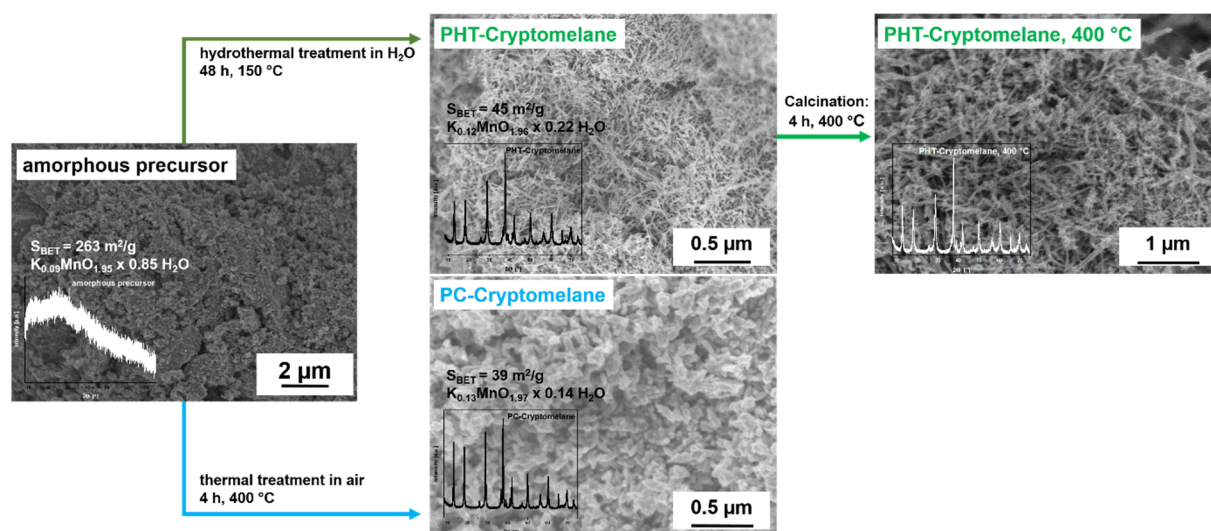


Figure 4.12. Scheme of a post-treated amorphous precursor to obtain Cryptomelane.

leading to an increase in OER activity. The activity enhancement through a more needle-like character is also apparent from the comparison of PHT-, and PC-Cryptomelane. The synthesis is based on precipitating an amorphous precursor followed by a thermal treatment in air (PC-Cry.) or a hydrothermal treatment in H_2O (PHT-Cry.). Major difference is the needle length developed in the final precursor-treatment step in air or in water. The comparative structural and morphological characterization is schematically depicted in Figure 4.12. The synthesis of the amorphous precursor is described in the chapter “Experimental Section”. The precursor exhibits a rough morphology with large aggregated particles. The BET surface area reaches a high value of $263 \text{ m}^2/\text{g}$ indicating a highly porous material. During the post-treatment the

BET surface decreased by about 80 %. To gain comparability, the chemical formula of the amorphous precursor was adapted to the formula of Cryptomelane assuming the same ox-

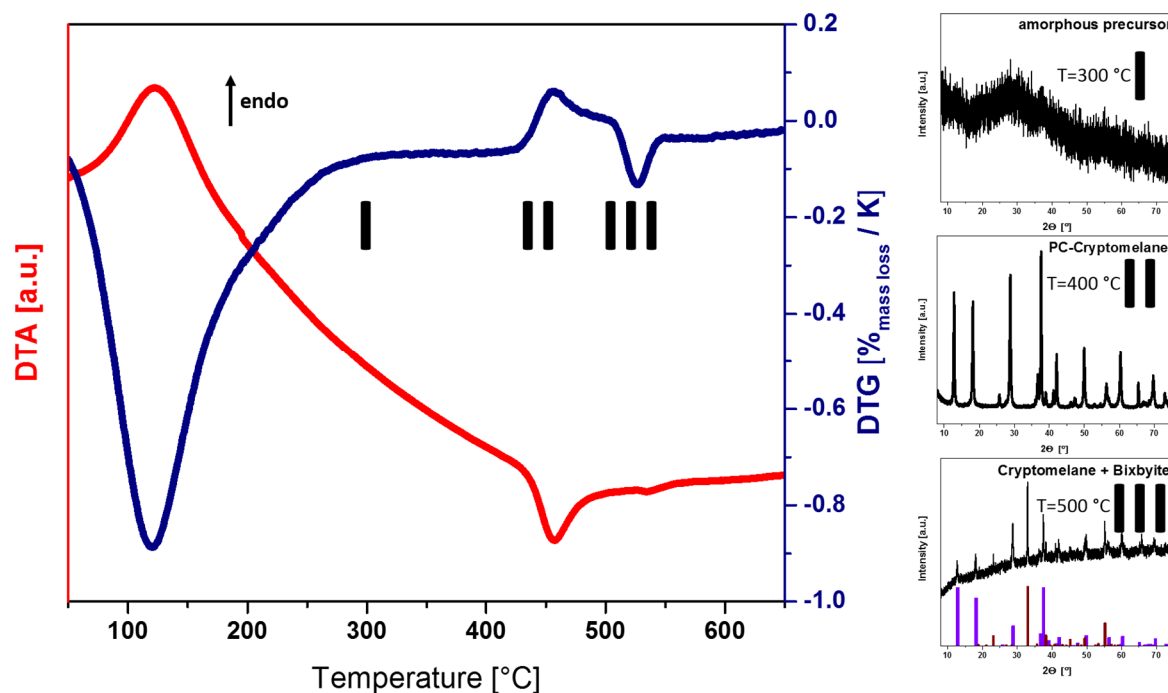


Figure 4.13. Thermogravimetric, differential thermal and subsequent XRD analysis of an amorphous MnO_x precursor to optimize the conditions for PC-Cryptomelane synthesis. Reference pattern: purple: Cryptomelane^[34], dark red: Bixbyite^[113].

dation state of manganese and the binding of remaining oxygen in form of H_2O . Noticeable is the high water content in the precursor, which is also in accordance with the water related mass loss at low temperatures in TG analysis. The chemical composition changes during the post-treatment. The amount of water is strongly lowered, whereas the relative potassium content increases in both products. This points to the preferred incorporation of potassium in the 2×2 tunnels of the Cryptomelane structure. The respective altered potassium to manganese ratio can be explained by the formation of soluble manganese species removed during washing. The conditions of the thermal treatment to obtain PC-Cryptomelane were chosen to be as mild as possible. Thus, the thermogravimetric and differential thermal analysis shown in Figure 4.13 reveal just a small temperature range between 400 and 500 °C as was verified by a subsequent XRD measurement of samples obtained at different temperatures. Higher temperatures lead to a Bixbyite ($\alpha\text{-Mn}_2\text{O}_3$) next to Cryptomelane and lower temperatures don't induce a crystallization.

The higher aspect ratio and the higher OER activity of PHT-Cryptomelane compared to PC-Cryptomelane confirms the advantageousness of a high aspect ratio on the catalytic performance. To rule out surface inactivation processes due to calcination at 400 °C the PHT-Cryptomelane was also treated at 400 °C in air. Surprisingly, this post-treatment even improves

the activity of the PHT-Cryptomelane and pushes the current density to more than 30 mA/cm² at a potential of 1.8 V what is equivalent to three times the value of PC-Cryptomelane. The results are depicted in Figure 4.14 combined with the voltammogram of the amorphous precursor whose low current density suggests a benefit of crystallinity for manganese oxide electrocatalysis. The post-calcination of PHT-Cryptomelane did not substantially affect the aspect ratio. Thus, structure sensitivity is not a good explanation for the improved activity. Instead, it can be assumed that the conductivity of the needles has been further improved by defect annealing during thermal treatment and caused a higher OER performance.

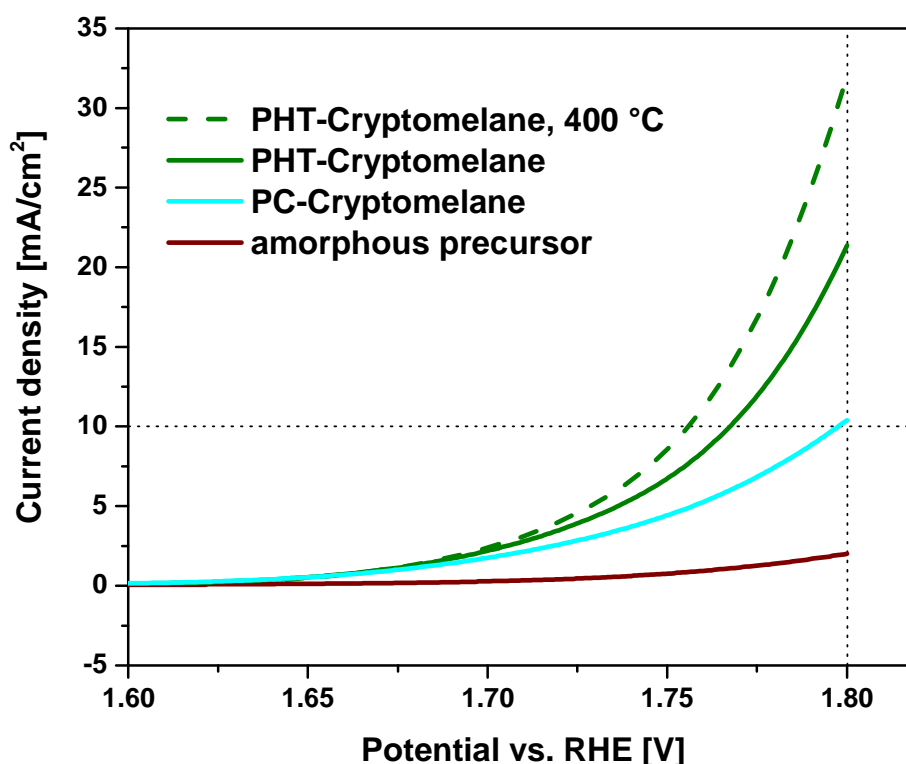


Figure 4.14. OER activities of Cryptomelane phases made of the same amorphous precursor.

Electrocatalytic stability

To evaluate the suitability of Cryptomelane to catalyze the oxygen evolution reaction further knowledge about the stability and behavior during the reaction is necessary. The deactivation of R- and HT-Cryptomelane as high and medium active catalysts were investigated. The potential was fixed at 1.8 V for 60 min while the current was detected. For comparative purposes the degradation process of both samples is normalized as depicted in Figure 4.15. Both catalysts follow the same curve. The strongest activity loss occurs in the first minutes but flattens during the rest of the measurement. After a reaction time of approximately 5 min the detected current flow drops to half of the starting value and fall to zero after 45 min.

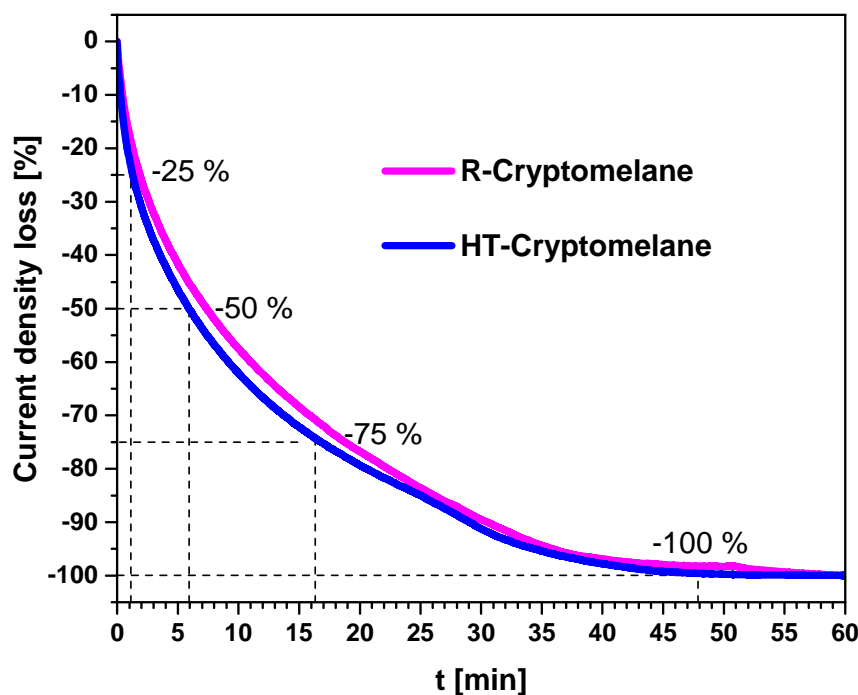


Figure 4.15. Loss of OER activity during stability measurement.

The stability during catalysis was investigated by operando Raman spectroscopy. The Figure 4.16 d shows the Raman spectra of HT-Cryptomelane recorded at different potentials. The main features of the spectra are located in the same position and with similar relative intensities, which suggests that the material is stable under reaction conditions. To examine the catalyst after a measuring time of 10 min a Powder XRD pattern of HT-Cryptomelane was recorded followed by a Rietveld refinement of the data. The result is graphically and tabularly shown in Figure 4.16 a and Table 4.4. The low reflection intensities and the high background

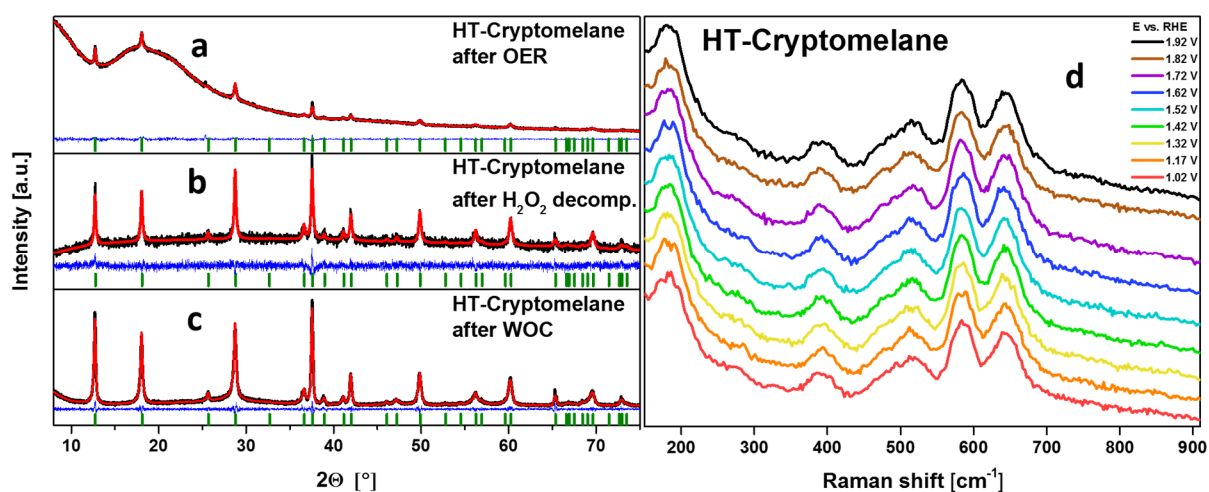


Figure 4.16. Left: Graphical results of the Rietveld refinement of the powder diffraction data of HT-Cryptomelane a) applied on adhesive tape after OER measurement and of HT-Cryptomelane after b) H_2O_2 decomposition and c) Water oxidation catalysis, right: d) Raman spectra of HT-Cryptomelane recorded at different potentials in the range from 1.02 to 1.92 V vs. RHE.

Table 4.4. Lattice parameters of HT-Cryptomelane [a] before catalysis, [b] after OER, [c] after H₂O₂ decomposition and [d] after WOC.

<i>Sample</i>	<i>HT-Cryptomelane</i> ^[a]	<i>HT-Cryptomelane after OER</i> ^[b]
<i>Lattice parameter</i>	a = b = 9.8062(19) Å c = 2.8526(5) Å α = β = γ = 90 °	a = b = 9.835(11) Å c = 2.857(3) Å α = β = γ = 90 °
<i>Sample</i>	<i>HT-Cryptomelane after H₂O₂ dec.</i> ^[c]	<i>HT-Cryptomelane after WOC</i> ^[d]
<i>Lattice parameter</i>	a = b = 9.799(3) Å c = 2.8528(8) Å α = β = γ = 90 °	a = b = 9.807(3) Å c = 2.8522(7) Å α = β = γ = 90 °

are caused by the small amount of catalyst used in electrocatalysis and subsequently for the XRD measurement. The analysis reveals the structural stability of the Cryptomelane catalyst. However, a small increase of the *a/b* parameter was detected indicative of a widening of the tunnels. The loss of activity during water oxidation catalysis using Ce⁴⁺ was significantly lower (Figure 4.8. c) and no noteworthy changes in crystal structure were observed. Consequently, the reason for the degradation during OER may be tentatively related with the widening of the tunnels and caused by the applied potential and the alkaline electrolyte. However, also surface effects may play an important role for the deactivation of Cryptomelane in OER and further investigations are needed to draw reliable conclusions.

4.5 Conclusion

Cryptomelane (α -(K)MnO₂) was successfully synthesized by different methods. XRD pattern were recorded and indicate phase-pure samples crystallizing in hollandite-type structure. Supported by Rietveld refinement of the powder data just slight variations of the lattice parameters and the volume-weighted mean column height can be observed. Raman spectroscopy verifies the presence of pure α -(K)MnO₂. Potassium likely resides in the channels of the α -MnO₂ structure. The potassium content just varies in a small scope from 10 to 13 cation-% in contrast to the BET surface area which ranges between 9 and 166 m²/g. Detected water content is assumed to be mainly surface bound based on thermal gravimetric experiments

which exhibits a related mass loss within the corresponding temperature range. The morphology can be described as needle-like, however the exact shape and the crystallite size strongly depend on the synthesis route and the aspect ratio of the needles varies between 2 and 15. Comparative measurements point out a substantial influence of the synthesis method on the catalytic performance. Water oxidation catalysis with Ce^{4+} as chemical oxidising agent (WOC) and H_2O_2 decomposition experiments were carried out. The oxygen evolution initial rate correlates with the BET surface area for both reactions suggesting a structure insensitive reaction. In contrast, the OER activity seems to be unaffected by the surface area but influenced by the sample conductivity and the morphology. Thus, a high average aspect ratio of the needle-like crystallites and a high conductivity lead to higher electrocatalytic OER activity. Assuming that the water oxidation proceed similarly structure insensitive, a correlation between aspect ratio and conductivity seems likely. This correlation is discussed based on the anisotropy of the crystal structure of Cryptomelane. The most active catalyst reaches about 30 mA/cm^2 at a potential of 1.8 V. To evaluate the stability during the reaction XRD patterns were recorded after WOC, H_2O_2 decomposition and OER. Additionally, operando Raman spectroscopy was carried out during OER catalysis. It can be inferred that Cryptomelane reveals a high structural stability at various conditions. Despite the structural stability long-time OER measurements show a fast decreasing activity of the catalyst during OER. This deactivation was associated with a slight widening of the tunnels in the crystal structure as determined by Rietveld refinement.

4.6 Acknowledgement

The authors acknowledge the Financial support of the BMBF funded project MANGAN (FKZ: 03SF0511B) and the collaboration with the related working groups. The authors also sincerely thank Fatih Özcan for providing the presented SEM images, Manuel Heimann and Stefanie Hoffmann for performing the water oxidation and H_2O_2 decomposition experiments and Laura Kühnel (working group Roland Schmechel, Institute of Technology for Nanostructures, University Duisburg-Essen) for running the resistivity measurements.

4.7 Supporting information

Table S4.1. Results of Rietveld refinement of Cryptomelane

<i>Sample</i>	R_{exp}	R_{wp}	R_p	R_{exp}'	R_{wp}'	R_p'	GOF	R_{Bragg}
<i>R-Cr.</i>	9.25	9.74	7.20	7.75	8.16	6.29	1.05	0.944
<i>PHT-Cr.</i>	11.05	11.42	8.05	9.44	9.75	7.43	1.03	1.169
<i>HT-Cr.</i>	10.43	11.78	8.41	8.12	9.17	7.08	1.13	1.557
<i>PC-Cr.</i>	11.04	11.97	8.02	7.69	8.34	6.04	1.08	1.460
<i>SS-Cr.</i>	9.93	10.34	7.54	7.67	7.99	6.00	1.04	1.154
<i>HT-Crypt. after OER</i>	1.53	1.63	1.16	2.44	2.59	1.99	1.06	0.511
<i>HT-Crypt. after H₂O₂ dec.</i>	2.23	2.38	1.89	6.45	6.89	7.46	1.07	0.624
<i>HT-Crypt. after WOC</i>	7.80	14.25	11.38	1.29	2.36	2.22	1.83	5.263

5. Controlling the Crystallinity of α -MnO₂ Synthesized by Acid Digestion of Bixbyite and its Electrocatalytic OER Activity

Justus Heese-Gärtlein^[a], D. M. Morales^[b], Fatih Özcan^[a], W. Schuhmann^[b], Malte Behrens^{*[a]}

^[a] Faculty of Chemistry, Inorganic Chemistry
University of Duisburg - Essen and Center for Nanointegration Duisburg-Essen
Universitätsstr. 7, 45141 Essen, Germany

^[b] Analytical Chemistry - Center for Electrochemical Sciences Ruhr University Bochum
Universitätsstr. 150, 44780 Bochum, Germany

* Corresponding author (malte.behrens@uni-due.de)

Contributions of co-authors:

D. M. Morales: Measurement and Interpretation of the Raman Spectroscopy experiments.

Fatih Özcan: Measurement of SEM images.

W. Schuhmann: Advising support concerning the Raman Spectroscopy experiments.

M. Behrens: Advising support and editing of the manuscript.

5.1 Abstract

α -MnO₂ powders were prepared by acid digestion of Mn₂O₃ precursor without purifications in its tunnel structure. The influence of the synthesis parameters reaction time, H₂SO₄ concentration, reaction temperature and precursor type is examined in this study. The success of synthesis is defined by the crystallinity of the product which is determined with X-ray diffraction. It can be shown that all four parameters have an impact on the crystallinity of the product. Especially the synthetic prehistory of the precursor is important. To prepare the Mn₂O₃ precursors, different starting materials were used. The reason for the precursor influence is supposed to be its morphology. Electrocatalytic measurements show the suitability of pure α -MnO₂ as catalyst in the oxygen evolution reaction (OER). A fast incorporation of potassium in the crystal structure due to contact with the KOH electrolyte is observed leading to a transformation of α -MnO₂ to Cryptomelane (α -(K)MnO₂) already during OER measurement. The intended insertion of potassium during acid digestion of Bixbyite didn't lead to a more active catalyst, whereas a Cryptomelane sample obtained by a hydrothermal route shows the highest activity of the examined samples. The presence of potassium leads to variations of the lattice parameters and consequences for the electrocatalytic measurement are discussed.

5.2 Introduction

In recent years, manganese oxides with tunnel structures got attention caused by their numerous application possibilities.^{[17][23][24][101]} Especially hollandite-type materials are known for their potential as catalyst or as electrode material for rechargeable lithium batteries and are thus well investigated.^{[90][34][31]} The Hollandite structure consists of edge-sharing MnO₆ octahedra which form 2x2 tunnels with a spacing of the wall atoms of 4.8 Å and are able to incorporate cations.^[32] The K⁺ containing form of Hollandite is called Cryptomelane. Common routes to synthesize Cryptomelane are based on potassium permanganate as reactant.^{[17][90]} To insert other cations than K⁺, it is possible to make a topotactical ion-exchange reaction of Cryptomelane. Tsuji et al. reported a removal of K⁺ with concentrated HNO₃ by a column technique, followed by a treatment with a solution containing different metal ions.^{[32][102]} Feng et al. developed a potassium free method to obtain NH₄⁺-Hollandite. The

group treated a layered manganese oxide hydrothermally with NH_4^+ as template ion.^[103] Another method to generate foreign cation free Hollandite (α -MnO₂) was already established in 1956 from Brenet et al. who synthesized α -MnO₂ by the treatment of Mn₂O₃ with sulfuric acid.^[104] Based on this method Ohzuku et al. prepared in a one-pot process K⁺-, NH₄⁺- and Rb⁺-Hollandite by doing the acid treatment of Mn₂O₃ together with K⁺-, NH₄⁺- or Rb⁺-sul-

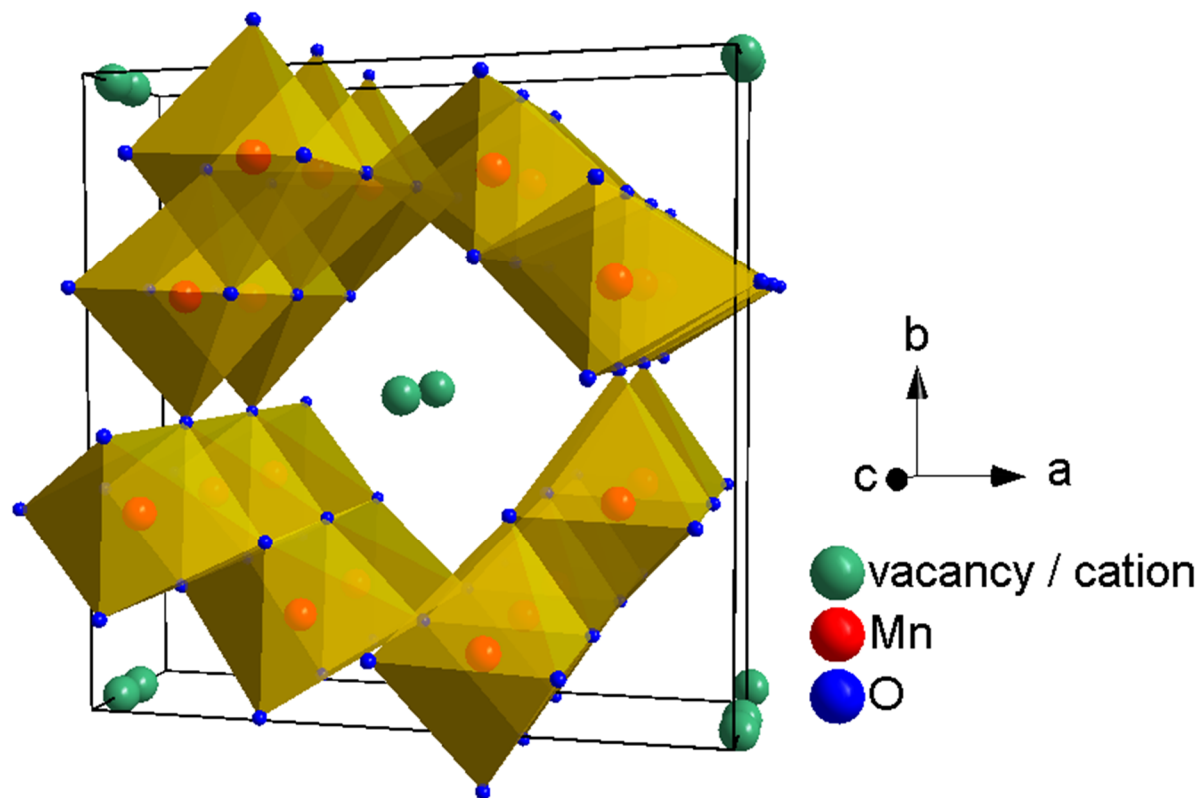


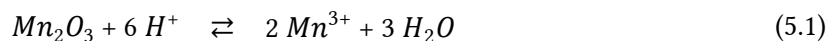
Figure 5.1. Unit cell of α -MnO₂ showing the edge-sharing MnO₆ polyhedra that form the tunnels running along the viewing direction (c-axis).

fate.^[72] Similarly, Zhang et al. used the acid digestion of Mn₂O₃ to influence the potassium content in Cryptomelane through variation of the potassium sulfate concentration in the acidic solution.^[87]

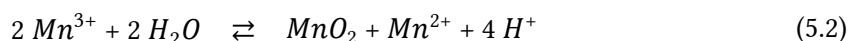
In addition to the flexible type of the tunnel cations, also their amount in hollandite-type materials can strongly vary and decrease even to zero. At present, α -MnO₂ is the only known tunneled manganese oxide which exhibits a stable structure even in the absence of a large stabilizing foreign cation in its tunnels. This point makes α -MnO₂ to an interesting candidate as electrode for secondary lithium cells.^[34] In 1991, Rossouw et al. synthesized a foreign metal ion free Hollandite by Li₂MnO₃ digestion in H₂SO₄ solution. However also the before-mentioned treatment of Mn₂O₃ with sulfuric acid without any additional salt leads to α -MnO₂. Walanda et al. investigated this route especially with regard to the formation of

γ -MnO₂.^{[105][106][107]} The group carried out kinetic and mechanistic studies and proposed a two-step mechanism. The first step of the digestion of Mn₂O₃ with sulfuric acid leads to a dissolved intermediate Mn(III) species followed by a disproportionation of Mn³⁺ to Mn²⁺ and Mn⁴⁺. The Mn(II) species remains in solution while Mn⁴⁺ precipitate as γ -MnO₂.

1.) Dissolution:



2.) Disproportionation-precipitation:



Depending of the digestion parameters temperature and acid concentration different MnO₂ polymorphs (α -, β - and γ -MnO₂) can be obtained as product.^{[107][108]} At present, there are only few investigations if the before mentioned mechanism can be applied on α -MnO₂.^[98] However based on the similarity of the synthetic route this assumption appears reasonable.

The required parameter windows for controlling the synthesis towards the desired MnO₂ polymorph are extensively described in the literature,^{[87][108]} whereas the fine tuning of the relevant synthesis variables within the windows for a well crystallized and given MnO₂ phase is often less regarded. Such synthesis optimization, however, is indispensable for a robust and reproducible manufacture of a well understood product as required for application research. In this work, the influencing factors of the α -MnO₂ synthesis by an acid digestion were examined in detail. The main factors reaction time, H₂SO₄ concentration, reaction temperature and precursor type were evaluated with respect to the synthesis success, which was defined by a high crystallinity of the product. Like mentioned before, hollandite-type materials are known for their high potential in catalysis. In particular potassium containing Hollandite called Cryptomelane is an inexpensive and interesting electrocatalyst for the oxygen evolution reaction (OER).^[86] In contrast to Cryptomelane, potassium free Hollandite (α -MnO₂) attracted less attention in view of its suitability as electrocatalyst. Thus, the roles of the crystallinity and K⁺ content of α -MnO₂ for its catalytic OER performance were also investigated in this study.

5.3 Experimental Section

5.3.1 Synthesis

Manganese(III) oxide (Bixbyite) was synthesized by calcination of manganese based materials in a muffle furnace for 24 h at 800 °C ($\beta = 32 \text{ K min}^{-1}$). Three different starting materials were used: Manganese(III) acetate (97 % p.a., Sigma-Aldrich), Manganese(IV) oxide (99,995 % p.a., Carl Roth GmbH), Manganese(III) oxide (99 %, abcr GmbH). The resulted Mn₂O₃ powders were thermally treated with a sulfuric acid solution (H₂SO₄: >95 %, Thermo Fisher Scientific, demineralized water: conductivity < 5 μS) in a reflux apparatus. Therefore 0.3 g of Manganese(III) oxide and 113 ml H₂SO₄ solution were stirred (500 rpm) in a 250 ml round-bottom flask (yield = 85 - 91 %). The Mn₂O₃ precursor made of Manganese(III) acetate was treated with varying parameters: reaction time (3 - 65 h), reaction temperature (70 °C - 110 °C) and the concentration of sulfuric acid (3 - 5 M). In each synthesis just one parameter was varied and the other two were fixed at $t = 24 \text{ h}$ and/or $T = 80 \text{ °C}$ and/or $[\text{H}_2\text{SO}_4] = 4 \text{ mol/l}$. The Mn₂O₃ precursors synthesized by calcination of Manganese(IV) oxide and Manganese(III) oxide were treated with the before mentioned fixed parameters. The obtained black α -MnO₂ powders were isolated and washed with demineralized water until the conductivity of the filtrates fell below 20 $\mu\text{S cm}^{-1}$. Finally, the samples were dried in static air at 80 °C for 24 h. For comparative purposes two potassium containing α -MnO₂ phases were synthesized by different methods. One, called α -(K)MnO₂, via the same route like pure α -MnO₂. Therefore Mn₂O₃ (made of Mn(CH₃COO)₃) and K₂SO₄ (99 % p.a., Carl Roth GmbH) were added in the molar ratio 1:1 to the 4 M sulfuric acid solution and treated for 24 h at 80 °C. The other K⁺ containing α -MnO₂ phase (HT-Cryptomelane) was synthesized similar to the literature procedure of Xu et al.^[109] Here, 2 ml HCl (37 %, VWR Chemicals) was added to 160 ml of a 0.1 molar KMnO₄ solution. After stirring (500 rpm) for 30 min at room temperature the solution was hydrothermal treated for 8 h at 150 °C in a Teflon-lined autoclave (200 ml).

5.3.2 Characterization

BET surface determination and elemental analysis

N₂ physisorption experiments were performed at -196 °C with a NOVA 3200e (Quantachrome GmbH & Co. KG) after degassing the samples at 80 °C for 2 h in vacuum. BET surface areas

were calculated from p/p_0 data between 0.05 and 0.3. The metal content of the as-prepared samples was determined by atomic absorption spectroscopy (Thermo Electron Corporation, M-Series after dissolving the powders in hydrochloric acid.

Structural characterization

Powder XRD patterns in the 2θ range from 5 to 90° were recorded with a Bruker D8 Advance diffractometer in Bragg–Brentano geometry by using a position sensitive LYNXEYE detector (Ni-filtered Cu-K α radiation). A step size of 0.01° and a counting time of 0.3 s were applied. Samples were finally dispersed with ethanol on a glass disk inserted in a round PMMA holder. The latter was subjected to gentle rotation during scanning. To verify the structure and calculate the lattice parameters a Rietveld refinement was performed using the TOPAS software (Bruker Corporation).^[4]

For an examination of the catalysts after the electrochemical measurement, the samples were recovered from the glassy carbon electrode with a commercial adhesive tape (Scotch Magic™ Tape, Minnesota Mining and Manufacturing Company). After applying the catalyst on the adhesive site the prepared tape was fixed on a glass disk in a round PMMA holder and measured by using the above mentioned setup with a step size of 0.01° and a counting time of 2.96 s.

Morphological characterization

High-resolution SEM images were taken with a JEOL JSM7500F equipped with a cold-field emission gun. An acceleration voltage of 5.0 kV and an emission current of 10 μ A were applied. All experiments were performed under high vacuum. Samples were fixed on the metallic holder by using a conductive carbon paste.

Raman spectroscopy

Raman spectra were recorded with a Jubin–Yvon iHR550 (HORIBA) spectrometer equipped with a 532 nm laser source (Ventus 532, Laser Quantum), using a laser power of 1 mW and a 60x objective. In situ Raman spectroscopy experiments were conducted in 0.01 M KOH solution.

Determination of Peak-to-background ratio

The success of synthesis was defined in this work by the crystallinity of the samples. The differences in crystallinity were quantified by a peak-to-background ratio (PBR). Therefore,

the area of the 9 main powder XRD peaks in the 2θ range from 10 to 61° was divided by the complete area of the diagram in the same range. This ratio is proportional to the degree of crystallinity and include all factors influencing the measurement (e.g. instrument parameters, human factor). The determination of the PB-ratio is exemplarily shown for an α -MnO₂ sample in Figure 5.2.

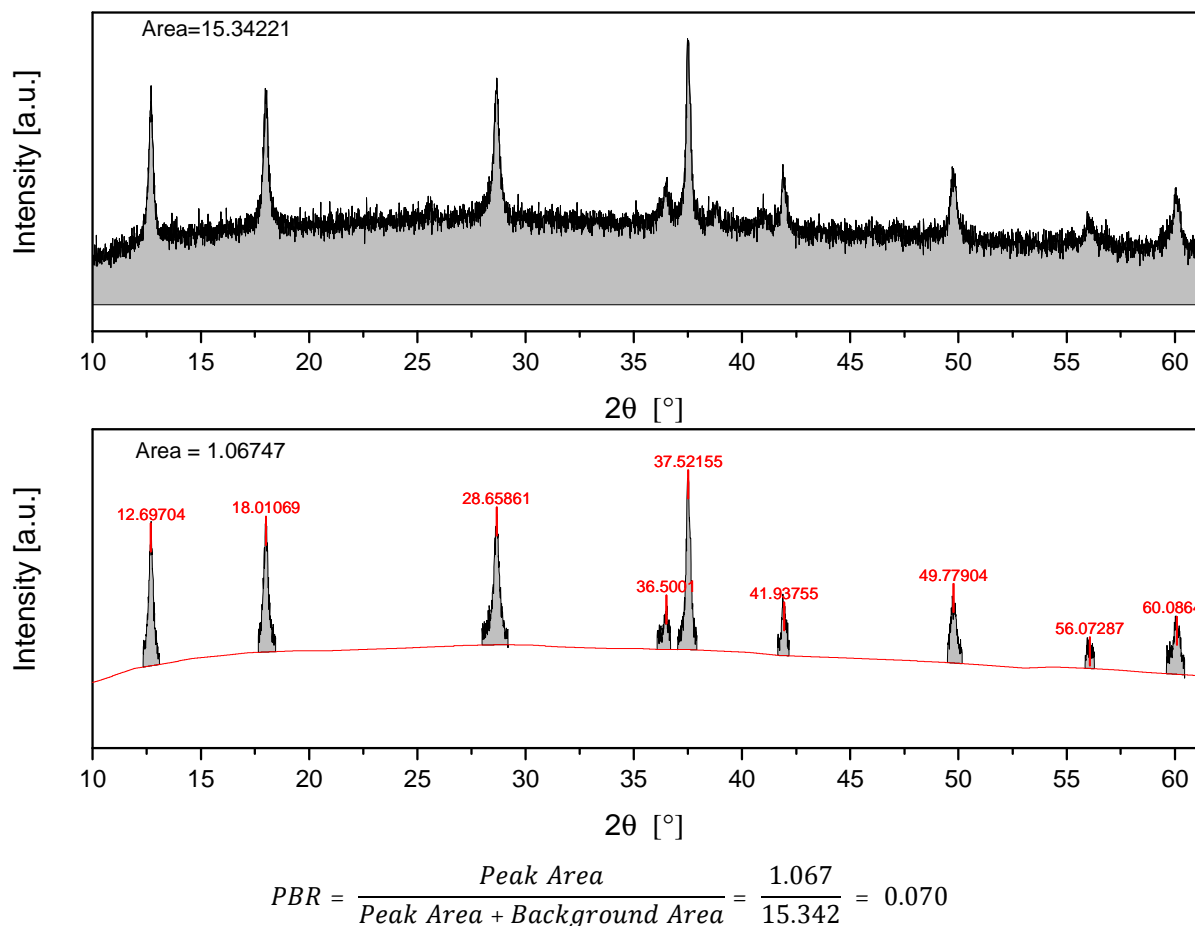


Figure 5.2. Determination and calculation of peak-to-background ratio.

5.3.3 Electrocatalysis

The electrochemical measurements were carried out in a cell with three-electrode setup and a 1 M KOH solution as the electrolyte. An Autolab potentiostat/galvanostat (PGSTAT12, Eco Chemie, Utrecht, The Netherlands) coupled to a Metrohm RDE rotator (1600 rpm) was used. The glassy carbon tip of the working electrode had a geometric area of 0.126 cm². As reference electrode and counter electrode acted Ag/AgCl/3M KCl and platinum foil. The catalyst ink was prepared by dispersing 2.5 mg of the catalyst in 2 μ l nafion, 249 μ l ethanol and 249 μ l water followed by 15 min ultrasonication. 5.0 μ l of the ink was drop coated onto the polished

glassy carbon electrode and dried in air at room temperature for about 2 h. The modified electrodes were subjected to continuous potential cycling until reproducible voltammograms were obtained before catalytic measurements. Electrochemical impedance spectroscopy was then recorded in the frequency range from 50 kHz to 1 Hz at the corresponding open circuit potential of the electrode, using an AC perturbation of 10 mV. The resistance of the solution was determined from the resulting Nyquist plot and used for iR drop correction. All reported current densities were calculated using the geometric surface area of the electrode. The measured potentials were converted to the reversible hydrogen electrode (RHE) scale.^{[78][79]}

5.4 Results and Discussion

5.4.1 Synthesis and Characterisation

The acid digestion of the Bixbyite precursor within the chosen parameter window leads to α -MnO₂ phases, as has been verified by X-ray diffraction. The corresponding XRD patterns are shown in Figure 5.3. The absence of foreign metal cations was proved by atomic absorption spectroscopy. The degree of crystallinity, which is indicated by the peak profiles and the shaping of the background, strongly depends on the exact synthesis parameters. For the evaluation of this effect, crystallinity was expressed with the peak-to-background ratio (PBR) as explained above. The PBR of the respective products is plotted in Figure 5.4 and clearly shows that the varied parameters influence the crystallinity to different extents. The highest impact can be attributed to the concentration of sulfuric acid. Slight deviations from the best value found in this study of 4 M H₂SO₄ disturb the crystallization of α -MnO₂ and lead to a product with a low long-range order. A treatment with a concentration less than 3 M H₂SO₄ results in an amorphous product whereas a treatment with more than 6 M H₂SO₄ prevents the precipitation. A short reaction time of 3 h leads to an α -MnO₂ phase with small PBR, thus a longer time of almost 24 h is required for highly crystalline products. No further improvement of crystallinity is observed, if the reaction time exceeds 24 h. Even a reaction time of 65 h still results in a highly crystalline α -MnO₂ phase showing the high stability of the crystalline product under the chosen conditions. Similar to the reaction time a low temperature of 70 °C leads to an only moderate synthesis success, whereas a temperature range of 80 °C-110 °C results in a product with high PBR. In conclusion, it was shown that the optimal synthesis

parameters to obtain a highly crystalline product are a reaction temperature of 80 °C, a reaction time of 24 h and a concentration of sulfuric acid of 4 mol l⁻¹.

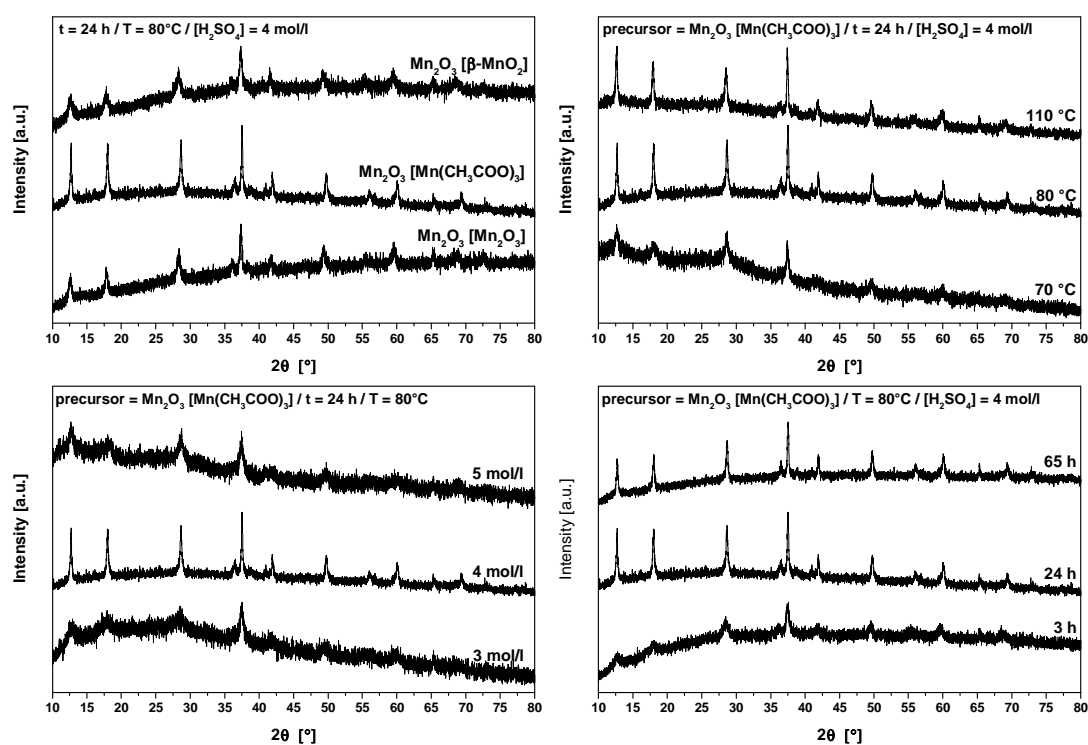


Figure 5.3. XRD patterns of α -MnO₂ synthesized by acid digestion of Mn₂O₃ with varying parameters.

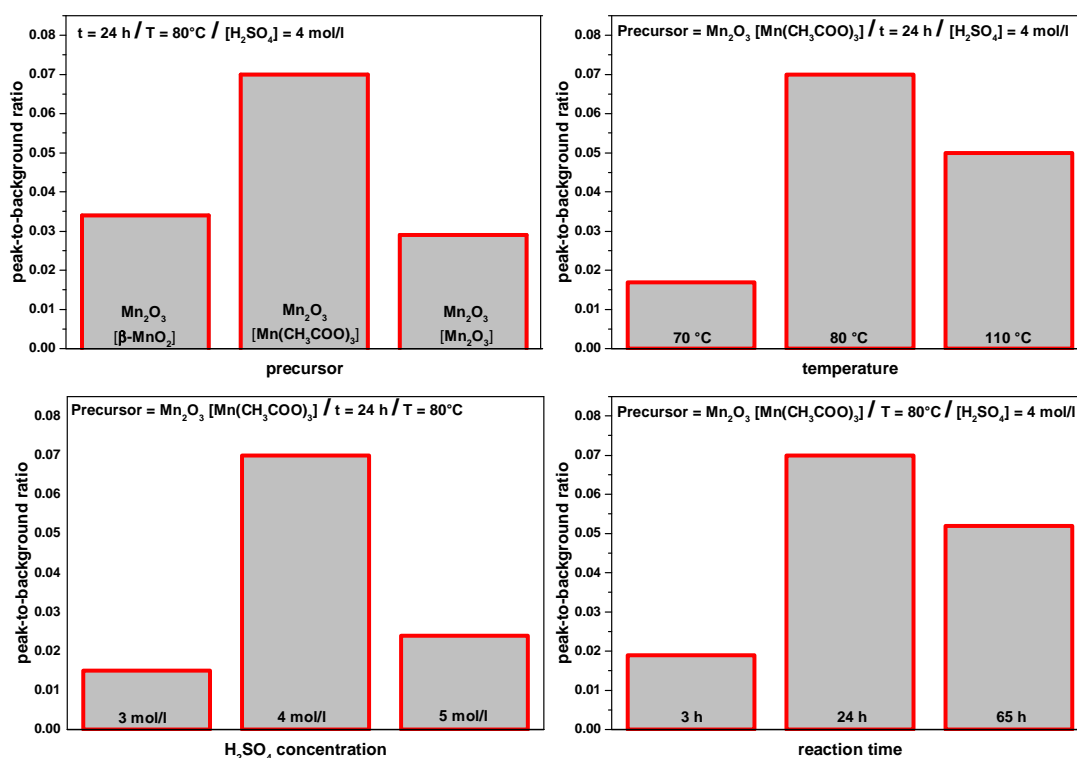


Figure 5.4. Peak-to-background ratio of α -MnO₂ phases synthesized by acid digestion of Mn₂O₃ with varying parameters.

Role of precursor

The fourth investigated parameter is the preparation history of the Bixbyite precursor, Mn₂O₃. The choice of the Mn₂O₃ precursor has not been addressed explicitly in previous literature, but our results show that the starting material strongly affects the degree of crystallinity of the obtained α -MnO₂ products. The samples are labeled in the form (product [precursor]). Surprisingly, the Bixbyite precursor (Mn₂O₃ [Mn₂O₃]) obtained by calcination of commercial Mn₂O₃ leads to foreign cation free Hollandite (α -MnO₂ [Mn₂O₃-derived Mn₂O₃]) with a peak-to-background ratio of 0.029 which is the lowest value within the samples derived from different starting materials. The treatment of the Bixbyite precursor (Mn₂O₃ [β -MnO₂]) made of commercial β -MnO₂ also leads to α -MnO₂ (α -MnO₂ [β -MnO₂-derived Mn₂O₃]) with a relatively low PB-ratio of 0.034. The best result could be obtained by using commercial Manganese(III) acetate (Mn(CH₃COO)₃) for preparing the Mn₂O₃ precursor (Mn₂O₃ [Mn(CH₃COO)₃]) which was transformed into highly crystalline α -MnO₂ (α -MnO₂ [Mn(CH₃COO)₃-derived Mn₂O₃]) with a PB-ratio of 0.07.

The XRD patterns and their Rietveld refinement results show no major differences of the bulk crystal structure between the three Mn₂O₃ precursors derived from commercial Mn₂O₃,

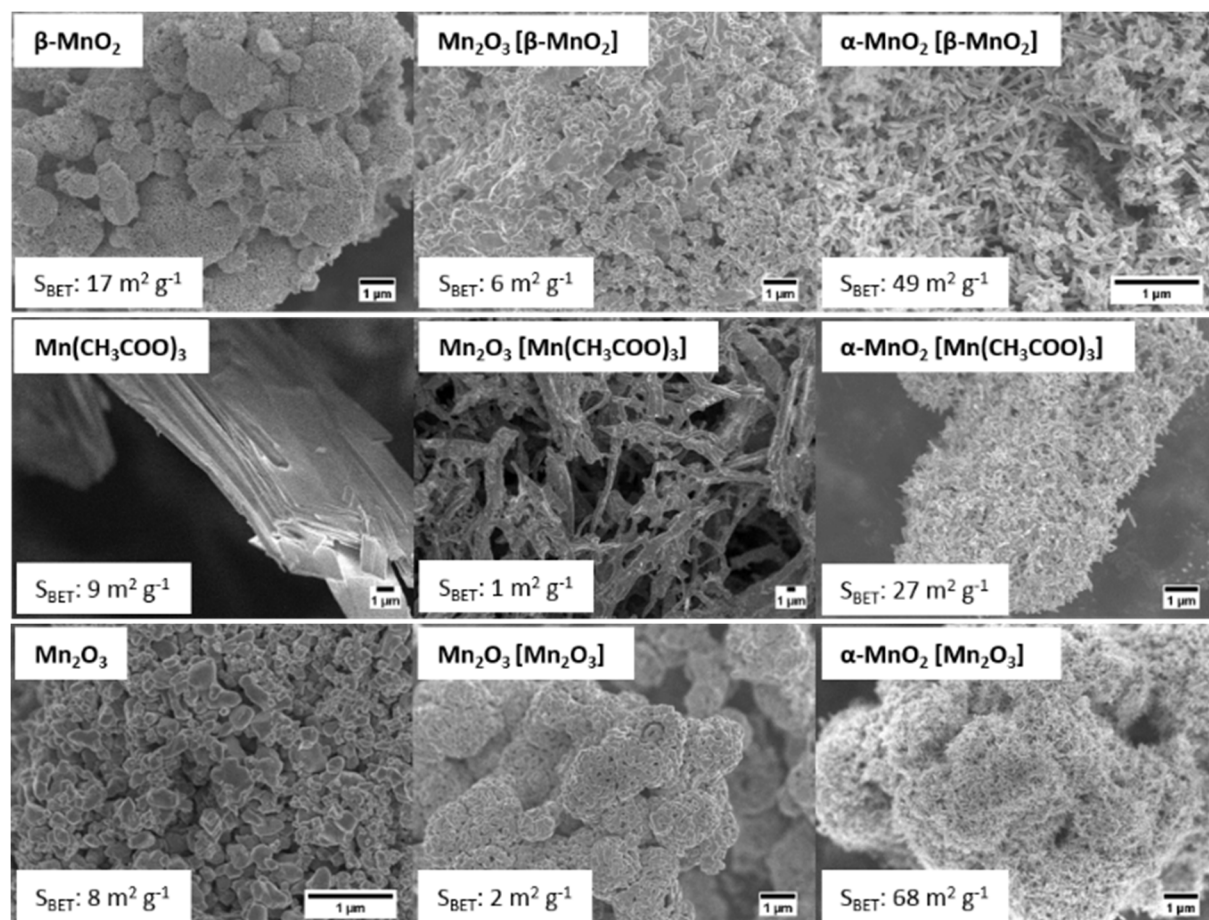


Figure 5.5. Scanning electron micrographs and BET surface areas of the starting material, the calcined starting material (Mn₂O₃) and the product (α -MnO₂).

β -MnO₂ and Mn(CH₃COO)₃, respectively (Figure S5.1). In all cases, a high crystallinity and the phase purity of the samples was verified. The lattice parameter of Bixbyite is around 9.4 Å. The results of the refinement are shown in Figure S5.1 and Table S5.1. A possible explanation for the different results is rather found in the particle morphology of the Mn₂O₃ precursors. SEM images can be seen in Figure 5.5 together with the images of the starting material and the resulting α -MnO₂ products.

Depending on the calcined starting materials, the obtained Bixbyite precursors show clearly dissimilar morphologies. Particularly remarkable is the highly anisotropic “bone like” morphology of Mn₂O₃ [Mn(CH₃COO)₃], the Bixbyite phase which was made by decomposition of Manganese(III) acetate. It differs from the more isotropic “cloud like” morphologies of Mn₂O₃ [Mn₂O₃] and Mn₂O₃ [β -MnO₂]. Possibly, the more anisotropic morphology leads to a higher reactivity in the liquid phase promoting the formation of the thermodynamically preferred more crystalline product. It is noted, however, that the specific surface areas of all three Mn₂O₃ precursor are low between 1 and 6 m² g⁻¹ (Figure 5.5).

Although the morphologies of the starting materials and the Bixbyite precursors differs, all synthesized α -MnO₂ samples prefers a similar needle like morphology with particle length around 400 nm and width around 80 nm which are in the same magnitude like literature values.^{[98][108]} The needles are reported to be orientated along the 2x2 tunnels ([001] direction).^[98]

Only slight changes in crystal structure were determined by refinement of the powder diffraction data with the Rietveld method. The resulting α -MnO₂ phases show no noteworthy differences in their crystal structure. As representative of this group the Rietveld refinement results of α -MnO₂ [Mn(CH₃COO)₃] are graphically and tabularly depicted in Figure 5.9 and Table 5.2. A c parameter of around 2.85 Å and an a/b parameter of 9.85 Å were calculated.

Comparison of α -MnO₂ and Cryptomelane

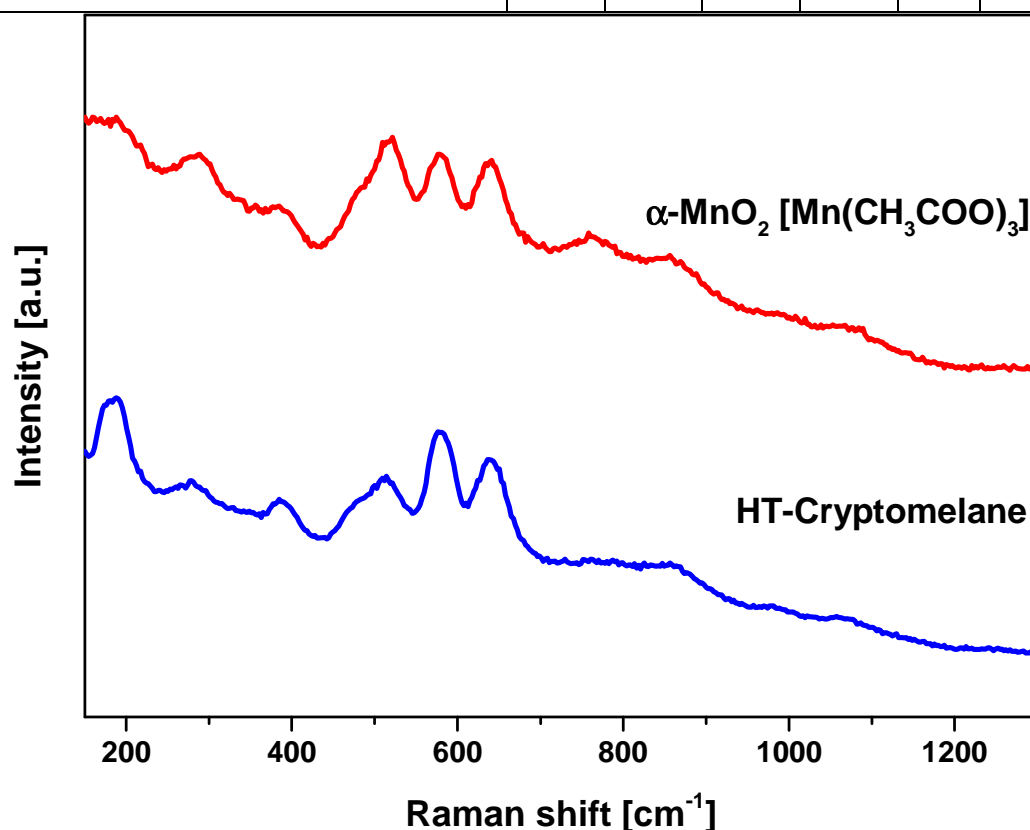
To compare structural features of α -MnO₂ (foreign cation free) and Cryptomelane (K⁺ containing), powder diffraction and Raman spectroscopy of α -MnO₂ [Mn(CH₃COO)₃] and HT-Cryptomelane were applied. As seen in Figure 5.9, both samples show a similar structure. However significant differences of the lattice parameters have been detected by Rietveld refinement (Table 5.2). While the lattice parameter c is roughly the same in both samples, the a and b axes of Cryptomelane show a small decrease, which may be a hint of a shrinking of the 2x2 tunnels.

The structural similarity was also verified with Raman spectroscopy (Figure 5.6, Table 5.1). The peaks found in the Raman spectrum of α -MnO₂ are in the same positions as in the case

of Cryptomelane. The peak assignment is therefore the same and in accordance with literature data. However, there are two main differences regarding peak intensities. The band at 189 cm⁻¹ was much less intense for pure α -MnO₂. This band is characteristic of α -MnO₂ structures and it is due to translational motion of the MnO₆ octahedra.^[96]

Table 5.1. Peaks observed in the Raman spectra.

<i>Sample</i>	<i>Raman wavenumber [cm⁻¹]</i>						
α -MnO ₂ [Mn(CH ₃ COO) ₃]	189	290	385	518	580	638	760
HT-Cryptomelane	189	280	385	514	578	639	-
Reference ^[97]	183	330	386	512	574	634	753

Figure 5.6. Raman spectra of α -MnO₂ and Cryptomelane.

Gao et al. compared α -MnO₂ phases containing different tunnel species (Li⁺, Na⁺ and K⁺) and detected a strong decreasing intensity of the band at 189 cm⁻¹ with decreasing atomic mass.^[95] Consequently, the less defined peak in α -MnO₂ may confirm the absence of any foreign metal cation in the tunnels which is in line with other studies.^{[34][31]} The second difference are the

relative peak intensities of the bands at 634 and 574 cm^{-1} , which was expected since the ratio of the bands is used to characterize tunnel species and to track ion exchange processes.^{[95][97]}

5.4.2 Electrocatalysis

In this work the electrocatalytic performance of α -MnO₂ was checked and an attempt is presented to correlate it with the peak-to-background ratio. As seen in Figure 5.7, all synthesized α -MnO₂ sample are able to catalyze the oxygen evolution reaction. The spread in activity is surprisingly high and ranged from 3.3 mA/cm^2 to 12.6 mA/cm^2 at 1.8 V. As shown in Figure 5.7, the highest activities are reached from samples with low crystallinity. So, the samples which were treated just for 3 hours or at a low temperature of 70 °C exhibit a current density higher than 10 mA/cm^2 at 1.8 V. In contrast to the α -MnO₂ sample with the highest peak-to-

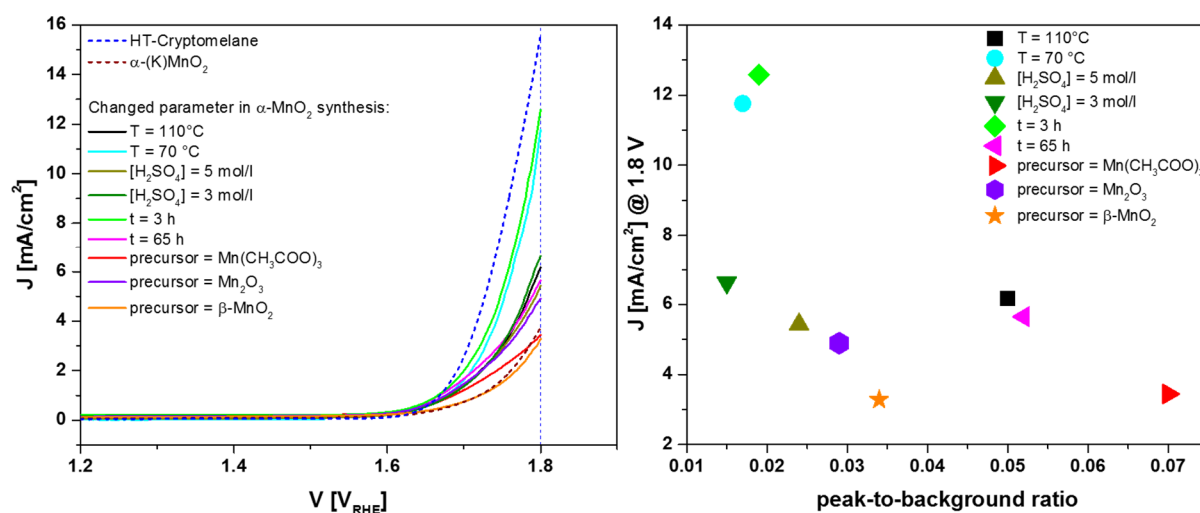


Figure 5.7. Left: OER activities of α -MnO₂ phases synthesized by acid digestion of Mn₂O₃ with varying parameters, right: Correlation of OER activities with the peak-to-background ratio of different α -MnO₂ phases.

background ratio of 0.7 which just shows a low value of 3.4 mA/cm^2 at 1.8 V. Nevertheless neither is the sample with the lowest PBR the most active one, nor does the least active sample exhibit the highest PBR. A clear trend of the crystallinity and the OER activity was not observed.

Ion insertion

Like mentioned before α -MnO₂ is known for incorporating easily potassium into the 2x2 tunnels what usually occurs while synthesis. To investigate if K⁺ insertion take place while running the oxygen evolution reaction in KOH solution different experiments were carried out. Figure 5.8 shows the Raman spectra of the sample α -MnO₂ [Mn(CH₃COO)₃] before and after

exposing it to 0.01 M KOH. The exposure duration was varied between 2 and 160 min. For the purpose of comparison, the spectra of HT-Cryptomelane untreated and treated for 2 min in 0.01 M KOH are shown in the same graphic. As expected for a fully K⁺-loaded sample, the HT-Cryptomelane seem unaffected by the K⁺ solution, but not the pure α -MnO₂. The position of the bands are maintained but the intensities of the bands (as pointed out by arrows) change and approximate to the one of Cryptomelane. This is an indication that K⁺ from the electrolyte may be easily incorporated in the tunnels of α -MnO₂. The most drastic change is observed between the untreated sample and the first spectrum, which was recorded after 2 min of exposure to KOH. This suggests that the insertion occurs rather instantaneously at the moment of bringing the material and the solution into contact, which agrees with literature.^[110]

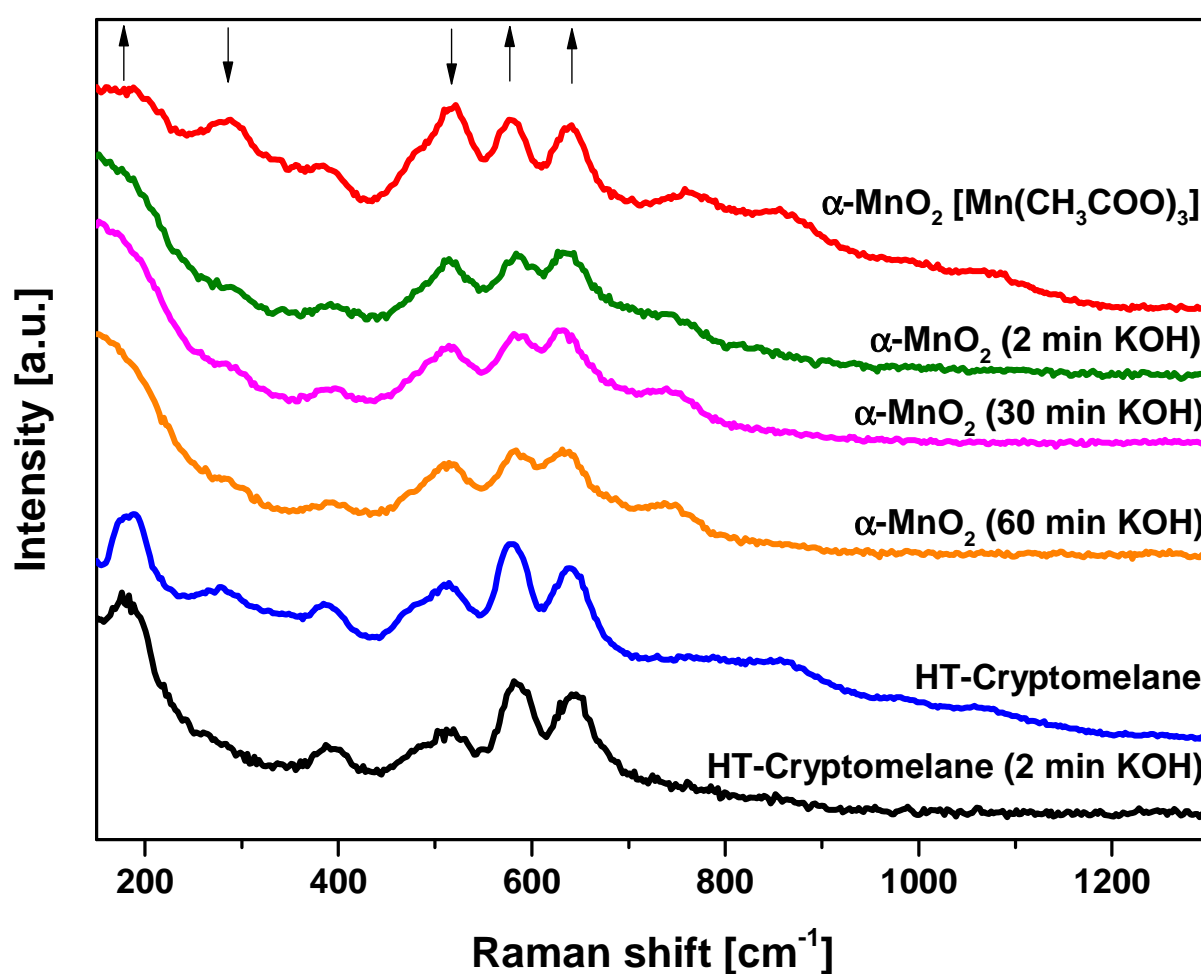


Figure 5.8. Raman spectra of α -MnO₂ and Cryptomelane and impact of KOH treatment.

This observation was confirmed with another experiment subjecting the sample α -MnO₂ [Mn(CH₃COO)₃] to 1 M KOH solution for three different stirring times (1 min, 15 min and 60 min). After washing and drying the obtained products were analyzed by atomic absorption spectroscopy and Powder diffraction. The potassium to manganese ratios shown in Table 5.2

verify the potassium insertion process in pure α -MnO₂ within the first 60 s. After one minute no noteworthy further changes are detectable. The potassium amount always lies around 10 cat.-%, which is similar with the potassium amount in HT-Cryptomelane. The incorporation of tunnel cations is also clearly indicated by changes in structure. Rietveld refinements reveals that the a/b lattice parameter of α -MnO₂ decreases through incorporating potassium and consequently converge to the one of Cryptomelane (Figure 5.9). Based on the property of α -MnO₂ to insert potassium from the electrolyte in the crystal structure in short time it can be assumed that right at the beginning of the OER measurement a transformation from α -MnO₂ to Cryptomelane takes place. Consequently, the influence of tunnel potassium in OER is non-determinable by simple comparison of the catalytic performance of α -MnO₂ and Cryptomelane in KOH solution.

Table 5.2. Molar ratio of potassium and manganese measured by AAS and structural data and lattice parameters of different α -MnO₂ and Cryptomelane samples obtained by Rietveld refinement.

<i>Sample</i>	<i>K/Mn ratio</i>	<i>Structural data and lattice parameter</i>	
α -MnO ₂ [Mn(CH ₃ COO) ₃]	0.00	a = b = 9.848(3) Å c = 2.8526(9) Å $\alpha = \beta = \gamma = 90^\circ$	<i>Structure Type:</i> α -MnO ₂ <i>Crystal System:</i> tetragonal <i>Space Group:</i> I 4/m (87) <i>Formula Units per Cell:</i> 8
α -MnO ₂ (1 min KOH)	0.09	a = b = 9.801(3) Å c = 2.8491(7) Å $\alpha = \beta = \gamma = 90^\circ$	
α -MnO ₂ (15 min KOH)	0.10	a = b = 9.800(3) Å c = 2.8480(8) Å $\alpha = \beta = \gamma = 90^\circ$	
α -MnO ₂ (60 min KOH)	0.11	a = b = 9.801(3) Å c = 2.8478(8) Å $\alpha = \beta = \gamma = 90^\circ$	
α -(K)MnO ₂	0.09	a = b = 9.802(2) Å c = 2.8475(6) Å $\alpha = \beta = \gamma = 90^\circ$	
HT-Cryptomelane	0.13	a = b = 9.798(3) Å c = 2.8512(9) Å $\alpha = \beta = \gamma = 90^\circ$	

The OER performances of α -(K)MnO₂ and HT-Cryptomelane rather indicate a strong impact of the synthesis route. The sample α -(K)MnO₂ was synthesized via the same acid digestion

route like α -MnO₂ [Mn(CH₃COO)₃]. During the acidic treatment a K⁺-salt was added to the solution obtaining a Cryptomelane. Despite the incorporation of potassium during synthesis, the OER activity shows no noteworthy changes in comparison to the pure α -MnO₂ [Mn(CH₃COO)₃]. By contrast, HT-Cryptomelane was synthesized hydrothermally and reveals a much higher OER activity with around 15 mA/cm² at 1.8 V.

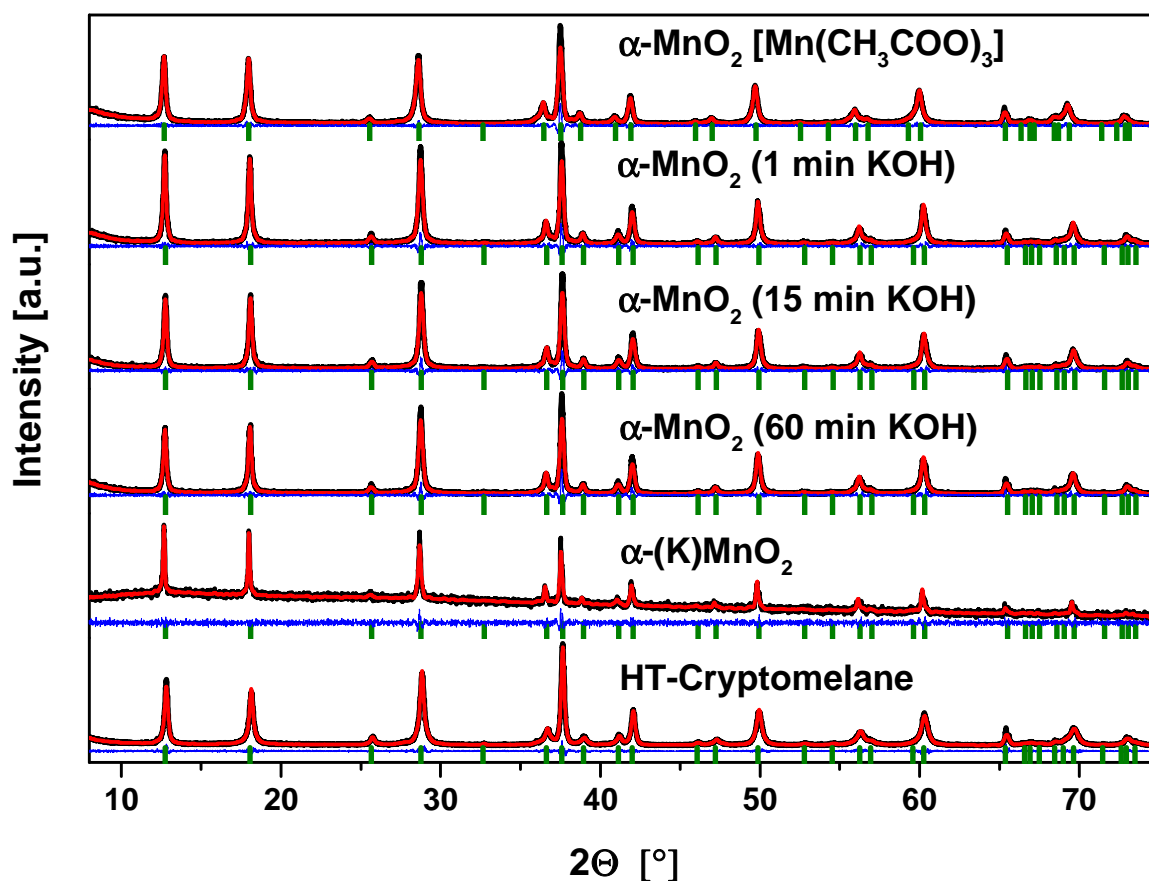


Figure 5.9. Graphical results of Rietveld refinement of the powder diffraction data of different α -MnO₂ and Cryptomelane samples.

Electrocatalytic stability and Post-OER-XRD

The stability of the α -MnO₂ [Mn(CH₃COO)₃] as representative of the α -MnO₂ samples during catalysis was examined. For this measurement the potential was fixed at 1.8 V for 60 min while the current was detected. The obtained current-time curve is depicted in Figure 5.10 and shows a negative slope from the beginning. The current flow decreased by almost 70% within the first 10 min. To investigate the catalyst after this deactivation, a Powder XRD pattern was recorded followed by a Rietveld refinement of the data. The result is graphically and

tabularly shown in Figure 5.10 and Table 5.3. The low reflection intensities and the high background are caused by the tiny amount of catalyst used for the electrocatalysis and subsequently for the XRD measurement. The examination reveals that the catalyst maintained its

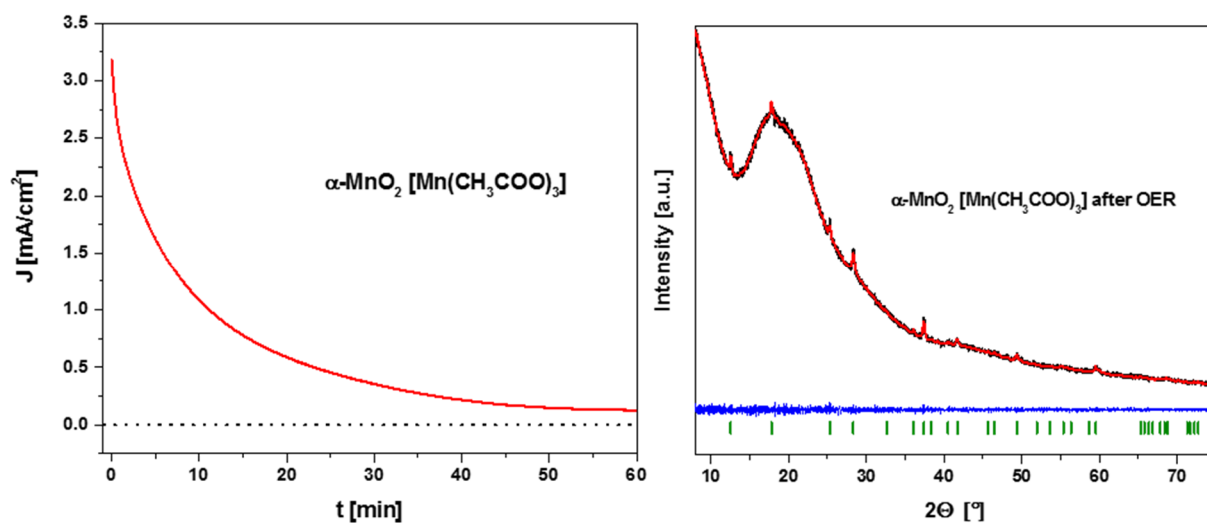


Figure 5.10. Long-time OER activities of α -MnO₂ (left) and graphical results of Rietveld refinement of the powder diffraction data of α -MnO₂ applied on adhesive tape after OER measurement (right).

bulk structure. However changes of lattice parameter are detectable. The a/b parameter increases from 9.85 Å to 9.95 Å while the c parameter keeps constant during the measurement. The effect is not caused by the incorporation of potassium considering the before described experiments by which the K^+ insertion leads to a shrinking of the unit cell. Possibly the observed expansion is induced by the applied potential and associated with the deactivation phenomenon. However for a proper interpretation further investigations are necessary.

Table 5.3. Lattice parameter of α -MnO₂ before and after OER measurement.

Sample	α -MnO ₂ [Mn(CH ₃ COO) ₃]	α -MnO ₂ [Mn(CH ₃ COO) ₃] after OER
Lattice parameter	a = b = 9.848(3) Å c = 2.8526(9) Å $\alpha = \beta = \gamma = 90^\circ$	a = b = 9.945(13) Å c = 2.853(3) Å $\alpha = \beta = \gamma = 90^\circ$

5.5 Conclusion

α -MnO₂ samples were prepared by the thermal and acidic treatment of Bixbyite precursors. The impact of the main synthetic parameters reaction time, H₂SO₄ concentration, reaction temperature and precursor was investigated. Therefore the before mentioned parameters were varied and the obtained α -MnO₂ powders measured by X-Ray diffraction. The success of synthesis is defined by the product crystallinity which is quantified by a peak-to background ratio. All four parameters influence the crystallinity of the product. The main impact can be attributed to the sulfuric acid concentration which should be set to 4 mol l⁻¹ to gain a high crystalline product. Additionally a reaction temperature of not less than 80 °C and an adequate reaction time should be chosen. A substantial influence on the product is also related to the Mn₂O₃ precursor history. Three kinds of Mn₂O₃ precursors were prepared by the calcination of different starting materials. In dependence of the chosen educt the obtained Mn₂O₃ samples differ regarding their morphology what the reason for the varying crystallinity of the α -MnO₂ products. All α -MnO₂ samples are able to catalyze the oxygen evolution reaction. Current densities between 3.3 mA/cm² and 12.6 mA/cm² at 1.8 V were measured. A long-time stability test shows a fast loss of activity. The incorporation of potassium within the first minute due to the contact with KOH solution is verified by AAS, Raman and XRD measurements. The insertion of K⁺ in α -MnO₂ while synthesis doesn't increase the activity of the product however Cryptomelane obtained by using a hydrothermal route exhibits the highest activity of the investigated samples. The incorporation leads to a reduction of the unit cell of α -MnO₂ however an enlargement while electrocatalysis can be observed what might be attributed to the applied potential.

5.6 Acknowledgement

The authors acknowledge the Financial support of the BMBF funded project MANGAN (FKZ: 03SF0511B) and of the State of North Rhine-Westphalia through the University of Duisburg-Essen, Faculty of Chemistry.

5.7 Supporting information

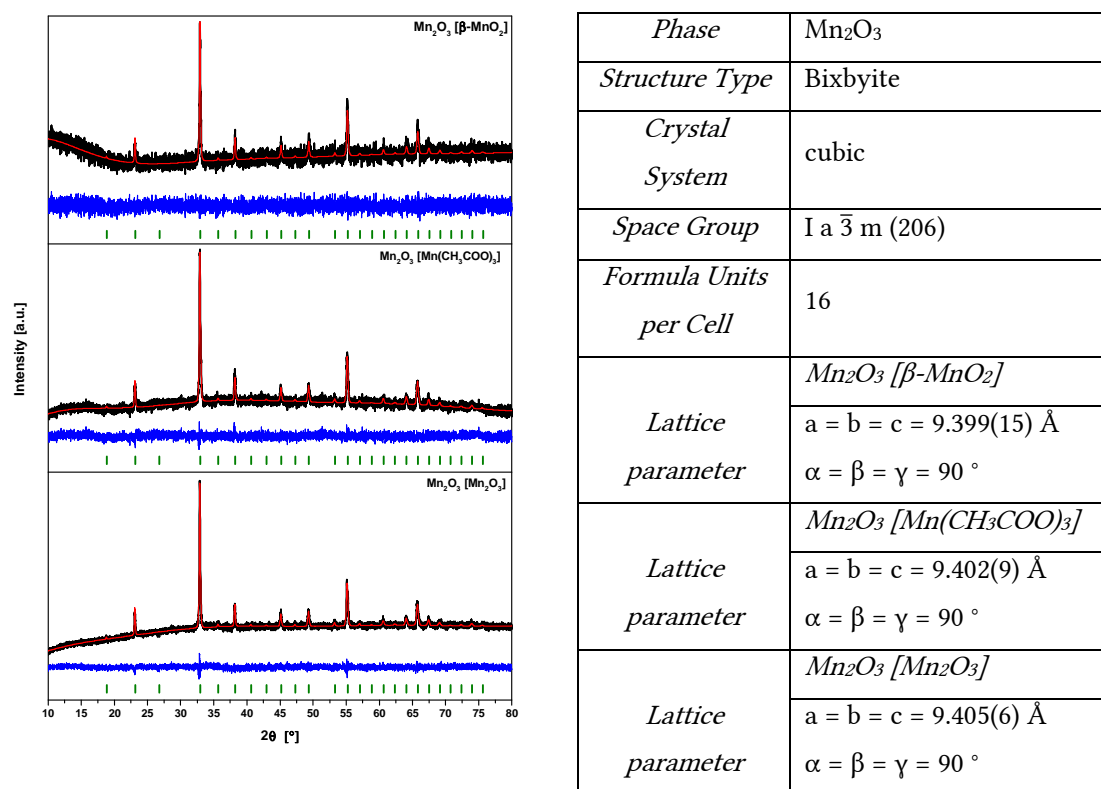


Figure S5.1./Table S5.1. Graphically results (left), structural data and lattice parameter (right) of the Rietveld refinement of the powder diffraction data of Mn₂O₃ precursors.

Table S5.2. Results of Rietveld refinement of Mn₂O₃ and α -MnO₂ and Cryptomelane phases.

<i>Sample</i>	R_{exp}	R_{wp}	R_p	R_{exp}'	R_{wp}'	R_p'	<i>GOF</i>	R_{Bragg}
<i>Mn₂O₃</i> <i>[\beta-MnO₂]</i>	4.58	4.64	3.71	11.19	11.35	11.85	1.01	0.900
<i>Mn₂O₃</i> <i>[\beta-MnO₂]</i>	2.57	2.80	2.21	7.57	8.26	9.23	1.09	0.920
<i>Mn₂O₃</i> <i>[Mn₂O₃]</i>	2.22	2.43	1.91	6.69	7.32	9.00	1.09	0.726
<i>α-MnO₂</i> <i>[Mn(CH₃COO)₃]</i>	2.17	2.71	2.02	6.56	8.20	8.74	1.25	2.665
<i>α-MnO₂</i> <i>(1 min KOH)</i>	10.99	12.75	9.67	0.35	0.41	0.40	1.16	1.334
<i>α-MnO₂</i> <i>(15 min KOH)</i>	11.76	13.53	10.26	0.32	0.37	0.37	1.15	1.633
<i>α-MnO₂</i> <i>(60 min KOH)</i>	11.93	13.79	10.34	0.32	0.37	0.36	1.16	1.712
<i>α-(K)MnO₂</i>	2.46	2.68	2.10	1.32	1.45	1.45	1.09	0.473
<i>HT-Cryp.</i>	10.31	12.91	9.51	0.33	0.41	0.43	1.25	1.533
<i>α-MnO₂</i> <i>after OER</i>	1.37	1.39	0.97	1.15	1.17	0.87	1.01	0.051

6. Conclusion and Outlook

Each of the three previous „Results and Discussion“ chapters contains an independent detailed conclusion part. The following is a rough chapter-spanning overview of the basic findings in terms of the suitability of manganese oxides as OER electrocatalysts combined with a brief outlook.

The OER activity screening discussed in Chapter 3 reveals a surprisingly high spread of the electrocatalytic performance in dependence of the manganese oxide species. The nearly inactive catalysts Mn_5O_8 , K-Birnessite, Bixbyite and Hausmannite only show a current density of less than 1 mA cm^{-2} at a potential of 1.8 V. The most efficient catalysts can be found within the hollandite-type oxides lead by Cryptomelane, which reaches a value of more than 15 mA cm^{-2} at a potential of 1.8 V. In the scope of a subsequent Cryptomelane study (Chapter 4) the current density was even doubled to over 30 mA cm^{-2} by changing the synthesis method. The enhancement is attributed to optimized material related properties. A particularly noteworthy influencing factor is found in the material conductivity. Transferring this knowledge to further manganese oxide species might help to improve their catalytic efficiency. The role of the tunnel cation in hollandite-type oxides is not finally clarified. On the one hand the potassium and ammonium containing $\alpha\text{-MnO}_2$ phases (NH_4 -Hollandite and Cryptomelane) reported in Chapter 3 reaches much higher activities than pure $\alpha\text{-MnO}_2$ (here worthy of mention is the usage of the same synthesis route of NH_4 -Hollandite and $\alpha\text{-MnO}_2$). On the other hand, the $\alpha\text{-MnO}_2$ study reported in Chapter 5 indicates no advantage or disadvantage if potassium is incorporated or absent in the fresh catalyst. In the case of pure $\alpha\text{-MnO}_2$ the study even shows the fast insertion of K^+ in the structure during the measurement and thus the transition to Cryptomelane without reaching higher activities. One of the most critical issues that needs to be solved is the fast decreasing activity during the reaction of all considered manganese oxides. In situ and ex situ studies (Chapter 4 and 5) reveal the structural stability of the bulk material of $\alpha\text{-MnO}_2$ and Cryptomelane. To identify the responsible causes for the fast activity loss, further investigations are crucial. The structural endurance of Cryptomelane during the water oxidation (with Ce^{4+}) and H_2O_2 decomposition experiments, emphasize the possibility to run the OER catalysis in neutral and acidic conditions. This represents an additional approach for future research. Finally, it can be concluded that the extensive number of known species and the manifold and tuneable material properties suggest a high potential of manganese oxides within the field of electrocatalysis.

7. References

- [1] Y. Gorlin, T. F. Jaramillo, *J. Am. Chem. Soc.* **2010**, *132*, 13612–13614.
- [2] S. Trasatti, *Electrochim. Acta* **1984**, *29*, 1503–1512.
- [3] *Acta Cryst.* **1992**, *48*, 922–946.
- [4] H. M. Rietveld, *Acta Cryst.* **1967**, *22*, 151–152.
- [5] R. A. Young, *The Rietveld Method*, Oxford University Press Publication, Oxford, United Kingdom, **1995**.
- [6] K. Kopitzki, P. Herzog, *Einführung in die Festkörperphysik*, Springer Berlin Heidelberg, Berlin, Heidelberg, **2017**.
- [7] L. S. Gerd, G. T. Robert, R. Schwarzer, H. Behnken, C. Genzel, *Moderne Röntgenbeugung, Röntgendiffraktometrie für Materialwissenschaftler, physiker Und Chemiker*, Vieweg+Teubner, Wiesbaden, **2009**.
- [8] D. A. Weber, Synthese und Charakterisierung neuer Oxide und Oxidnitride der Elemente der 5. und 6. Gruppe des Periodensystems, Dissertation, TU Berlin, **2014**.
- [9] H. Ahmad, S. K. Kamarudin, L. J. Minggu, M. Kassim, *Renew. Sustain. Energy Rev.* **2015**, *43*, 599–610.
- [10] C. E. Frey, P. Kurz, *Chem. Eur. J.* **2015**, *21*, 14958–14968.
- [11] C. L. Muhich, B. D. Ehrhart, I. Al-Shankiti, B. J. Ward, C. B. Musgrave, A. W. Weimer, *Wiley Interdiscip. Rev. Energy Environ.* **2016**, *5*, 261–287.
- [12] M. Wang, Z. Wang, X. Gong, Z. Guo, *Renew. Sustain. Energy Rev.* **2014**, *29*, 573–588.
- [13] M. M. Rashid, M. K. Al Mesfer, H. Naseem, M. Danish, *Int. J. Eng. Adv. Technol.* **2015**, 2249–8958.
- [14] T. Teetz, *Experimentelle Elektrochemie*, De Gruyter, Berlin, Boston, **2017**.
- [15] R. L. Doyle, M. E. G. Lyons, *Photoelectrochemical Solar Fuel Production: From Basic Principles to Advanced Devices*, Springer, Cham, Switzerland, **2016**.
- [16] I. C. Man, H. Y. Su, F. Calle-Vallejo, H. A. Hansen, J. I. Martínez, N. G. Inoglu, J. Kitchin, T. F. Jaramillo, J. K. Nørskov, J. Rossmeisl, *ChemCatChem* **2011**, *3*, 1159–1165.
- [17] R. N. DeGuzman, Y.-F. Shen, E. J. Neth, S. L. Suib, C. L. O’Young, S. Levine, J. M. Newsam, *Chem. Mater.* **1994**, *6*, 815–821.
- [18] S. Turner, P. R. Buseck, *Sci.* **1981**, *212*, 1024–1027.
- [19] Y. Shen, R. Zerger, R. DeGuzman, *Sci.* **1993**, *260*, 511–515.
- [20] A. D. Wadsley, *Am. Miner.* **1950**, *35*, 485–499.

- [21] G. G. Xia, W. Tong, E. N. Tolentino, N. G. Duan, S. L. Brock, J. Y. Wang, S. L. Suib, T. Ressler, *Chem. Mater.* **2001**, *13*, 1585–1592.
- [22] X. Shen, Y. Ding, J. Liu, K. Laubernds, R. P. Zerger, M. Polverejan, Y. C. Son, M. Aindow, S. L. Suib, *Chem. Mater.* **2004**, *16*, 5327–5335.
- [23] S. L. Brock, N. Duan, Z. R. Tian, O. Giraldo, H. Zhou, S. L. Suib, *Chem. Mater.* **1998**, *10*, 2619–2628.
- [24] T. Chen, H. Dou, X. Li, X. Tang, J. Li, J. Hao, *Microporous Mesoporous Mater.* **2009**, *122*, 270–274.
- [25] O. Ghodbane, J. L. Pascal, B. Fraisse, F. Favier, *ACS Appl. Mater. Interfaces* **2010**, *2*, 3493–3505.
- [26] A. M. Byström, E. W. Lund, L. K. Lund, M. Hakala, *Acta Chem. Scand.* **1949**, *3*, 163–173.
- [27] R. M. McKenzie, *Mineral. Mag.* **1971**, *38*, 493–502.
- [28] W. Feitknecht, *Pure Appl. Chem.* **1964**, *9*, 423–440.
- [29] J. E. Post, C. W. Burnham, *Am. Mineral.* **1986**, *71*, 1178–1185.
- [30] Q. Feng, H. Kanoh, Y. Miyai, K. Ooi, *Chem. Mater.* **1995**, *7*, 148–153.
- [31] N. Kijima, T. Ikeda, K. Oikawa, F. Izumi, Y. Yoshimura, *J. Solid State Chem.* **2004**, *177*, 1258–1267.
- [32] M. Tsuji, M. Abe, *Bull. Chem. Soc. Jpn.* **1985**, *58*, 1109–1114.
- [33] J. W. Gruner, *Am. Miner.* **1943**, 497–506.
- [34] M. H. Rossouw, D. C. Liles, M. M. Thackeray, W. I. F. David, S. Hull, *Mater. Res. Bull.* **1992**, *27*, 221–230.
- [35] W. Xu, Z. Deng, G. Li, *Ind. Eng. Chem. Res.* **2012**, *51*, 16188–16195.
- [36] X. Chen, Y. F. Shen, S. L. Suib, C. L. O’Young, *J. Catal.* **2001**, *197*, 292–302.
- [37] Y. Li, Z. Fan, J. Shi, Z. Liu, J. Zhou, W. Shangguan, *Catal. Today* **2015**, *256*, 178–185.
- [38] M. T. Nguyen Dinh, J. M. Giraudon, A. M. Vandenbroucke, R. Morent, N. De Geyter, J. F. Lamonier, *J. Hazard. Mater.* **2016**, *314*, 88–94.
- [39] M. Sun, L. Yu, F. Ye, G. Diao, Q. Yu, Z. Hao, Y. Zheng, L. Yuan, *Chem. Eng. J.* **2013**, *220*, 320–327.
- [40] L. Sun, Q. Cao, B. Hu, J. Li, J. Hao, G. Jing, X. Tang, *Appl. Catal. A Gen.* **2011**, *393*, 323–330.
- [41] C. Almquist, M. Krekeler, L. Jiang, *Chem. Eng. J.* **2014**, *252*, 249–262.
- [42] L. R. Pahalagedara, S. Dharmarathna, C. K. King’ ondu, M. N. Pahalagedara, Y.-T. Meng, C.-H. Kuo, S. L. Suib, *J. Phys. Chem. C* **2014**, *118*, 20363–20373.
- [43] H. Miura, H. Kudou, J. H. Choi, Y. Hariya, *Jour. Fac. SeL, Hokkaido Univ., Ser. IV*

- 1990, 22, 611–617.
- [44] M. Fleischer, A. D. Wallace, *Econ. Geol.* **1943**.
- [45] G. Vaux, H. Bennett, *Mineral. Mag.* **1937**, 24, 521–526.
- [46] H. F. McMurdie, E. Golovato, *J. Res. Natl. Bur. Stand. Study* **1948**, 41, 589.
- [47] M. M. Thackeray, M. H. Rossouw, R. J. Gummow, D. C. Liles, K. Pearce, a. De Kock, W. I. F. David, S. Hull, *Electrochim. Acta* **1993**, 38, 1259–1267.
- [48] D. W. Murphy, F. J. Di Salvo, J. N. Carides, J. V. Waszczak, *Mater. Res. Bull.* **1978**, 13, 1395–1402.
- [49] A. D. Wadsley, *J. Am. Chem. Soc.* **1950**, 72, 1781–1784.
- [50] H. F. McMurdie, *J. Electrochem. Soc.* **1944**, 86, 313–326.
- [51] L. H. P. Jones, A. A. Milne, *Mineral. Mag.* **1956**, 31, 283–288.
- [52] J. E. Post, D. R. Veblen, *Am. Mineral.* **1990**, 75, 477–489.
- [53] S. Bach, J. P. Pereira-Ramos, N. Baffier, R. Messina, *Electrochim. Acta* **1991**, 36, 1595–1603.
- [54] M. Nakayama, T. Kanaya, J.-W. Lee, B. N. Popov, *J. Power Sources* **2008**, 179, 361–366.
- [55] K. Xhaxhiu, *J. Met. Nanotechnologies* **2015**, 23–32.
- [56] C. E. Frey, M. Wiechen, P. Kurz, *Dalt. Trans.* **2014**, 43, 4370–4379.
- [57] A. C. Thenuwara, S. L. Shumlas, N. H. Attanayake, Y. V. Aulin, I. G. McKendry, Q. Qiao, Y. Zhu, E. Borguet, M. J. Zdilla, D. R. Strongin, *ACS Catal.* **2016**, 6, 7739–7743.
- [58] A. C. Thenuwara, S. L. Shumlas, N. H. Attanayake, E. B. Cerkez, I. G. McKendry, L. Frazer, E. Borguet, Q. Kang, M. J. Zdilla, J. Sun, et al., *Langmuir* **2015**, 31, 12807–12813.
- [59] S. L. Penfield, H. W. Foote, *Am. J. Sci.* **1897**, 105–108.
- [60] L. Pauling, M. D. Shappell, *Z. Krist.* **1930**, 75, 128–142.
- [61] A. Ramos-Gallardo, A. Vegas, *J. Solid State Chem.* **1995**, 119, 131–133.
- [62] J. Cao, Y. Zhu, L. Shi, L. Zhu, K. Bao, S. Liu, Y. Qian, *Eur. J. Inorg. Chem.* **2010**, 1172–1176.
- [63] Z. Yang, Y. Zhang, W. Zhang, X. Wang, Y. Qian, X. Wen, S. Yang, *J. Solid State Chem.* **2006**, 179, 679–684.
- [64] S. Imamura, M. Shono, N. Okamoto, A. Hamada, S. Ishida, *Appl. Catal. A Gen.* **1996**, 142, 279–288.
- [65] F. Hausmann, *Handb. der Mineral.* **1813**, 293.
- [66] G. Aminoff, *Zeitschr. f. Krist.* **1926**, 64, 475–490.
- [67] D. Jarosch, *Mineral. Petrol.* **1987**, 37, 15–23.
- [68] M. Baldi, E. Finocchio, F. Milella, G. Busca, *Appl. Catal. B Environ.* **1998**, 16, 43–51.
- [69] W. B. S. Machini, C. S. Martin, M. T. Martinez, S. R. Teixeira, H. M. Gomes, M. F. S.

- Teixeira, *Sensors Actuators B* **2013**, *181*, 674–680.
- [70] H. R. Oswald, M. J. Wampetich, *Helv. Chim. Acta* **1967**, *50*, 2023–2034.
- [71] D. Jeong, K. Jin, S. E. Jerng, H. Seo, D. Kim, S. H. Nahm, S. H. Kim, K. T. Nam, *ACS Catal.* **2015**, *5*, 4624–4628.
- [72] T. Ohzuku, M. Kitagawa, K. Sawai, T. Hiroi, *J. Electrochem. Soc.* **1991**, *138*, 360–365.
- [73] H. Ma, J. Shen, M. Shi, B. Yan, N. Li, M. Ye, *Mater. Res. Bull.* **2011**, *46*, 1461–1466.
- [74] T. Gao, H. Fjellvg, P. Norby, *Nanotechnology* **2009**, *20*, 055610.
- [75] S. Ching, J. A. Landrigan, M. L. Jorgensen, *Chem. Mater.* **1995**, *7*, 1604–1606.
- [76] W. L. He, Y. C. Zhang, X. X. Zhang, H. Wang, H. Yan, *J. Cryst. Growth* **2003**, *252*, 285–288.
- [77] H. R. Oswald, M. J. Wampetich, *Helv. Chim. Acta* **1967**, *50*, 2023–2034.
- [78] C. C. L. McCrory, S. Jung, J. C. Peters, T. F. Jaramillo, *J. Am. Chem. Soc.* **2013**, *135*, 16977–16987.
- [79] I. Spanos, A. A. Auer, S. Neugebauer, X. Deng, H. Tüysüz, R. Schlögl, *ACS Catal.* **2017**, *7*, 3768–3778.
- [80] A. A. Bolzan, C. Fong, B. J. Kennedy, C. J. Howard, *Aust. J. Chem.* **1993**, *46*, 939–944.
- [81] A. Gaillot, V. Drets, A. Manceau, B. Lanson, *Microporous Mesoporous Mater.* **2007**, *98*, 267–282.
- [82] X. F. Wang, G. H. Li, Q. X. Chu, X. Y. Liu, S. H. Feng, *Chem. J. Chinese Univ.* **2007**, *28*, 821–823.
- [83] Q. Chu, X. Wang, X. Zhang, Q. Li, X. Liu, *Inorg. Chem.* **2011**, *50*, 2049–2051.
- [84] Z. Sun, D. Shu, H. Chen, C. He, S. Tang, J. Zhang, *J. Power Sources* **2012**, *216*, 425–433.
- [85] D. C. Golden, J. B. Dixon, C. C. Chen, *Clays Clay Miner.* **1986**, *34*, 511–520.
- [86] Y. Meng, W. Song, H. Huang, Z. Ren, S. Chen, S. L. Suib, *J. Am. Chem. Soc.* **2014**, *136*, 11452–11464.
- [87] R. Zhang, T. S. Arthur, C. Ling, F. Mizuno, *J. Power Sources* **2015**, *282*, 630–638.
- [88] D. C. Golden, C. C. Chen, J. B. Dixon, *Clays Clay Miner.* **1987**, *35*, 271–280.
- [89] X. Wang, Y. Li, *CHEM. COMMUN.* **2002**, 764–765.
- [90] Y. S. Ding, X. F. Shen, S. Sithambaram, S. Gomez, R. Kumar, V. M. B. Crisostomo, S. L. Suib, M. Aindow, *Chem. Mater.* **2005**, *17*, 5382–5389.
- [91] M. Heimann, Wasserspaltung, Synthese Und Charakterisierung von Co-Katalysator / Photohalbleiter-Kompositen Für Die Photokatalytische, Fakultät für Chemie der Universität Duisburg-Essen, **2017**.
- [92] F. Liu, J. J. Concepcion, J. W. Jurss, T. Cardolaccia, J. L. Templeton, T. J. Meyer, *Inorg. Chem.* **2008**, *47*, 1727–1752.

- [93] M. M. Najafpour, T. Ehrenberg, M. Wiechen, P. Kurz, *Angew. Chemie - Int. Ed.* **2010**, *49*, 2233–2237.
- [94] A. F. Holleman, E. Wiberg, *Lehrbuch Der Anorganischen Chemie*, De Gruyter, Berlin, **2007**.
- [95] T. Gao, H. Fjellvåg, P. Norby, *Anal. Chim. Acta* **2009**, *648*, 235–239.
- [96] Y. Xie, Y. Yu, X. Gong, Y. Guo, Y. Guo, Y. Wang, G. Lu, *CrystEngComm* **2015**, *17*, 3005–3014.
- [97] T. Gao, M. Glerup, F. Krumeich, R. Nesper, H. Fjellvåg, P. Norby, *J. Phys. Chem. C* **2008**, *112*, 13134–13140.
- [98] Y. Shao-Horn, S. A. Hackney, C. S. Johnson, M. M. Thackeray, *1. Electrochem. Soc.* **1998**, *145*, 582–589.
- [99] T. Gao, P. Norby, *Eur. J. Inorg. Chem.* **2013**, 4948–4957.
- [100] K. Selvakumar, S. M. Senthil Kumar, R. Thangamuthu, G. Kruthika, P. Murugan, *Int. J. Hydrogen Energy* **2014**, *39*, 21024–21036.
- [101] W. Zhang, Z. Yang, X. Wang, Y. Zhang, X. Wen, S. Yang, *Catal. Commun.* **2006**, *7*, 408–412.
- [102] M. Tsuji, S. Komarneni, *J. Mater. Res.* **1993**, *8*, 611–616.
- [103] Q. Feng, T. Horiuchi, T. Mitsusio, K. Yanagisawa, N. Yamasaki, *J. Mater. Sci. Lett.* **1999**, *18*, 1375–1378.
- [104] J. Brenet, A. Grund, *Comptes rendus l'Académie des Sci.* **1956**, *242*, 2343.
- [105] D. K. Walanda, *Proceeding Int. Semin. Chem.* **2008**, *2008*, 180–184.
- [106] D. K. Walanda, G. A. Lawrance, S. W. Donne, *J. Solid State Chem.* **2009**, *182*, 1336–1342.
- [107] D. K. Walanda, G. a. Lawrance, S. W. Donne, *J. Power Sources* **2005**, *139*, 325–341.
- [108] N. Kijima, Y. Sakata, Y. Takahashi, J. Akimoto, T. Kumagai, K. Igarashi, T. Shimizu, *Solid State Ionics* **2009**, *180*, 616–620.
- [109] M. Xu, L. Kong, W. Zhou, H. Li, *J. Phys. Chem. C* **2007**, *111*, 19141–19147.
- [110] S. Cheng, L. Yang, D. Chen, X. Ji, Z. jie Jiang, D. Ding, M. Liu, *Nano Energy* **2014**, *9*, 161–167.
- [111] A.-C. Gaillot, D. Flot, V. A. Drits, A. Manceau, M. Burghammer, B. Lanson, *Chem. Mater.* **2003**, *15*, 4666–4678.
- [112] H. Klein, J. David, *Acta Crystallogr. Sect. A Found. Crystallogr.* **2011**, *67*, 297–302.
- [113] E. Cockayne, I. Levin, H. Wu, A. Llobet, *Phys. Rev. B* **2013**, 1–11.

A. Appendix

Parts of the research results originated from the work as PhD student were published in scientific journals or already prepared to do so and presented at scientific conferences. Selected contributions are listed below.

A.1 List of Publications

Paper I

Effect of Ni Incorporation into Malachite Precursors on the Catalytic Properties of the Resulting Nanostructured CuO/NiO Catalysts

Klaus Friedel Ortega, Andreas Hüttner, Justus Heese, Malte Behrens

Eur. J. Inorg. Chem. 2016, 2063–2071

Own contribution: Refinement, interpretation and evaluation of structural data.

Paper II

Ammonia Decomposition and Synthesis over Multinary Magnesioferrites: Promotional Effect of Ga on Fe Catalysts for the Decomposition Reaction

Klaus Friedel Ortega, Denise Rein, Christian Lüttmann, Justus Heese, Fatih Özcan, Markus Heidelmann, Jan Folke, Kevin Kähler, Robert Schlögl, Malte Behrens

ChemCatChem 2017, 9, 659 –671

Own contribution: XRD measurements. Refinement, interpretation and evaluation of structural data.

Paper III

Continuous Hydrothermal Flow Synthesis of $\text{Co}_{1-x}\text{Ni}_x\text{Fe}_2\text{O}_4$ ($x = 0 - 0.8$) Ferrite Nanoparticles: Catalysts in the CO Oxidation and in the Oxygen Evolution Reaction

Yu Xu, Fatih Özcan, Philipp Zielke, Stefanie Hoffmann, Justus Heese, Manuel Heimann, Kalapu Chakrapani, Malte Behrens, Søren Bredmose Simonsen, Poul Norby, Peter Vang Hendriksen, Ragnar Kiebach

Manuscript in preparation

Own contribution: Supporting advice concerning OER and XRD measurements and interpretation.

Paper IV

Topotactic Synthesis of Porous Cobalt Ferrite Platelets from a Layered Double Hydroxide Precursor and Their Application in Oxidation Catalysis

Klaus Friedel Ortega, Sven Anke, Soma Salamon, Fatih Özcan, Justus Heese, Corina Andronescu, Joachim Landers, Heiko Wende, Wolfgang Schuhmann, Martin Muhler, Thomas Lunkenbein, Malte Behrens

Chem. Eur. J. 2017, 23, 12443–12449

Own contribution: XRD measurements. Refinement, interpretation and evaluation of structural data.

Paper V

Synthesis, Characterization and OER Activity of different Manganese Oxides

Justus Heese-Gärtlein, Malte Behrens

In manuscript, included in the thesis

Paper VI

Cryptomelane as Water Oxidation Catalyst: Factors Influencing the OER Activity

Justus Heese-Gärtlein, D. M. Morales, W. Schuhmann, Malte Behrens

In manuscript, included in the thesis

Paper VII

Controlling the Crystallinity of α -MnO₂ Synthesized by Acid Digestion of Bixbyite and its Electrocatalytic OER Activity

Justus Heese-Gärtlein, D. M. Morales, Fatih Özcan, W. Schuhmann, Malte Behrens

In manuscript, included in the thesis

A.2 List of Conference Contributions

- 03.2016 49. Jahrestreffen Deutscher Katalytiker, Weimar/Germany
Structural effects of Ni-incorporation into malachite as single-phase precursor for nanostructured CuO/NiO catalysts
- 03.2017 50. Jahrestreffen Deutscher Katalytiker, Weimar/Germany
Synthesis, Characterization and OER Activity of Manganese Oxide Powders
- 03.2017 50. Jahrestreffen Deutscher Katalytiker, Weimar/Germany
Promoting Methanol Synthesis: Effect of Zn and Mn Addition to Cu/MgO
- 08.2017 13th European Congress on Catalysis, Florence/Italy
Synthesis, characterization and OER activity of α -MnO₂
- 08.2017 13th European Congress on Catalysis, Florence/Italy
Activity correlation of manganese oxides for different catalytic reactions
- 09.2017 1st IMPRS – RECHARGE SCIENTIFIC SYMPOSIUM 2017 Catalysis for Sustainable Chemical Energy Conversion, Duisburg/Germany
Synthesis, characterization and OER activity of α -MnO₂
- 03.2018 26th Annual Meeting of the German Crystallographic Society, Essen/Germany
Structural effects of Ni-incorporation into malachite
- 03.2018 51. Jahrestreffen Deutscher Katalytiker, Weimar/Germany
Hollandite-type materials as electrocatalysts for the oxygen evolution reaction

List of Figures

Figure 2.1	Scheme of the diffraction geometry of the Bragg condition.	5
Figure 2.2	Abstract schema of water electrolysis and electrolyzer cell.	8
Figure 2.3	A: pH dependency of the half-cell reaction standard potentials. B: Relation between activation energy (E_a) and Gibbs energy in terms of electrocatalytic water splitting.	10
Figure 2.4	Theoretical overpotential of several oxides plotted against the standard free energy difference ΔG^0 .	11
Figure 3.1	Idealized Unit cells of hollandite-group (A), Pyrolusite (B), Ramsdellite (C), K-Birnessite (D), Bixbyite (E), Hausmannite (F) and Mn_5O_8 (G) with selected MnO_x polyhedra.	15
Figure 3.2	XRD pattern of different manganese oxides and the corresponding reference pattern (black): α - MnO_2 , β - MnO_2 , R- MnO_2 , δ - MnO_2 , α - Mn_2O_3 , Mn_3O_4 , Mn_5O_8 .	21
Figure 3.3	Graphs of thermogravimetric (left) and temperature programmed oxidation analysis (right) of α - MnO_2 .	23
Figure 3.4	XRD pattern (above) of α - MnO_2 calcined at selected temperatures and related Scanning electron micrographs (below). The oxygen content was [a] calculated from the difference to 100 % of the total elemental composition detected by atomic absorption spectroscopy, [b] determined by temperature programmed oxidation assuming a phase-pure Mn_3O_4 sample at 1000 °C.	24
Figure 3.5	Calculated lattice parameters of α - MnO_2 samples calcined at different temperatures. Grey area: presence of two phase system.	25
Figure 3.6	Scanning electron micrographs, BET surface areas and chemical formulas of different manganese oxide samples. The oxygen content was calculated from the difference to 100 % of the total elemental composition detected by atomic absorption spectroscopy.	26
Figure 3.7	Thermogravimetric analysis of different manganese oxides.	27
Figure 3.8	OER activities of manganese oxides, A and B: rotating disk electrode voltammograms, C: loss of current density during long-time measurement at 1.8 V, D: Current density at 1.8 V and the manganese	29

oxide related BET surface area and average oxidation state. The oxidation states of Cryptomelane, α -MnO₂, R-MnO₂, Pyrolusite, K-Birnessite, Bixbyite and Hausmannite are based on literature data. The oxidation state of NH₄-Hollandite is orientated on Cryptomelane, the one of Calc.-Hollandite and Mn₅O₈ was calculated from AAS measurements.

Figure S3.1	Graphical results of the Rietveld refinement of the powder diffraction data of α -MnO ₂ samples calcined at different temperatures. Experimental data (black), calculated curve (red), and difference curve (blue). Position of Bragg reflections are indicated by green.	32
Figure S3.2	XRD pattern and related Scanning electron micrographs of Bixbyite prepared by calcination of Mn(III) acetate (Bixbyite (prec.)), α -MnO ₂ synthesized by acid digestion of Bixbyite (prec.) and Bixbyite obtained by calcination of α -MnO ₂ (Bixbyite (550 °C)).	34
Figure S3.3	Graphical results of the Rietveld refinement of the powder diffraction data of different manganese oxide samples. Experimental data (black), calculated curve (red), difference curve (blue) and position of Bragg (green).	35
Figure S3.4	XRD patterns of different manganese oxides calcined at selected temperatures. Corresponding TG measurements are shown in Figure 3.7.	36
Figure 4.1	Unit cell of Cryptomelane showing the edge-sharing MnO ₆ polyhedra that form the tunnels running along the view-ing direction (c-axis).	39
Figure 4.2	XRD patterns of different Cryptomelane samples. Reference pattern: Cryptomelane.	44
Figure 4.3	Graphical results of the Rietveld refinement of the powder diffraction data of different Cryptomelane samples.	46
Figure 4.4	Raman spectra of R- and HT-Cryptomelane.	47
Figure 4.5	Scanning electron micrographs of different Cryptomelane samples.	48
Figure 4.6	Correlation between BET surface area, water content (dark yellow) and water related mass loss while thermal treatment in air between 50 and 300 °C (dark cyan) of Cryptomelane.	50

Figure 4.7	Left: thermogravimetric analysis of different Cryptomelane samples. Right: subsequently external XRD analysis of PC Cryptomelane sample. Reference pattern: green: Cryptomelane, dark yellow: Bixbyite, purple: K Birnessite, dark cyan: Hausmannite.	50
Figure 4.8	Initial rate of oxygen evolution during chemical water oxidation using Ce^{4+} as chemical oxidizing agent (a) and decomposition of hydrogen peroxide (b) catalyzed by different Cryptomelane phases and oxygen evolution rate during chemical water oxidation using Ce^{4+} over a duration of 60 min of HT-Cryptomelane (c).	52
Figure 4.9	Correlation of initial oxygen evolution during chemical water oxidation using Ce^{4+} (a) and during decomposition of hydrogen peroxide (b) with the BET surface area and plot of the initial oxygen evolution during chemical water oxidation using Ce^{4+} (c) and during decomposition of hydrogen peroxide (d) against the average aspect ratio.	53
Figure 4.10	OER activities of Cryptomelane phases, a) current density at a voltage of 1.8 V and respective BET surface areas, b) rotating disk electrode voltammograms	54
Figure 4.11	a: Resistivity measurement of selected Cryptomelane samples, b: Correlation of activity and mean aspect ratio of different Cryptomelane phases.	55
Figure 4.12	Scheme of a post-treated amorphous precursor to obtain Cryptomelane.	56
Figure 4.13	Thermogravimetric, semiquantitative differential thermal and subsequently external XRD analysis of an amorphous precursor. Reference pattern: purple: Cryptomelane, dark red: Bixbyite	57
Figure 4.14	OER activities of Cryptomelane phases made of the same amorphous precursor.	58
Figure 4.15	Loss of OER activity during stability measurement.	59
Figure 4.16	Left: Graphical results of the Rietveld refinement of the powder diffraction data of HT-Cryptomelane a) applied on adhesive tape after OER measurement and of HT-Cryptomelane after b) H_2O_2 decomposition and c) Water oxidation catalysis, right: d) Raman spectra of	59

	HT-Cryptomelane recorded at different potentials in the range from 1.02 to 1.92 V vs. RHE.	
Figure 5.1	Unit cell of α -MnO ₂ showing the edge-sharing MnO ₆ polyhedra that form the tunnels running along the viewing direction (c-axis).	65
Figure 5.2	Determination and calculation of peak-to-background ratio.	69
Figure 5.3	XRD patterns of α -MnO ₂ synthesized by acid digestion of Mn ₂ O ₃ with varying parameters.	71
Figure 5.4	Peak-to-background ratio of α -MnO ₂ phases synthesized by acid digestion of Mn ₂ O ₃ with varying parameters.	71
Figure 5.5	Scanning electron micrographs and BET surface areas of the starting material, the calcined starting material (Mn ₂ O ₃) and the product (α -MnO ₂).	72
Figure 5.6	Raman spectra of α -MnO ₂ and Cryptomelane.	74
Figure 5.7	Left: OER activities of α -MnO ₂ phases synthesized by acid digestion of Mn ₂ O ₃ with varying parameters, right: Correlation of OER activities with the peak-to-background ratio of different α -MnO ₂ phases.	75
Figure 5.8	Raman spectra of α -MnO ₂ and Cryptomelane and impact of KOH treatment.	76
Figure 5.9	Graphical results of Rietveld refinement of the powder diffraction data of different α -MnO ₂ and Cryptomelane samples.	78
Figure 5.10	Long-time OER activities of α -MnO ₂ (left) and graphical results of Rietveld refinement of the powder diffraction data of α -MnO ₂ applied on adhesive tape after OER measurement (right).	79
Figure S5.1	Graphically results of the Rietveld refinement of the powder diffraction data of Mn ₂ O ₃ precursors.	81

List of Tables

Table 3.1	Structural data, lattice parameter and [a] volume-weighted mean column height of different manganese oxide samples obtained by Rietveld refinement.	22
Table S3.1	Quality factors of Rietveld refinement of different samples.	32
Table S3.2	Lattice parameters of α -MnO ₂ samples calcined at different temperatures obtained by Rietveld refinement.	33
Table S3.3	Quality factors of Rietveld refinement of different manganese oxide samples.	35
Table 4.1	Structural data, lattice parameter and [a] volume-weighted mean column height of different Cryptomelane samples obtained by Rietveld refinement	45
Table 4.2	Peak assignment of Raman spectra.	47
Table 4.3	Textural and elemental properties of Cryptomelane. [a] BET surface area, [b] average needle length, [c] average needle width, [d] average aspect ratio of needles (length/width), [e] The oxygen content was estimated from the difference to 100 % of the total elemental composition. An average manganese oxidation state of +3.8 was assumed orientated on literature data. [10]	49
Table 4.4	Lattice parameters of HT-Cryptomelane [a] before catalysis, [b] after OER, [c] after H ₂ O ₂ decomposition and [d] after WOC.	60
Table S4.1	Results of Rietveld refinement of Cryptomelane	62
Table 5.1	Peaks observed in the Raman spectra.	74
Table 5.2	Molar ratio of potassium and manganese measured by AAS and structural data and lattice parameters of different α -MnO ₂ and Cryptomelane samples obtained by Rietveld refinement.	77
Table 5.3	Lattice parameter of α -MnO ₂ before and after OER measurement.	79
Table S5.1	Structural data and lattice parameter of the Rietveld refinement of the powder diffraction data of Mn ₂ O ₃ precursors.	81
Table S5.2	Results of Rietveld refinement of Mn ₂ O ₃ and α -MnO ₂ and Cryptomelane phases	82